

THESIS FOR THE DEGREE OF DOCTOR OF PHILOSOPHY

Finite Element Procedures for Virtual Tribology

Bertil Nilsson

CHALMERS |  UNIVERSITY OF GOTHENBURG

Department of Mathematical Sciences
Chalmers University of Technology and University of Gothenburg
Gothenburg, Sweden 2009

Finite Element Procedures for Virtual Tribology
Bertil Nilsson
ISBN 978-91-7385-303-3

©Bertil Nilsson, 2009

Doktorsavhandlingar vid Chalmers Tekniska högskola
Ny serie nr 2984
ISSN 0346-718X

Department of Mathematical Sciences
Division of Mathematics
Chalmers University of Technology and University of Gothenburg
SE-412 96 Göteborg
Sweden
Telephone +46 (0)31 772 1000

Printed at the Department of Mathematical Sciences
Göteborg, Sweden 2009

Finite Element Procedures for Virtual Tribology

Bertil Nilsson

Department of Mathematical Sciences
Chalmers University of Technology
and University of Gothenburg

Abstract

The main purpose of this thesis is to use modern goal-oriented adaptive finite element techniques in order to improve the numerical simulation of tribology. Two novel adaptive finite element methods for the Reynolds thin film model, and Stokes model including cavitation are presented and their different strategies are compared. The algorithms are inspired by an analogy with the obstacle problem and the cavitation problem that we consider is written as a variational inequality considering in the formulation the fact that the lubricant cannot stand negative stresses induced by sub-atmospheric pressure. *A posteriori* error estimates and adaptive algorithms are derived, and numerical examples illustrating the theory are supplied.

The cavitation problem and calculations is introduced and put into historical and modern perspective. Modern thoughts and techniques around the oil-pocket idea in sheet metal forming are presented. The influence of oil pockets on the contact regime is assessed, and in particular the likely effect of oil-pocket-induced cavitation in order to produce lift, is discussed. The ultimate goal with the numerical simulation is to be able to optimize the surface structure so as to take advantage of cavitation effects in the lubricant.

Keywords: Tribology, Reynolds equation, Stokes equation, cavitation, FEM, adaptivity, variational inequality, penalty formulation, error estimation, residual, duality.

Dissertation

This thesis consists of a short review and four papers:

Paper I: *Adaptive finite element methods for hydrodynamic lubrication with cavitation.*

Internat. J. Numer. Methods Engrg. 72/13 (2007) 1584–1604 (with Peter Hansbo).

Paper II: *A Stokes model with cavitation for the numerical simulation of hydrodynamic lubrication.*

Preprint 2008:17, Department of Mathematical Sciences, Chalmers University of Technology and University of Gothenburg (with Peter Hansbo).

Paper III: *A mixed finite element formulation of Reynolds equations with cavitation.*

Paper IV: *Weak coupling of a Reynolds model and a Stokes model for hydrodynamic lubrication* (with Peter Hansbo).

Contributions to co-authored papers

All but one of the appended papers address two authors. Hansbo is responsible for the overall theoretical ideas and framework and Nilsson for the computer implementations and simulations. The two hard working domains were glued together during fruitful and smooth discussions concerning ideas, realizations and pitfalls here and there in the concepts.

Acknowledgements

The thesis at hand is now to be delivered at first main stop on the long and winding academic road. It has been a project of (too) many years as a (too) small part of my normal duty lecturing mathematics and applied mechanics at Halmstad University. The scientific part has been carried out under superb guidance from the staff at Department of Applied Mechanics and Department of Mathematical Sciences at Chalmers University of Technology in Gothenburg. Ultimately has the project converged, despite the constant amplitude of my frequent oscillations between Halmstad and Gothenburg!

A significant number of people has influenced and taught me over the years. From excellent teachers when I was an undergraduate student long time ago, to fantastic colleagues during my time as applied mathematician at Volvo and then back to an academic career at Halmstad University spiced by more than well tasting graduate studies at Chalmers.

First and foremost, I would like to express my deepest gratitude to my excellent supervisor and examiner Professor Peter Hansbo at Mathematical Sciences, for taking part of your remarkable knowledge, smooth pedagogical ability and endless patience. Without your support and pep talk this work has definitely not been finished. Professor Bengt-Göran Rosén at Halmstad University for letting financial support from the University and Swedish Foundation for Strategic Research trickle down on me.

I also wish to thank my former and current colleagues for creating such an easy-going atmosphere over the years, for a great many coffee breaks and laughs in our everyday strive to become "better human beings", and for keeping up that special work atmosphere. Thank you all for being the persons you are!

Finally, I would like to thank my family and friends for their encouragement and understanding through all the years.

Halmstad in the Summer of 2009

Bertil Nilsson

*"I was working on the proof of one of my poems all the morning,
and took out a comma.*

In the afternoon I put it back again."

Oscar Wilde

Contents

| | | |
|----------|---|-----------|
| 1 | Introduction to Tribology | 1 |
| 1.1 | Historical background | 1 |
| 1.2 | Reynolds equation | 4 |
| 2 | Cavitation | 5 |
| 2.1 | Gaseous cavitation | 6 |
| 2.2 | Vaporous cavitation | 6 |
| 2.3 | Cavitation boundary conditions | 6 |
| 3 | Sheet metal forming | 8 |
| 4 | Sheet metal forming and oil-pockets | 11 |
| 5 | Virtual tribology | 14 |
| 6 | Computational modeling | 17 |
| 6.1 | Idealization | 17 |
| 6.2 | Discretization and solution | 18 |
| 6.3 | The finite element method | 19 |
| 7 | Models considered | 23 |
| 7.1 | Reynolds equation | 23 |
| 7.1.1 | Continuity of flow in a column | 24 |
| 7.1.2 | Equilibrium of an element | 26 |
| 7.1.3 | Full Reynolds equation | 28 |
| 7.1.4 | Simplifications | 28 |
| 7.1.5 | The variational formulation of Reynolds equation considering cavitation | 29 |
| 7.1.6 | The finite element formulation | 32 |
| 7.2 | Mixed formulation of Reynolds equation | 33 |
| 7.2.1 | The continuous model | 33 |
| 7.2.2 | The finite element formulation | 35 |
| 7.3 | Stokes equation | 36 |
| 7.3.1 | The continuous models | 36 |
| 7.3.2 | Finite element formulations | 39 |
| 7.4 | Weak coupling of Reynolds model and Stokes model | 40 |
| 7.4.1 | The continuous model | 42 |
| 7.4.2 | Finite element formulation | 43 |

| | | |
|-----------|------------------------------------|-----------|
| 8 | Computational aspects | 46 |
| 8.1 | Raviart-Thomas element | 48 |
| 8.2 | Crouzeix-Raviart element | 49 |
| 8.3 | Coupling matrices | 51 |
| 8.4 | Element assembly | 51 |
| 9 | Summary of appended papers | 53 |
| 10 | Future trends and ideas | 54 |

Introduction and summary of the thesis

The main purpose of this thesis is to use modern goal-oriented adaptive finite element techniques in order to improve the numerical simulation of tribology. A novel algorithm based on an analogy with the obstacle problem is presented. The cavitation problem that we consider is written as a variational inequality, considering the fact that the lubricant cannot stand negative stresses induced by sub-atmospheric pressure.

An outline of the Summary is as follows. A short historical background is given in Section 1. The cavitation problem and calculations is introduced and put into historical and modern perspective in Sections 2 and in Section 3 is sheet metal forming introduced together with problems involved. Modern thoughts and techniques around the oil-pocket idea in sheet metal forming are presented in Section 4. Section 5 address the issue of the newborn rapidly growing field of "Virtual Tribology" and the goal-oriented adaptive finite element methods that are developed in this thesis. An overview of computational modeling, especially finite element methods, is given in Section 6. In Section 7 we present the different models investigated, strong, and variational forms in harmony with solution strategies for the finite element formulations. Some computational aspects are discussed in Section 8. A more direct summary of the appended papers is given in Section 9 followed by future trend and ideas in Section 10.

1 Introduction to Tribology

1.1 Historical background

The science of *Tribology* (Greek *tribos*: *rubbing*) concentrates on *Contact Mechanics of Moving Interfaces* that generally involve energy dissipation. It encompasses historically the science fields of *Adhesion*, *Friction*, *Lubrication* and *Wear*. Today it extends over the scientific fields of physics, chemistry, solid mechanics, fluid mechanics, heat transfer, materials science and lubricant rheology [4, 10, 19, 25].

Friction is the resistance to motion whenever one solid body moves over another. It is one of the oldest problems in physics and is of great practical importance in many industrial operations. More than 400 000 years ago, our ancestors used friction when they chipped stone tools. Friction was essential when the Neanderthals by 200 000 B.C. succeeded in generating fire by rubbing wood on wood and by striking together flint stones. Early civilizations, like the Sumerian and Egyptian, discovered the usefulness of lubricants in improving the performance in facilitating transport by sleds. Figure 1 shows a painting from the tomb of Tehuti-Hetep at El-Beshed dated

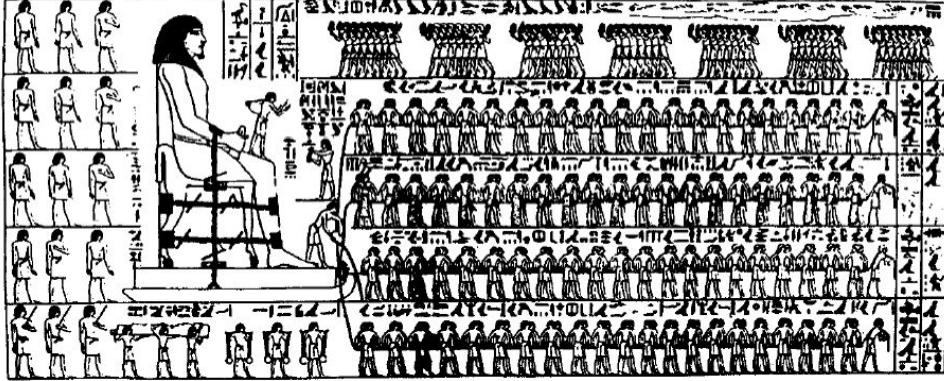


Figure 1: Transportation in the old days of an Egyptian colossus.

at about 1880 B.C., where the Egyptian method of moving stone statues is illustrated. The painting shows that the statue is moved by means of a sled, without the aid of rollers or levers. A most interesting detail in the painting is a man standing and pouring lubricant from a jar onto the ground immediately in front of the sled.

Leonardo da Vinci (1452-1519) can be named as the father of modern tribology. He studied an incredible manifold of tribological subtopics such as: friction, wear, bearing materials, plain bearings, lubrication systems, gears, screw-jacks, and rolling-element bearings. 150 years before *Amontons' Laws of Friction* were introduced, he had already recorded them in his manuscripts. Hidden or lost for centuries, Leonardo da Vinci's manuscripts were read in Spain a quarter of a millennium later. To the pioneers in tribology one counts besides Leonardo da Vinci also Guillaume Amontons (1663-1705), John Theophilus Desaguliers (1683-1744), Leonard Euler (1707-1783), and Charles-Augustin Coulomb (1736-1806). These pioneers brought tribology to a standard, and its laws still apply to many engineering problems today. Some of their findings are summarized in the following three laws:

1. The force of friction is directly proportional to the applied load. (Amontons 1st Law)
2. The force of friction is independent of the apparent area of contact. (Amontons 2nd Law)
3. Kinetic friction is independent of the sliding velocity. (Coulomb's Law)

These three laws were attributed to dry friction only, as it has been well

known since ancient times that lubrication modifies the tribological properties significantly. However, it took quite a long time until lubrication was studied pragmatically and lubricants were not just listed such as a "cooking formula". It was Osborne Reynolds around 1880 [31], who recognized the hydrodynamic nature of lubrication, and introduced a theory of fluid-film lubrication. Still today, Reynolds steady state equation of fluid film lubrication

$$F \propto \frac{U\mu}{H}$$

is valid for *hydrodynamic lubrication* of thick films ($> 10^{-6}\text{m}$) where the frictional drag force F is proportional to both the sliding velocity U , the bulk fluid viscosity μ and inversely proportional to the film lubricant thickness H . The hydrodynamic theory breaks down below a critical thickness threshold that is expressed in the *Stribeck curve* [36].

In the twentieth century the theories of dry friction and lubricated friction were further developed. Solid-like behavior of lubricants in the ultra thin film regime ($< 10^{-6}\text{m}$) led to theory of *Boundary Lubrication*, which was proposed by W.B. Hardy (1919). The *adhesion concept of friction* for dry friction, already proposed by Desanguliers, was applied with great success by Bowden and Tabor [5] to metal-metal interfaces.

Adhesion is a term relating to the force required to separate two bodies in contact with each other. Desanguliers (1734) proposed adhesion as an element in the friction process, a hypothesis which appeared to contradict experiments because of the independence of friction on the contact area (Amontons 2nd Law). Therefore the tribologists rejected Desanguliers' proposal and devoted their attention to a more geometrical hypothesis of friction, the interlocking theory of mechanical asperities. The contradiction between the adhesive issue and Amontons 2nd Law cleared up by the introduction of the concept of the *real area of contact*. The real area of contact is made up of a large number of small regions of contact, in the literature called asperities or junctions of contact, where atom-to-atom contact takes place. Bowden and Tabor showed that the force of static friction between two sliding surfaces is strongly dependent on the real area of contact. A very important outcome of their work, which led to the asperity contact theory of friction, is their detailed discussion about adhesive wear. In contrast to abrasive wear which applies to the form of wear arising when a hard, rough surface slides against a softer surface, in adhesive wear, asperity junctions plastically deform above a critical shear strength, which depends on the adhesive forces of the two surfaces in contact. Assuming during a frictional sliding process a fully plastic flow situation of all asperities, friction is found to change linearly with the applied load as demanded by Amontons 1st Law.

Bowden and Tabor investigated friction also from the perspective of a

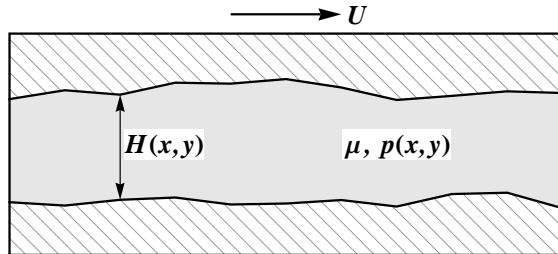


Figure 2: Reynolds channel.

purely elastic sliding process. They used a simplified single asperity model of contact based on the *Hertzian elastic theory*, and found a non-linear friction-load dependence ($F \propto L^{2/3}$), which clearly contradicted Amontons 1st Law and the experiments conducted at that time. It was Archard [3], who recognized that there was no contradiction between an elastic single asperity model and Amontons 1st law that is based on a contact that involves many asperities. Instead of assuming a constant number of asperities as Bowden and Tabor did, Archard assumed a load dependent number of asperities. With this assumption the controversy between the elastic multiple asperity hypothesis and Amontons 1st Law could be resolved. Greenwood and Williamson [20] further improved the method with a Gaussian and exponential distributions of asperities. With the birth of the *atomic force microscope (AFM)* and *friction force microscope (FFM)* Bowden and Tabor's single asperity elastic theory ($F \propto L^{2/3}$) could be experimentally verified.

1.2 Reynolds equation

The first mathematical approach to tribology was undertaken by Leonard Euler with a geometrical resistance theory of "dry" friction - the *Interlocking Asperity Theory*. Euler's theory provides us with the two well known terms for static and dynamic friction. The static friction coefficient is provided by the tangent of the asperity angle, while the dynamic friction coefficient is reduced by the kinetic term. But the true workhorse for many of years is of course the Reynolds equation. It has been used successfully to determine the pressure distribution in the fluid film for a wide range of applications from bearings, seals to sheet metal forming processes.

In the spirit of Figure 2, where a typical channel is furnished with the x -axis oriented as the relative surface velocity U and z -axis upwards, he made the following assumptions:

1. Body forces are neglected, i.e. there are no extra fields of forces acting

on the fluid.

2. The pressure is constant through the thickness of the film.
3. The curvature of surfaces is large compared with film thickness. Surface velocities need not be considered as varying in direction.
4. There is no slip at the boundaries.
5. The lubricant is Newtonian, i.e. stress is proportional to rate of shear.
6. The flow is laminar.
7. Fluid inertia is neglected.
8. The viscosity is constant through the film thickness.

With these assumptions considered, Reynolds derived the well known equation as usually quoted

$$\frac{\partial}{\partial x} \left(H^3 \frac{\partial p}{\partial x} \right) + \frac{\partial}{\partial y} \left(H^3 \frac{\partial p}{\partial y} \right) = 6\mu U \frac{\partial H}{\partial x}, \quad (1.1)$$

or

$$\nabla \cdot (H^3 \nabla p) = 6\mu U \frac{\partial H}{\partial x}. \quad (1.2)$$

2 Cavitation

Cavitation is the disruption of what would otherwise be a continuous liquid phase by the presence of a gas or vapor or both. The phenomenon has been examined by scientists and engineers for a century or more. The investigations according to sheet metal forming considering cavitation are by all means limited, so this review concentrates on cavitation in bearings and seals. This is really no limitation due to similarities in the physical layout of the models. There have been many studies outside the field of lubrication. Most of these have been concerned with aqueous systems, and the erosive damage to surfaces bounding a cavitating flow has received much attention. Components that have proved vulnerable to cavitation erosion damage include pump impellers, valves, marine propellers, pipes and cylinder liners. Another nontribological problem that has attracted attention in recent times is the oscillation of a hydrofoil, which may be induced by cavitation. In his classical paper identifying the mechanism of hydrodynamic pressure generation in lubricating films, Reynolds [31] and later Rayleigh [30] clearly recognized the possible influence of cavitation on bearing behavior. The formation of cavities and their disposition affects the pressure

generated in a continuous thin film and hence the integrated quantities such as the load capacity of bearings. Work by tribologists in the last century has resulted in the development of cavitation models that to some extent makes it possible to predict the performance of liquid-film bearings with acceptable engineering accuracy for the majority of applications. However it is true to say that the physical understanding of cavitation is still not satisfactory.

Two basic forms of cavitation in lubricating films are recognized: gaseous and vaporous.

2.1 Gaseous cavitation

The most common way in which gas (air) cavities arise in a lubricant is due to ventilation from the surrounding atmosphere whenever sub-ambient pressures occur. However, the emission of dissolved gases from solution when the liquid pressure falls below the saturation pressure is another apparent mechanism by which gas cavities may be formed. Typically mineral oils contain dissolved air with a saturation pressure near to atmospheric resulting in gas release. While in many regards ventilation and gas release result in similar behavior in lubricant films, indeed no distinction is usually made in analytical work.

The growth of air bubbles trapped between asperities or in pre-fabricated oil-pockets on the surface is another way in which gas cavities can be induced, although little attention has been given to this possibility until recently, Figure 3.

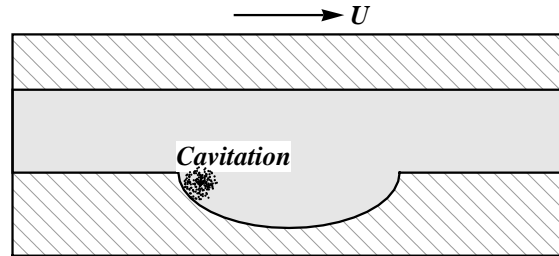
2.2 Vaporous cavitation

If the pressure in a lubricant falls to its vapor pressure, i.e. phase change, it may boil at ambient temperature. Vapor-filled cavities will be formed and these may later collapse, causing cavitation erosion. The occurrence of vaporous cavitation is normally restricted to situations in which the loading is dynamic.

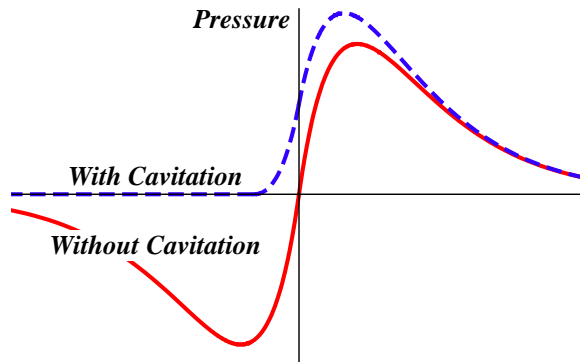
2.3 Cavitation boundary conditions

In this section the historically most important cavitation boundary conditions will be presented. For a more elaborate discussion and motivation of their behavior see [11, 12] and the references given therein. Consider the converging-diverging channel in Figure 4.

The conditions at the outlet boundary have a great influence on the shape of the pressure distribution and the clue to correct boundary conditions lies in the continuity of the flow. A direct application of Reynolds equation with $p(\pm\infty) = 0$ gives an anti-symmetrical pressure distribution. This case



(a) Cavitation upstream in the oil-pocket.



(b) Associated pressure curves.

Figure 3: Asperity cavitation effect.

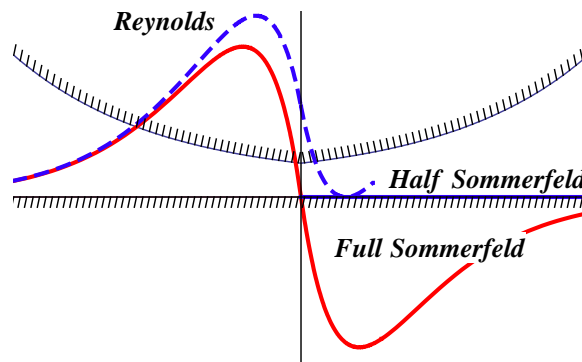


Figure 4: Comparison of classical boundary conditions.

is now bearing the name after the inventor Sommerfeld [34]. Obviously, this profile will not produce any lift. Now lubricating fluids cannot stand large and continuous negative pressures without cavitation. The simplest way of taking cavitation into consideration is simply to apply the fact that the liquid is unable to sustain negative pressures, i.e. assume atmospheric pressure in the region in which pressures otherwise would be sub-atmospheric. This is called the half-Sommerfeld or Gumbel [21] boundary conditions. Various objections were raised to the half-Sommerfeld, the most serious one concerns the unnatural discontinuity in the pressure gradient on the border between the two phases. The cure was introduced by Swift [37] and Stieber [35]. They added the condition that also $\frac{dp}{dx} = 0$ on the internal boundary now located at any desired position. This is also recognized in the literature as the Reynolds or continuity boundary conditions. As a result of this the positive part of the pressure distribution will be a bit amplified and the extreme point is also transferred slightly downstream compared with the half-Sommerfeld analysis. The experimentally observed occurrence of a sub-cavity pressure loop in bearings lead to the idea that flow separation might be playing a role in film rupture. A technique taking this into account was introduced by Floberg [16, 17, 18]. He assumed a no net flow into the cavity and suggested boundary conditions on film rupture which defines the shape of a single cavity. His model incorporates the possibility for a liquid with a capability to sustain a known sub-atmospheric pressure. The ideas were further investigated by Taylor [38]. A comparison of pressure distributions resulting from the first three boundary conditions can be seen in Figure 4.

An obvious and very serious drawback of these attempts is of course that the cavitation region must be known or dictated *a priori*. This state of affairs will be taken further in a following section.

3 Sheet metal forming

In metal forming, a piece of material is plastically deformed between tools to obtain the desired product. A special class of metal forming concerns the case where the thickness of the piece of material is small compared to the other dimensions; sheet metal forming. Sheet metal forming is a widely used production process and makes a good deal of the worldwide total steel and aluminum production. It is characterized by a stress state in which the component normal to the sheet plane is generally much smaller than the stresses in the sheet plane. A commonly used sheet metal forming process is the deep drawing process, Figure 5.

An initially flat or pre-shaped sheet material, the blank, is clamped between the die and the blankholder. The blankholder is loaded by a

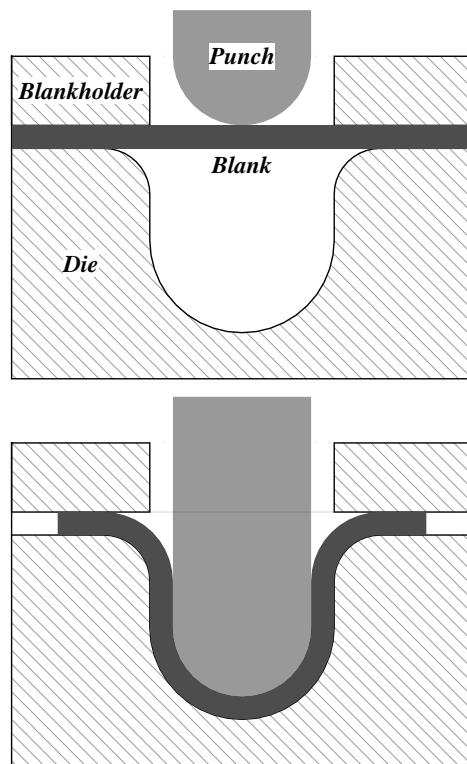


Figure 5: Deep drawing sheet metal forming.

blankholder force, which is necessary to prevent wrinkling and to control the material flow into the die cavity. Then the punch is pushed into the die cavity, simultaneously transferring the specific shape of the punch and the die to the blank. During the forming stage the material is drawn out of the blankholder die region, whereas the material is subjected to compressive and tensile stresses during forming. When a very high blankholder force is applied, the deep drawing process becomes a stretching process. In stretch forming the material is fixed under the blankholder, leading to thickness reduction in the remaining part of the blank in which the stresses are tensile in almost all directions. Stretch forming is used mainly to produce large shallow parts that must be subjected to sufficient straining to improve the flex resistance. To conclude, the material flow into the die cavity is controlled by the blankholder, a restraining force is created by friction between the tools and the blank. The friction conditions during forming are influenced by the lubricant, the presence of coatings on the blank, surface roughness of the tools and the blank, blankholder pressure and process speed.

The deep drawing process is frequently used in the automotive industry to manufacture products with even more complicated shapes and curvatures. Nowadays, the automotive industry favors light construction principles, leading to the usage of light materials (aluminum and sandwich laminates), tailored blanks and the usage of new production processes such as hydroforming.

The deep drawing process is applied with the intention of manufacturing a product with a desired shape and no failures. The final product shape after deep drawing is defined by the tools, the blank and the process parameters. An incorrect design of the tools and blank shape or an incorrect choice of material and process parameters can yield a product with a deviating shape or with failures. A deviating shape is caused by elastic springback after forming and retracting the tools. The most frequent types of failure are wrinkling, necking (and subsequently tearing), scratching and orange peel, Figure 6.

Wrinkling may occur in areas with high compressive strains, necking may occur in areas with high tensile strains, scratching is caused by defects of the tool surface and orange peel may occur after excessive deformations, depending on the grain size of the material. The deformation patterns of the sheet material are influenced by the material properties and the friction conditions. Generally, sheet material behaves anisotropically which means that the material shows a different deformation behavior in different directions because of the rolling process. An example of anisotropy is the development of ears in cylindrical cup drawing.



Figure 6: Frequent failures applied to sheet metal forming.

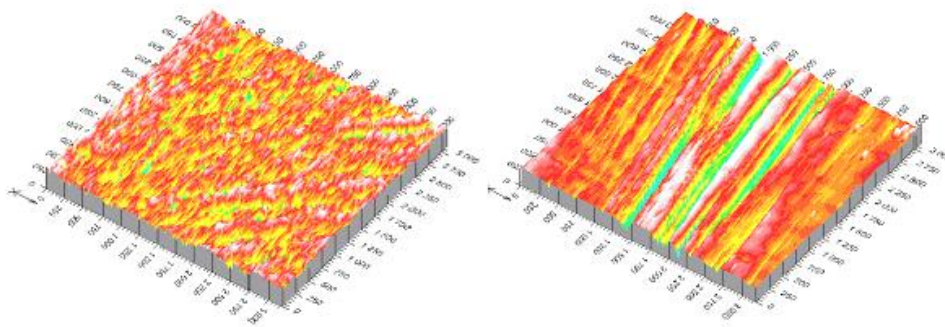


Figure 7: Two surfaces with different statistical properties.

4 Sheet metal forming and oil-pockets

There seems to be two basic approaches to the problem of a lubricated rough surface sliding against a smoother surface. In Figure 7 two such manufactured rough surfaces with different statistical properties are exemplified.

The first is to consider the effect of the asperities themselves. As the surfaces are in relative motion, the lubricant pressure increases upstream of an asperity and decreases downstream. The changes of pressure should normally cancel each other out. But if the downstream pressure drops below the cavitation pressure, the resulting cavitation will raise the local pressure to the ambient one. There will then no longer be enough negative pressure to cancel out the positive pressure and the net result will be to generate a

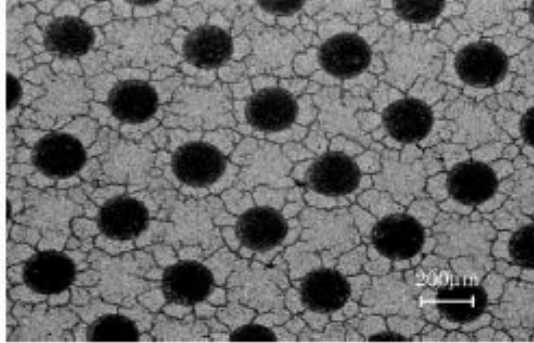
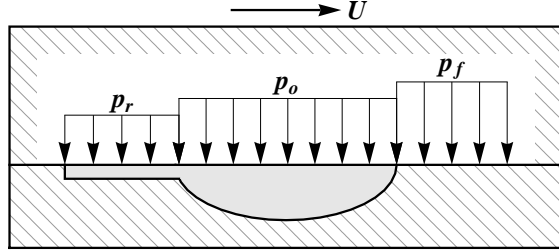


Figure 8: Textured surface.

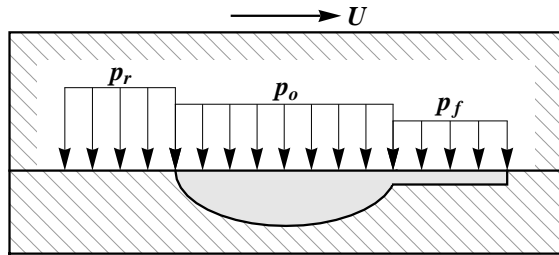
lifting force. The more cavitation, the greater the lift and consequently the lower the friction [22, 2]. This is apparently the mechanism which enables rotary lip seals to function [32].

The second approach, which is addressed here, is to consider the effect of holes, pits or oil pockets, which may exist on the rough surfaces. The use of textured surfaces, Figure 8, producing oil-pockets, in order to improve the performance and quality of products that has experienced lubricated highly loaded contacts during fabrication is a new and promising development being studied by several research groups, both at universities and in industry, [27, 14, 15, 39].

The use of textured surfaces may improve the load carrying capacity and reduce friction in two ways: by induced cavitation upstream in the oil-pockets providing lift themselves, Figure 3, and also by acting as a reservoir of lubricant which will leak out around their boundaries to minimize direct metallic contact in the surrounding region. The former mechanism requires rapid relative translation of the surfaces and so would be expected to dominate in tribological environments characterized by high-speed motion. The latter mechanism would be expected to dominate in environments of low translation speeds such as drawing. In situations where translation speed varies with time or location, for instance reciprocating sliding or gear meshing, the relative importance of the two mechanisms is likely to vary. Reynolds, as described in [19], first established the existence of lift due to cavitation in a journal bearing. The onset of cavitation delays and increases the maximum pressure, which decays asymptotically to zero downstream of the axis of symmetry, thus giving rise to a net separating force, Figure 3. The adaptive finite element methods presented in this thesis gives a very similar pressure distribution, confirming that in principle an oil pocket will



(a) MPHDL, a backward flow of the lubricant.



(b) MPHSL, a forward flow of the lubricant.

Figure 9: Oil-pocket leakage mechanisms.

produce lift by cavitation. The other way in which the presence of oil pockets can reduce friction is by acting as a reservoir to trap lubricant which can subsequently be released under the squeezing action of loads to maintain a lubricant film between the contacting surfaces [26]. With applied pressure, higher sliding speed and hydrodynamic shear stress exerted by the lubricant.

Apparently, oil pockets reduce friction in lubricated contact by two mechanisms, lift and leakage. The relative importance of these two mechanisms in any given application has still to be established. The optimum friction reduction by lift appears to depend on a combination of oil pocket size, depth-to-diameter ratio and distribution. Friction reduction by leakage involves two lubrication mechanisms termed MPHDL and MPHSL, Figure 9. Micro Plasto Hydro Dynamic Lubrication (MPHDL), if the lubricant is squeezed out backwards from the oil pocket, is induced by hydrodynamic pressure caused by the relative movement between sheet and die. The mechanism is initiated when the hydrodynamic pressure p_0 in the pocket exceeds the pressure p_r in the rear of the pocket. A forward flow of the lubricant, Micro Plasto Hydro Static Lubrication (MPHSL), occurs when the hydrostatic pressure p_0 exceeds the die pressure p_f in front of the pocket. The prerequisite for MPHSL occurs when the pocket moves towards an area with lower die pressure. The two lubricant mechanisms are affected by reduction,

drawing speed, lubricant viscosity, die angle and back tension, pocket volume and shape.

5 Virtual tribology

Without extensive knowledge of the influences of all control variables on the deep drawing process it is hardly possible to design the tools adequately and make a proper choice of blank material and lubricant to manufacture a product with the desired shape and performance using a minimum of power during the process. As a result, after the first design of the tools and choice of blank material and lubricant, an extensive and time consuming trial and error process is started to determine the proper tool design and all other variables, leading to the desired product. This trial and error process can yield an unnecessary number of deep drawing strokes, or may even require redesigning the expensive tools. To reduce this waste of time and cost, computer simulation can be used to replace the experimental trial and error process modeling by a virtual one and by extension optimize it.

The prime objective of an analysis is to assist in the design of a product. To design or select the tools and the equipment, such design essentially consists of:

- predicting the material flow,
- determining whether it is possible to form the part without surface or internal defects,
- predicting the forces and stresses necessary to execute the forming operation.

In the past a number of methods of analysis have been developed and applied to various forming processes. These methods have been useful in qualitatively predicting forming loads, overall geometry changes of the deformed blank and material flow and in determining approximate optimum process conditions. However, a more accurate determination of the effects of various process parameters on the deep drawing process has become possible only recently, when the finite element method entered the arena.

Rapid developments in computer hardware make the finite element analysis of complex deformation responses increasingly applicable. The finite element method is used worldwide to simulate the deep drawing process and has become a reliable numerical simulation technology. For an accurate simulation of a real life deep drawing process an accurate numerical description of the tools is necessary, as well as an accurate description of material

behavior, contact behavior and other process variables. The numerical description of the tools is provided by CAD packages which are generally used by tool designers. The finite element method adapts favorably to the complicated surfaces generated. The description of material behavior, contact behavior and other process variables evolved from rather simple models in the earlier days to more and more sophisticated models nowadays. This evolution is due to the elaborate work of researchers working in the field of metal forming and is shown in authoritative conferences concerning sheet metal forming. Developments have been made in the field of finite element types, mesh adaptivity, material laws, failure criteria, wrinkling and surface defects, springback, contact algorithms, friction, simulation of new processes (for example hydroforming), optimization and process design.

The conventional finite element codes are based on implicit time integration. This involves repeated solutions of large systems of equations. Furthermore, equilibrium must be fulfilled after each incremental step. As a result, implicit codes are computational time and memory consuming. Hence, a new class of finite element codes based on explicit time integration was developed, resulting in a drastic decrease of computational time. In an explicit code no system of equations needs to be solved and static equilibrium is not checked after each incremental step, as the algorithm assumes an inertia dominated process. The explicit procedure is conditionally stable with a critical time step, which is proportional to the smallest element in the mesh. However, in most sheet metal forming processes inertia effects can be neglected. In order to apply the explicit algorithms in these processes, it is necessary to assume artificially high velocities and accelerations or artificially high mass density, which seems rather unrealistic. The competition between implicit and explicit finite element codes is still in full swing.

Currently, the accuracy and reliability of numerical simulations of sheet metal forming processes do not yet satisfy the industrial requirements. One of the limitations of numerical simulations is still the high computational time for complex deep drawing parts, despite the development of iterative solvers, fast contact algorithms and the ever ongoing progress in computer hardware.

Today, industries such as the automotive and aerospace industry require the solution of highly complex problems concerning three-dimensional geometries, non linear material behavior, contact conditions and large deformations. Consequently, the numerical simulation of these types of problems is potentially very expensive, even when simplifying assumptions such as membrane kinematics are made. Despite the high computer power available, it is desired that a computation can be performed overnight. Hence, the computational costs, including computation time and time to prepare and

analyze the finite element model, must be minimized while still maintaining the desired accuracy. This goal can be achieved by adaptive remeshing; the initial finite element mesh can be changed in a specific way during the simulation. Adaptive remeshing has two major advantages. First, the computational costs can be reduced by starting the simulation with a relatively coarse mesh. Remeshing at specific parts in the mesh can take place when these coarse elements are no longer able to accurately describe the geometry or the rapid variation in state variables, and this is usually the case in the final stage of the forming process. Second, when large deformations develop, the initial mesh can be highly distorted, so that the numerical simulation becomes unstable or crashes. To prevent a high mesh distortion, adaptive remeshing can be applied to enhance the element mesh during simulation.

Globally, the adaptive remeshing procedure can be divided into three phases. First, some measure of the accuracy of the finite element approximation is required. This is accomplished via a so called goal-oriented error estimator which ranks the elements according to their contribution to the total error. Consequently, the elements to be refined are a predefined subset of the mostly needed elements indicated by the error estimator. The refinement process needs to take several specific requirements into consideration, for instance, the underlying geometry. Finally, a procedure for the transfer of state variables and boundary conditions from the old mesh to the new mesh concludes the remeshing. As a result, adaptive finite element techniques can successfully be applied in simulations of the deep drawing process, significantly decreasing the required CPU time for an accurate simulation.

However, another limitation is the lack of detailed knowledge of material physics such as material behavior at large deformations, high deformation rates and contact behavior. Therefore extensive research in the field of sheet metal forming is and will be necessary to decrease the existing gap between the real life deep drawing process and the predictions obtained from deep drawing simulations. Friction behavior has up today been poorly modeled by the Coulumb's law. In order to accurately represent and effectively study and optimize the influence of rough or textured surfaces on the squeezed lubricant behavior, a more in-depth study is necessary and sophisticated mathematical models has to be developed.

Using sophisticated goal-oriented adaptive finite element techniques in harmony with modern computer hardware in order to improve the numerical simulation of tribological scenes is natural and very promising and opens up for the newborn rapidly growing field of "Virtual Tribology" and the possibility to take the analysis into the 21st century. The thesis at hand follows that path.

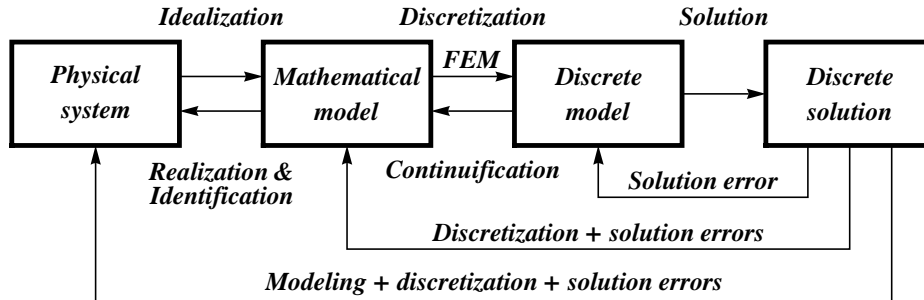


Figure 10: A simplified view of the physical simulation process, reproduced to illustrate modeling terminology.

6 Computational modeling

Computational modeling can be defined as the process of building abstract mathematical models from physical ones in order to simulate or mimic their behavior in a computer. This process is of great importance in all activities dependent on fast and reliable decision support. It may range from weather forecast, development of next generation mobile phone or car, to medical diagnostics and scheduling of transport systems.

The basic steps are discussed in more generality in what follows. The process, pretty hard to describe correctly and thoroughly, is schematized in Figure 10, which is a merged simplification, but serves well for an overview and to illustrate terminology. The three key simulation steps shown are: *idealization*, *discretization* and *solution*. Each step is a source of errors. Therefore is a companion reverse bottom up identification and control of the errors introduced of great importance.

6.1 Idealization

Idealization passes from the physical system to a mathematical model. This is the most important and perhaps most crucial step in engineering practice, because it cannot be automated. It must be done by a human, who possess interdisciplinary skills, experience and familiarity with mathematics as well practical problems and a clear idea of the goal to be reached.

The word model has the traditional meaning of a scaled copy or representation of an object. In this context we are more likely heading towards a model furnished in mathematical clothes and that should be implemented in a computer. Note that a model is built to simulate certain aspects of the behavior of a system, not the system itself. To predict everything, in all

physical scales, you must deal with the actual system. A model abstracts aspects of interest to the modeler. This means that the same physical system can give birth to different models depending on the questions we are likely to present to the model. For instance, models for weather forecasts differ a lot if it happens to be for a week, next day, or the next minute! This is a very important aspect. Different models also give the range of applicability for a particular model. This must be clearly documented so that misuse can be avoided.

Why is the mathematical model an abstraction of reality? Engineering systems tend to be highly complex. For simulation purposes it is necessary to reduce that complexity to manageable proportions. This is achieved by filtering out physical details that are not relevant to the analysis process. Mathematical modeling is actually an abstraction tool by which complexity can be controlled. It also has the advantage of handling extremely idealized cases that are not reachable in practical experiments, such as "things going to zero or infinity" and of course taking care of dangerous experiments. Consequently, picking a mathematical model is equivalent to choosing an information filter.

6.2 Discretization and solution

Mathematical modeling is a simplifying step. But models of physical systems are not necessarily simple to solve. They often involve coupled partial differential equations in space and time subject to boundary and/or interface conditions. Such models have an infinite number of degrees of freedom. We then talk about a continuous model.

At this point one faces the choice of going for analytical or numerical solutions. Analytical solutions, also called closed form solutions, are perhaps more intellectually satisfying, particularly if they apply to a wide class of problems, so that particular instances may be obtained by substituting the values of free parameters. Unfortunately they tend to be restricted to regular geometries, not that sophisticated models and simple boundary conditions. Moreover some closed-form solutions, expressed as a bunch of elementary functions or infinite series solutions, may have to be numerically evaluated anyway to be useful. Almost every interesting problem faced by an engineer tend to fall outside this scope, and for more elaborate models, numerical simulation in a computer is the only way out. Here is where finite element methods enter the scene. To make numerical simulations practical it is necessary to reduce the number of degrees of freedom to a finite number. This reduction is called discretization. The product of the discretization process is the discrete model. Discretization can proceed in spatial dimensions as well as in the time domain. The discretized model usually ends up in a

system of linear equations that naturally is handed over to a computer to be solved. The dimension of that system is equal to the finite number of degrees of freedom. The computer work needed depends heavily on that number. A solid treatment of the modeling steps should keep track of the different errors introduced, and a bottom up identification is of most value. For example, the solution error originates from the fact that we have round off problems when we apply fixed-point arithmetics in the computer. Depending on the numerical algorithms used they can be more or less severe. The discretization error is the discrepancy that appears when the discrete solution is substituted in the mathematical model. The continuation and realization, are far more difficult, elaborate, and expensive to evaluate, because model validation requires access to and comparison with experimental results. These may be either scarce, or unavailable in the case of a new product in the design stage.

Intuitively one might suspect that the accuracy of the discrete model solution would improve as the number of degrees of freedom is increased, and that the discretization error goes to zero as that number goes to infinity. This loosely worded statement describes the convergence requirement of discrete approximations. One of the key goals of approximation theory is to make the statement as precise as it can be expected from the mathematical point of view.

6.3 The finite element method

The finite element method (FEM) is the most popular and dominant discretization technique in computational engineering. It can be interpreted from either a physical or mathematical point of view. We start with the former.

The basic concept in the physical FEM is the subdivision of the mathematical model into disjoint (non-overlapping) components of simple geometry called finite elements or elements for short. The response of each element is expressed in terms of a finite number of degrees of freedom characterized as the value of an unknown function, or functions, at a set of nodal points on the element. The response of the mathematical model is then considered to be approximated by that of the discrete model obtained by connecting or assembling the collection of all elements. So FEM actually follows the process of "divide and conquer" and as an almost perfect analogy we may think of the Danish building blocks Lego of building complex shapes out of simple standardized blocks. Even if we allow the bricks to be skewed we have to live with "broken horizons" when it comes to follow smooth curves or surfaces in a CAD model, Figure 11. This can to some extent be cured by using smaller elements, we are talking of coarse and fine mesh.



Figure 11: Coarse mesh of familiar animal.

For illustrating FEM from the mathematical point of view, we start from a general setting. Seek a solution u to the, often partial, differential equation

$$L(u) = f \text{ in } \Omega, \quad (6.1)$$

together with suitable boundary conditions. In almost all practical situations we are forced to use some numerical procedure in order to find an approximate solution u_h that mimics the true solution u with an error that we can control. We prefer to seek u_h in a rather simple setting, namely as a continuous piecewise polynomial of low order where the "piecewisery" is understood to coincide with the disjoint element subdivision. We say that u_h resides in a function space V_h spanned by such functions. The reason for using polynomial, is the ease with which we can add, subtract, multiply, differentiate and integrate them. They are closed under these operations. The order is usually kept low, first or second, and then rely on adaptivity to zoom in with smaller elements were needed. This is called an h -method. The reverse path is to keep element size constant and increase the degree of the polynomial approximation in order to keep track of sharp gradients in geometry, solution field or other properties in the model, a p -method, Figure 12.

Thus, we have local support and they form an almost orthogonal basis in the element. We call u_h primary variable and let it have support at nodes and then interpolate in the elements. As u_h does not solve our equation at hand, we project the *residual*

$$R(u_h) := L(u_h) - f,$$

onto the space spanned by the basis of V_h . To this end, we may say that FEM is a nice joint venture between two classical mathematical branches,

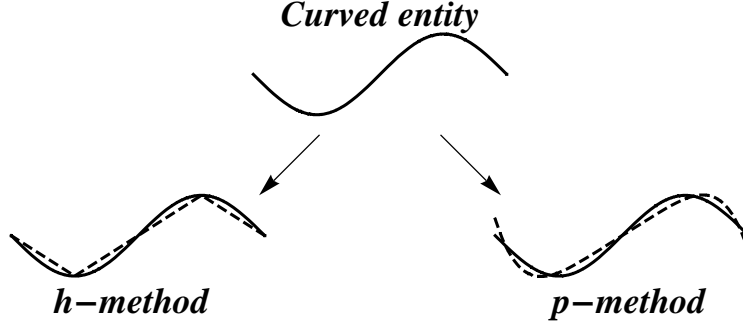


Figure 12: Approximation of given curved entity using either h -method or p -method.

namely interpolation and minimization, in this case of an energy functional (a least squares method). It is enough to check orthogonality for the residual $R(u_h)$ against each of the basis functions in the space V_h that spans u_h

$$\int_{\Omega} (L(u_h) - f)v \, d\Omega = 0, \quad \forall v \in V_h. \quad (6.2)$$

The space in which we seek our solution u_h is called *trial space* and the one we are testing orthogonality against the *test space*. These linear spaces, that usually are the same, should be complete, i.e. every Cauchy sequence should converge to some point in the space, and it should be equipped with a norm generated by an inner product, with which we can measure "distance" or "closeness" between functions. We also require the functions, or derivatives of them, that reside in the space to be square integrable. So, we end up in a Hilbert space or a Sobolev space respectively. The actual demands on the space is clear after that (6.2) has been integrated by parts (divergence theorem in higher dimensions) in order to lower the regularity requirements for the functions in V_h . Apply this to the L part in left hand side of (6.2)

$$\int_{\Omega} L(u_h)v \, d\Omega = \int_{\Gamma} (F(v)G(u_h) - F(u_h)G^*(v)) \, d\Gamma - \int_{\Omega} u_h L^*(v)v \, d\Omega, \quad (6.3)$$

we end up in the *weak form*. Here F and G are differential operators whose form follows naturally from integration by parts. The L^* is called the adjoint of L . If $L^* = L$ the L is *self-adjoint* and positive definite. In this case is $G^* = G$ also. The $F(u_h)$ are called *essential, or Dirichlet, boundary conditions* and $G(u_h)$ are the *natural, or Neumann, boundary conditions*. When $L^* = L$, $F(u_h)$ is prescribed along the boundary Γ_D , and $G(u_h)$ is prescribed on Γ_N , where $\Gamma = \Gamma_D \cup \Gamma_N$, $\Gamma_D \cap \Gamma_N = \emptyset$. We prefer to call (6.3)

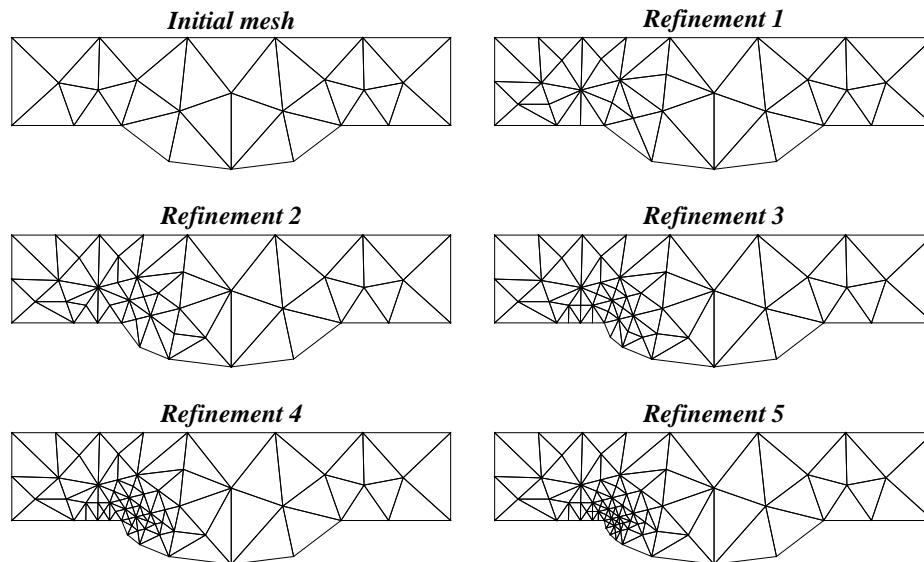


Figure 13: Adaptive refinement according to region of interest.

the Galerkin finite element method. Some times the phrase weighted residual method (WRM) is used. If (6.1) originates from a variational formulation we are on solid ground when it comes to questions concerning uniqueness of u_h and error control. However (WRM) gives the same solution u_h even if a variational form does not exist, or does, but not to our knowledge.

The soul of FEM is now manifested by the fact that the integration can be carried out element-wise and gathered together, in the so called *assembly* phase

$$\int_{\Omega} (L(u_h) - f)v \, d\Omega = \bigoplus \int_{\Omega_e} (L(u_h) - f)v \, d\Omega_e. \quad (6.4)$$

All the element manipulation, such as derivation and integration, is carried out in a standardized parameter space and mapped to physical space. As elements only "talk" to neighboring elements via common nodes the assembly phase eventually forms a set of linear equations for the unknown nodal values of the primary variable u_h . For self-adjoint problems this system is symmetric.

The functional analysis machinery behind the formulation also gives us a strict way of estimate and keeping track of the error in each element, measured in some abstract norm $\|u - u_h\|$. This error is usually bounded by the geometric size of the element. Thus, we have an indicator which tells us where elements should be marked for subdivision in the next adaptivity

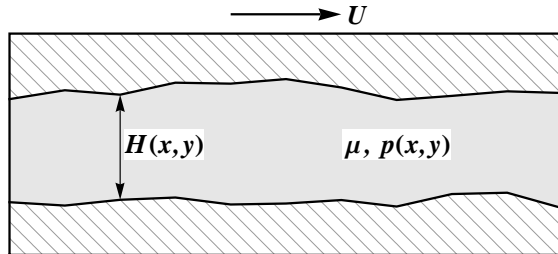
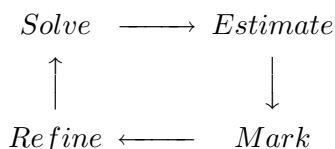


Figure 14: Reynolds channel.

step, Figure 13. This process continues until an overall desired accuracy has been achieved.



To summarize, an adaptive finite element method should consist of a sequence of successive loops until satisfaction. The process should terminate according to given stopping criteria, they may for instance be: a maximum bound on the number of refinement levels, number of degrees of freedom in the approximation, the memory usage, the time of the computation, the total size of the residual, or a combination of them.

For an excellent and mathematically sound introduction to finite element methods, we refer to [13]. A more demanding one is [6].

7 Models considered

7.1 Reynolds equation

The first mathematical approach to tribology was undertaken by Leonard Euler with a geometrical resistance theory of "dry" friction - the *Interlocking Asperity Theory*. Euler's theory provides us with the two well known terms for static and dynamic friction. The static friction coefficient is provided by the tangent of the asperity angle, while the dynamic friction coefficient is reduced by the kinetic term. But the true workhorse for many of years is of course the Reynolds equation. It has been used successfully to determine the pressure distribution in the fluid film for a wide range of applications from bearings, seals to sheet metal forming processes.

In the spirit of Figure 14, where a typical channel is furnished with the x -axis oriented as the relative surface velocity \mathbf{U} and z -axis upwards, he made the following assumptions:

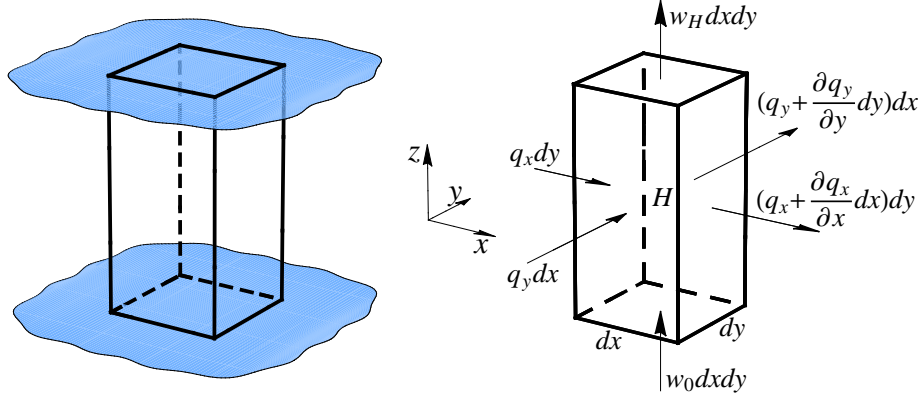


Figure 15: Continuity of flow in a column of height H .

1. Body forces are neglected, i.e. there are no extra fields of forces acting on the fluid.
2. The pressure is constant through the thickness of the film.
3. The curvature of surfaces is large compared with film thickness. Surface velocities need not be considered as varying in direction.
4. There is no slip at the boundaries.
5. The lubricant is Newtonian, i.e. stress is proportional to rate of shear.
6. The flow is laminar.
7. Fluid inertia is neglected.
8. The viscosity is constant through the film thickness.

With these assumptions considered, the development of the equations can start. First, continuity of flow is examined.

7.1.1 Continuity of flow in a column

Consider a thin column of fluid of height $H(x, y)$ and base dx, dy , Figure 15. Fluid flows from the left at a rate q_x per unit width so the volume flow rate is $q_x dy$ into the column. The rate of flow out per unit width is

$$q_x + \frac{\partial q_x}{\partial x} dx, \quad (7.1)$$

where $\frac{\partial q_x}{\partial x}$ is the rate of change of flow in the x -direction. The actual flow out is

$$\left(q_x + \frac{\partial q_x}{\partial x} dx \right) dy. \quad (7.2)$$

In the y -direction the same argument applies. The flow rate in is $q_y dx$ and out is

$$\left(q_y + \frac{\partial q_y}{\partial y} dy \right) dx. \quad (7.3)$$

The vertical flow is rather different. If the floor of the column moves upwards at a velocity w_0 and if the roof moves upward as well at a speed w_H the volume of the column changes at a rate $(w_H - w_0) dx dy$. Although the base and roof are moving, at the instant considered the height is H , though a fraction of time later it will of course have altered.

An alternative possibility is that the floor and/or roof are porous, and fluid is flowing in at a velocity w_0 or out of the column at a velocity w_H . The fluid velocity can be considered constant over the very small base area $dx dy$ hence the increase of volume is at a rate $w_0 dx dy$ and fluid leaves at a rate $w_H dx dy$.

For continuity of flow, the fluid being of constant density, the rate flowing in must equal the rate flowing out. These can all be added up. Flowing into the column

$$q_x dy + q_y dx + w_0 dx dy, \quad (7.4)$$

and flowing out

$$\left(q_x + \frac{\partial q_x}{\partial x} dx \right) dy + \left(q_y + \frac{\partial q_y}{\partial y} dy \right) dx + w_H dx dy. \quad (7.5)$$

These two are equal, equating them and canceling,

$$\frac{\partial q_x}{\partial x} dx dy + \frac{\partial q_y}{\partial y} dy dx + (w_H - w_0) dx dy = 0. \quad (7.6)$$

Now $dx dy$ is arbitrary and non zero, hence can be canceled giving the continuity of flow of a column as

$$\frac{\partial q_x}{\partial x} + \frac{\partial q_y}{\partial y} + (w_H - w_0) = 0. \quad (7.7)$$

If the top and bottom surfaces are impermeable, $w_H - w_0$ is the rate of change of height of the column according to time and may be written $\frac{\partial H}{\partial t}$. Having obtained the continuity it is necessary to look at the force balance of an element of the fluid.

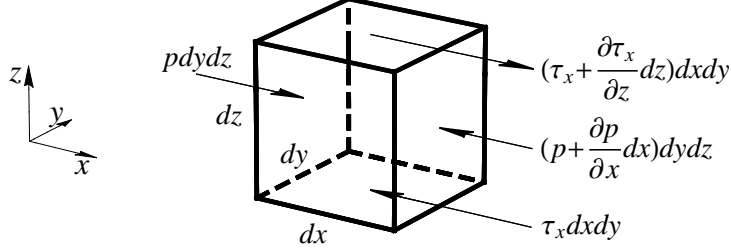


Figure 16: Equilibrium of an element.

7.1.2 Equilibrium of an element

Take a small element of fluid of sides dx , dy and dz , Figure 16, and consider first the forces in the x -direction only. On the left of the element there is a pressure p on the face of area $dydz$ giving a force of $pdydz$ acting to the right. On the opposite face the pressure is

$$p + \frac{\partial p}{\partial x} dx, \quad (7.8)$$

and the corresponding force is

$$\left(p + \frac{\partial p}{\partial x} dx \right) dydz. \quad (7.9)$$

There are shear stresses on the top and bottom faces producing forces. On the bottom face the shear stress τ_x gives a force $\tau_x dx dy$ acting to the left and on the top face, and acting to the right, is a force

$$\left(\tau_x + \frac{\partial \tau_x}{\partial z} dz \right) dx dy, \quad (7.10)$$

where the shear stress on the top face being $\tau_x + \frac{\partial \tau_x}{\partial z} dz$. These forces acting to the left and right must balance each other so

$$pdydz + \left(\tau_x + \frac{\partial \tau_x}{\partial z} dz \right) dx dy = \left(p + \frac{\partial p}{\partial x} dx \right) dydz + \tau_x dx dy, \quad (7.11)$$

expanding and canceling considering $dx dy dz$ an arbitrary non zero volume gives

$$\frac{\partial \tau_x}{\partial z} = \frac{\partial p}{\partial x}. \quad (7.12)$$

Now Newton's viscosity relation states

$$\tau_x = \mu \frac{\partial u}{\partial z}, \quad (7.13)$$

where u is the velocity of the fluid in the x -direction, so

$$\frac{\partial}{\partial z} \left(\mu \frac{\partial u}{\partial z} \right) = \frac{\partial p}{\partial x}. \quad (7.14)$$

In the y -direction where the velocity of the fluid is v the shear stresses and pressures can be equated and a similar equation follows

$$\frac{\partial \tau_y}{\partial z} = \frac{\partial p}{\partial y}, \quad \text{where} \quad \tau_y = \mu \frac{\partial v}{\partial z},$$

so

$$\frac{\partial}{\partial z} \left(\mu \frac{\partial v}{\partial z} \right) = \frac{\partial p}{\partial y}. \quad (7.15)$$

The pressure gradient in the z -direction is by assumption zero, so $\frac{\partial p}{\partial z} = 0$. Consider now equation (7.14) further. This can be integrated since p is not a function of z , thus

$$\mu \frac{\partial u}{\partial z} = \frac{\partial p}{\partial x} z + C_1. \quad (7.16)$$

Now both μ and u are functions of z but it is in this context too difficult to consider both at once so μ is taken as constant with respect to z as stated in assumption 8. It is important to realize that this is a big assumption and is only made for simplicity. The inclusion of $\frac{\partial \mu}{\partial z}$ can modify the equation very considerably in certain circumstances. However, using this assumption, a further integration can be performed to give

$$\mu u = \frac{\partial p}{\partial x} \frac{z^2}{2} + C_1 z + C_2. \quad (7.17)$$

The boundary conditions are simple, according to assumption 4, i.e. no slip at the boundaries

$$\begin{cases} u(0) = U_0 \\ u(H) = U_H \end{cases}, \quad (7.18)$$

so (7.17) and (7.18) gives

$$u = \frac{1}{2\mu} \frac{\partial p}{\partial x} (z^2 - zH) + (U_H - U_0) \frac{z}{H} + U_0. \quad (7.19)$$

Finally the flow rate $q_x = \int_0^H u dz$ in the x -direction per unit width of y

$$q_x = -\frac{H^3}{12\mu} \frac{\partial p}{\partial x} + (U_0 + U_H) \frac{H}{2}. \quad (7.20)$$

If the same procedure is followed for y using equation (7.15) it is easily found that

$$q_y = -\frac{H^3}{12\mu} \frac{\partial p}{\partial y} + (V_0 + V_H) \frac{H}{2}, \quad (7.21)$$

where V_0 and V_H in the y -direction correspond to U_0 and U_H in the x -direction.

7.1.3 Full Reynolds equation

It is now possible to replace (7.20) and (7.21) into the continuity equation (7.7)

$$\frac{\partial}{\partial x} \left(\frac{H^3}{\mu} \frac{\partial p}{\partial x} \right) + \frac{\partial}{\partial y} \left(\frac{H^3}{\mu} \frac{\partial p}{\partial y} \right) = 6 \left(\frac{\partial}{\partial x} ((U_0 + U_H) H) + \frac{\partial}{\partial y} ((V_0 + V_H) H) + 2(w_H - w_0) \right). \quad (7.22)$$

This is the full Reynolds equation with everything varying.

7.1.4 Simplifications

Firstly, write U for the sum $U_0 + U_H$ and V for $V_0 + V_H$. These are merely short forms and do not involve any assumptions. Next, it is usually possible to arrange the axes so that either

$$\frac{\partial}{\partial x}(UH) = 0, \quad \text{or} \quad \frac{\partial}{\partial y}(VH) = 0.$$

The right hand side of (7.22) can therefore now be reduced to

$$6 \left(\frac{\partial}{\partial x}(UH) + 2(w_H - w_0) \right).$$

A further simplification is to realize that the velocity of a surface does not vary from one point to another, i.e. U is not a function of x so

$$\frac{\partial}{\partial x}(UH) = U \frac{\partial H}{\partial x}.$$

Furthermore, write $w_H - w_0$ as $\frac{\partial H}{\partial t}$. This is allowable if the surfaces are impermeable so no fluid seeps in or out and they are merely moving relative to each other. The right hand side of (7.22) now becomes

$$6 \left(U \frac{\partial H}{\partial x} + 2 \frac{\partial H}{\partial t} \right).$$

Keeping both these terms in is a matter of complexity. In steadily running situations, of course, $\frac{\partial H}{\partial t}$ is zero, so this term is usually omitted. Finally μ has been taken as constant in the z -direction, so why not consider it constant everywhere, giving

$$\frac{\partial}{\partial x} \left(H^3 \frac{\partial p}{\partial x} \right) + \frac{\partial}{\partial y} \left(H^3 \frac{\partial p}{\partial y} \right) = 6\mu U \frac{\partial H}{\partial x}, \quad (7.23)$$

or

$$\nabla \cdot (H^3 \nabla p) = 6\mu U \frac{\partial H}{\partial x}. \quad (7.24)$$

This is the Reynolds equation as usually quoted.

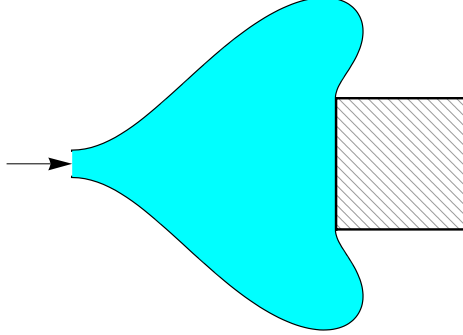


Figure 17: Blowing up a balloon considering a solid obstacle.

7.1.5 The variational formulation of Reynolds equation considering cavitation

Thus far we have not accounted for the possibility to include effects of cavitation in Reynolds equation (7.24). To cure this, we present a novel algorithm in analogy with the obstacle problem, which is encountered in many applications. For instance, blowing up a balloon and finding its shape considering a solid obstacle, Figure 17.

The model will be outlined in the following. We assume that p is zero at the boundaries of the domain Ω of interest. Let p_c be the atmospheric pressure, which without loss of generality can be taken to be zero. Obviously, (7.24) is recognized as the stationary reaction-diffusion equation, which is elliptic and the left hand operator is a positive definite operator so depending on the gradient of H we can have $p < 0$ on sets of positive measure in Ω which is a physically unrealistic situation. The lubricant cannot support sub-atmospheric pressure, so an additional condition is then $p \geq 0$ in Ω . The request to incorporate this condition into the model motivates reformulation as a variational inequality. Let c be a typical thickness of the film and set

$$p := \frac{pc^2}{6\mu U}, \quad d := \frac{H}{c}, \quad \text{and} \quad f := -\frac{\partial d}{\partial x},$$

giving the scaled version of (7.24)

$$-\nabla \cdot (d^3 \nabla p) = f. \tag{7.25}$$

For given smooth $d \in L_\infty(\Omega)$, $p \in H_0^1(\Omega)$ and $f \in H^{-1}(\Omega)$ where the appropriate Hilbert spaces

$$H^1(\Omega) = \{v : \int_{\Omega} |v|^2 + |\nabla v|^2 d\Omega < \infty\},$$

$$H_0^1(\Omega) = \{v \in H^1(\Omega), v|_{\partial\Omega} = 0\},$$

it is known that a solution p^* to (7.25) may be given by minimizing the strictly convex quadratic functional

$$J[p^*] = \min_{p \in H_0^1(\Omega)} J[p] = \min_{p \in H_0^1(\Omega)} \int_{\Omega} \frac{1}{2} d^3 |\nabla p|^2 - fp \, d\Omega. \quad (7.26)$$

In particular, $p \in H_0^1(\Omega)$ implies that p vanishes on the boundary of Ω . As previously indicated $p \geq 0$ so we restrict our admissible functions in the minimization process to reside in the space

$$K = \{v \in H_0^1(\Omega) : v \geq 0\},$$

and seek $p^* \in K$ such that

$$J[p^*] = \min_{p \in K} J[p]. \quad (7.27)$$

We assume that K is closed and so chosen that p^* exists and is unique. Relying on the convexity of K we have

$$(1 - \epsilon)p + \epsilon v \in K, \quad 0 \leq \epsilon \leq 1, \quad \forall p, v \in K.$$

As a motivation for the next step we study a smooth quadratic function $g : \mathbb{R} \rightarrow \mathbb{R}$ on the closed interval $I = [a, b]$. Seek the points $x_0 \in I$ for which

$$g(x_0) = \min_{x \in I} g(x). \quad (7.28)$$

Three cases can now occur, Figure 18,

- (a) if $a < x_0 < b$, then $g'(x_0) = 0$,
- (b) if $x_0 = a$, then $g'(x_0) \geq 0$,
- (c) if $x_0 = b$, then $g'(x_0) \leq 0$.

These statements may be summarized into one inequality by writing

$$g'(x_0)(x - x_0) \geq 0, \quad \forall x \in I. \quad (7.29)$$

The analogy with (7.28) and (7.29) to our problem at hand (7.26) is straightforward. Using Gâteaux derivative we obtain

$$\left. \frac{\partial}{\partial \epsilon} J[(1 - \epsilon)p + \epsilon v] \right|_{\epsilon=0} (v - p) \geq 0, \quad \forall v \in K,$$

and finally we have our variational inequality for Reynolds thin film model considering cavitation: find $p \in K$ such that

$$\int_{\Omega} d^3 \nabla p \cdot \nabla (v - p) - f(v - p) \, d\Omega \geq 0, \quad \forall v \in K. \quad (7.30)$$

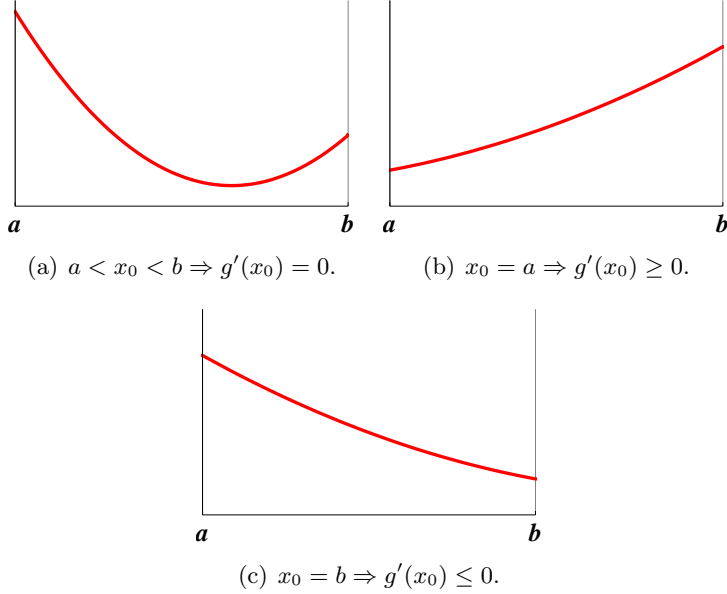


Figure 18: Three distinct cases for $g(x_0) = \min_{x \in I} g(x)$.

For the physical reasoning behind this model, see Capriz and Cimatti [9]. This formulation furthermore leads naturally to a decomposition of our domain into two disjoint sets

$$\Omega = \Omega^+ \cup \Omega^c,$$

where Ω^+ stands for the domain having positive pressure and Ω^c the domain of cavitation. The set Ω^c may be empty and in this case is our constraint inactive and we have

$$J[p^*] = \min_{p \in K} J[p] = \min_{p \in H_0^1(\Omega)} J[p].$$

In our application is usually Ω^c non empty so there is an unknown free boundary Γ^c between the two sets. This will automatically be identified through our formulation, in comparison to the classical approaches mentioned in the previous section where it needs to be known *a priori*. A true advantage. The question of regularity of the free boundary is not that easy to answer, but if we assume that Γ^c is smooth we have that

$$\left. \frac{\partial p^*}{\partial \mathbf{n}} \right|_{\Gamma^c} = 0,$$

as we approach Γ^c from Ω^+ . This is of course identified as the standard Reynolds boundary condition.

In order to solve the cavitation problem numerically, we introduce the regularized version of (7.30): given a small penalty parameter $\epsilon \in \mathbb{R}^+$, we seek $p_\epsilon \in H_0^1(\Omega)$ such that

$$\int_{\Omega} d^3 \nabla p_\epsilon \cdot \nabla v \, d\Omega + \int_{\Omega} d^3 \beta(p_\epsilon) v \, d\Omega = \int_{\Omega} f v \, d\Omega, \quad \forall v \in H_0^1(\Omega). \quad (7.31)$$

where

$$\beta(s) = \begin{cases} 0, & s \geq 0 \\ s/\epsilon, & s < 0 \end{cases}.$$

This formulation was studied by Scholz [33] in the context of obstacle problems, and was used as a starting point for formulating *a posteriori* error estimates by Johnson [24] (see also Wu [40] for application to the problem at hand). From [33], we know that the solution of (7.31) converges to the solution of (7.30) in the sense that

$$\int_{\Omega} d^3 |\nabla p - \nabla p_\epsilon|^2 \, d\Omega \leq C\epsilon \int_{\Omega} f^2 \, d\Omega.$$

The idea used in [33, 24] was to tie ϵ to the meshsize h in a finite element method for solving (7.31). In order to make dimensional sense (which is important for the conditioning of the discrete system of equations) it is clear that $\epsilon \sim h^2$, in which case the error in the penalty formulation is of the same order as the discretization error of a linear finite element method. Thus, this approach is best suited for low-order finite element methods (linear and bilinear). For higher order finite elements, we will either have a penalty error dominating the discretization error or, alternatively, with $\epsilon \sim h^q$, $q > 2$, obtain a badly conditioned system of equations.

7.1.6 The finite element formulation

Let $\mathcal{T}_h = \{T\}$ be a locally quasi-uniform triangulation of Ω into simplexes T of local mesh size h , in the following regarded as a piecewise constant function such that $h(x) = h|_T$ for $x \in T$, and let

$$V_h = \{v \in H_0^1(\Omega) : v|_T \in P_1(T), \forall T \in \mathcal{T}_h\},$$

i.e., we will use constant-strain triangles. Furthermore, we will tie the penalty parameter ϵ to the local meshsize, following [33, 24], according to $\epsilon = \gamma^{-1}h^2$, where γ is a constant. We seek $p_h \in V_h$ such that

$$\int_{\Omega} d^3 \nabla p_h \cdot \nabla v \, d\Omega + \int_{\Omega} d^3 \beta(p_h) v \, d\Omega = \int_{\Omega} f v \, d\Omega, \quad \forall v \in V_h, \quad (7.32)$$

or, explicitly,

$$\int_{\Omega} d^3 \nabla p_h \cdot \nabla v \, d\Omega + \int_{\Omega} d^3 \gamma h^{-2} p_h^- v \, d\Omega = \int_{\Omega} f v \, d\Omega, \quad \forall v \in V_h, \quad (7.33)$$

where we used the notation

$$w^- := \min(w, 0).$$

This nonlinear problem is solved iteratively using fixed-point iterations. We lumped the mass matrix resulting from the penalty term using nodal quadrature, and the condition $p_h \geq 0$ was checked node-wise. In all nodes where $p_h < 0$, penalty was applied.

A posteriori error control is derived in natural norm and in goal oriented formulation via dual solution. For the latter one is the performance for two ways of linearisation of the tangent matrix compared with the error in natural norm. The two basic forms of error control forms different strategies for the mesh adaptivity that finally show up in rate of convergence.

The error control also rates the elements according to their contributions to the total error. We subdivide those elements having highest indicators forming next refined mesh. We refine 30% of the elements with the highest indicator in each adaptive step.

In Figure 19, a typical model of an oil-pocket is illustrated together with current mesh and pressure contours after ten refinements.

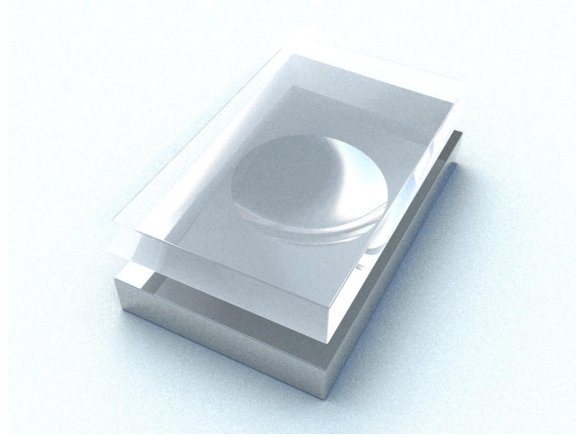
7.2 Mixed formulation of Reynolds equation

Instead of deriving the final form of Reynolds equation it is possible to reclaim the flow rates, and formulate the mixed problem using flow and pressure as variables (\mathbf{q}, p) . One obvious advantage of this formulation is that no derivative of H is needed. Another one is the possibility to take care of the cavitation problem as a pressure projection on the run due to the fact that the two fields are iterated in parallel using an algorithm of Uzawa type. Yet another advantage is that the flow is a primary variable, hence no postprocessing is necessary if leakage is of interest.

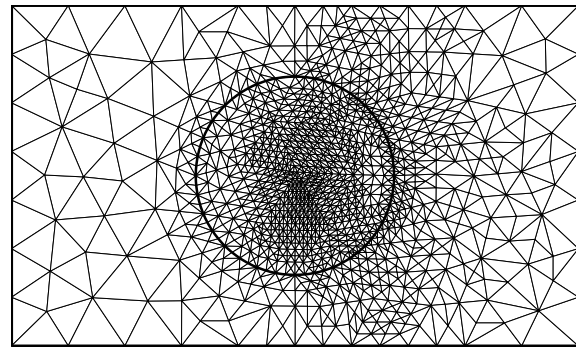
7.2.1 The continuous model

By adding (7.20) and (7.21) taking continuity (7.7) and presented simplifications into consideration, we are able to reintroduce Reynolds equation and pose the problem as a mixed one of finding (\mathbf{q}, p) such that

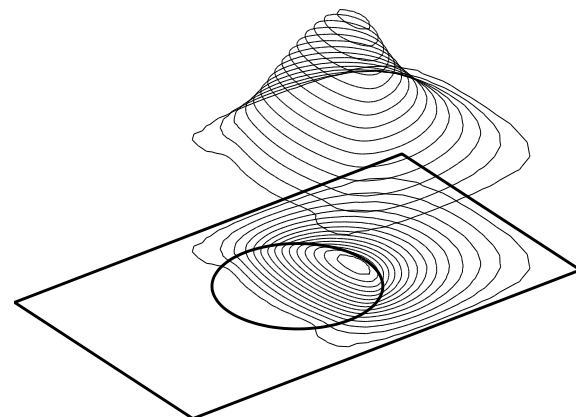
$$\begin{aligned} \frac{12\mu}{H^3} \mathbf{q} + \nabla p &= \frac{6\mu}{H^2} \mathbf{U}, \\ \nabla \cdot \mathbf{q} &= 0. \end{aligned} \quad (7.34)$$



(a) Oil-pocket model.



(b) Mesh after ten refinements using error control in L_2 -norm.



(c) Pressure contour lines.

Figure 19: Oil-pocket overview using Reynolds model.

where it has been assumed that the thickness of the film does not change over time and that $\mathbf{U} = (U_0, U_H) = (0, U_H)$ and $\mathbf{V} = \mathbf{0}$. In weak form, this problem may be written as seeking $\mathbf{q} \in H(\text{div}; \Omega)$, where

$$H(\text{div}; \Omega) = \{\mathbf{v} \in L_2(\Omega) : \|\nabla \cdot \mathbf{v}\|_{L_2(\Omega)} < \infty\},$$

and $p \in L_2(\Omega)$ such that

$$\int_{\Omega} \frac{12\mu}{H^3} \mathbf{q} \cdot \mathbf{v} \, d\Omega - \int_{\Omega} p \nabla \cdot \mathbf{v} \, d\Omega = \int_{\Omega} \frac{6\mu}{H^2} \mathbf{U} \cdot \mathbf{v} \, d\Omega, \quad \forall \mathbf{v} \in H(\text{div}; \Omega), \quad (7.35)$$

and

$$\int_{\Omega} \nabla \cdot \mathbf{q} w \, d\Omega = 0, \quad \forall w \in L_2(\Omega). \quad (7.36)$$

Boundary conditions for this problem are either handled strongly, in the case of conditions on the normal flow rate, or weakly in the case of conditions on the pressure.

7.2.2 The finite element formulation

Let $\mathcal{T}_h = \{T\}$ be a locally quasi-uniform triangulation of Ω into simplexes T of local mesh size h . From the finite element theory of mixed methods, it is well known that one must carefully select the combination of approximations for the flow variables and the pressure variable. In case of the Reynolds model, a well known stable element combination is the lowest order Raviart-Thomas finite element spaces for the flux, i.e. $\mathbf{q}_h \in \mathcal{RT}_0$, defined as [8]

$$\mathcal{RT}_0 := \{\mathbf{q} \in H(\text{div}; \Omega) : \mathbf{q}|_T \in ([P_0(T)]^2 + \mathbf{x}P_0(T)), \forall T \in \mathcal{T}_h\},$$

where $P_0(T)$ is the space of zero degree polynomials on the element T , combined with element-wise constant pressure $p_h \in Q_h$, where

$$Q_h := \{w \in L_2(\Omega) : w|_T \in P_0(T), \forall T \in \mathcal{T}_h\}.$$

Now we state our finite element problem as seek $(\mathbf{q}_h, p_h) \in \mathcal{RT}_0 \times Q_h$ such that

$$\int_{\Omega} \frac{12\mu}{H^3} \mathbf{q}_h \cdot \mathbf{v} \, d\Omega - \int_{\Omega} p_h \nabla \cdot \mathbf{v} \, d\Omega = \int_{\Omega} \frac{6\mu}{H^2} \mathbf{U} \cdot \mathbf{v} \, d\Omega, \quad \forall \mathbf{v} \in \mathcal{RT}_0, \quad (7.37)$$

and

$$\int_{\Omega} \nabla \cdot \mathbf{q}_h w \, d\Omega = 0, \quad \forall w \in Q_h. \quad (7.38)$$

For a given finite element discretization of the saddle point problem (7.37) and (7.38) we arrive at the following matrix formulation

$$\begin{pmatrix} \mathbf{A} & \mathbf{B} \\ \mathbf{B}^T & \mathbf{0} \end{pmatrix} \begin{pmatrix} \mathbf{q}_h \\ \mathbf{p}_h \end{pmatrix} = \begin{pmatrix} \mathbf{F} \\ \mathbf{0} \end{pmatrix}. \quad (7.39)$$

In order for this to be solved we need to have \mathbf{A} and $\mathbf{B}^T \mathbf{A}^{-1} \mathbf{B}$ invertible. Normally there is no problem in the finite element method for \mathbf{A} to be positive definite, but it is more crucial in the latter construction, due to the fact that \mathbf{B} is formed from a mix of the finite element spaces involved. However for our particular choice of spaces \mathcal{RT}_0 and Q_h the system is known to be solvable without any stability problems. The well-posedness of this problem follows from the general theory presented by Brezzi, Hager, and Raviart [8]. Cavitation occurs when the pressure reaches atmospheric pressure, which we for definiteness define as $p = 0$. The lubricant cannot support subatmospheric pressure, so an additional condition is $p \geq 0$ in Ω . In order to incorporate this condition into the model, we apply an iterative algorithm of Uzawa type to solve the system taking cavitation into consideration using a pressure projection on the run.

1. Let $k = 0$ and choose an initial \mathbf{p}_h^k .
2. Solve the linear system $\mathbf{A} \mathbf{q}_h^{k+1} = \mathbf{F} - \mathbf{B} \mathbf{p}_h^k$ for the flow field \mathbf{q}_h^{k+1} .
3. Perform Richardson update $\mathbf{p}_h^{k+1} = \mathbf{p}_h^k + \omega \mathbf{B}^T \mathbf{q}_h^{k+1}$, where ω is a relaxation parameter.
4. Project pressure field $\mathbf{p}_h^{k+1} = P_\Lambda(\mathbf{p}_h^{k+1})$, where the operator $P_\Lambda(\vartheta) := \max(\mathbf{0}, \vartheta)$.
5. If convergence not yet achieved, set $k = k + 1$ and go back to step 2.

The projection operator P_Λ is applied element-wise on the element values for the pressure, which by construction leads to $p_h \in \{p \in L_2(\Omega) : p \geq 0\}$.

When it comes to adapt the mesh to given goals we investigate the discrete jump of the normal component $[[\mathbf{q}_h^i]]_E$ of the flux \mathbf{q}_h^i over all interior edges E in mesh \mathcal{T}_h^i . We insert new nodes on midpoints of those edges having highest indicators forming next refined mesh \mathcal{T}_h^{i+1} . We refine 30% of the edges with the highest indicator in each adaptive step.

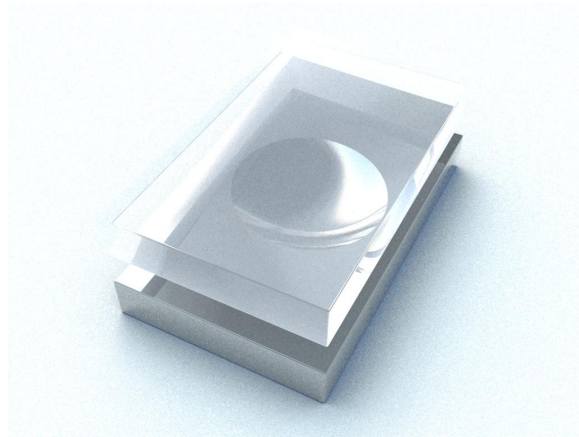
In Figure 20 is the flow field illustrated for the particular oil-pocket model under consideration. Pressure field is similar to that for the penalized model, Figure 19.

7.3 Stokes equation

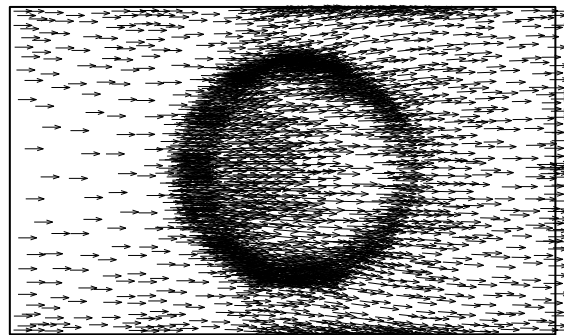
We investigate the Stokesian flow model in two flavors, the strain and Laplace formulation respectively, incorporate cavitation effect and formulate adaptive finite element methods for their solutions. We will focus on control of the error in energy-like norms.

7.3.1 The continuous models

Consider a domain Ω in \mathbb{R}^n , $n = 2$ or $n = 3$ with boundary $\partial\Omega$. We consider a lubricant with viscosity μ . The Stokes equation using strain formulation



(a) Oil-pocket model.



(b) Flow field.

Figure 20: Oil-pocket overview using 2D mixed formulation of Reynolds model.

can then be written

$$-2\mu\nabla \cdot \boldsymbol{\varepsilon}(\mathbf{u}) + \nabla p = \mathbf{f} \text{ and } \nabla \cdot \mathbf{u} = 0 \text{ in } \Omega, \quad (7.40)$$

with, for ease of presentation, $\mathbf{u} = 0$ on $\partial\Omega$. Here, \mathbf{u} is the velocity of the lubricant,

$$\boldsymbol{\varepsilon}(\mathbf{u}) = \frac{1}{2}(\nabla \otimes \mathbf{u} + (\nabla \otimes \mathbf{u})^T),$$

is the symmetric velocity gradient, p is the pressure, and \mathbf{f} is a force term. We have also used the notation

$$(\nabla \cdot \boldsymbol{\tau})_i = \sum_{j=1}^n \frac{\partial \tau_{ij}}{\partial x_j}.$$

Cavitation occurs when the pressure reaches atmospheric pressure, which we for definiteness define as $p = 0$. The lubricant cannot support subatmospheric pressure, so an additional condition is $p \geq 0$ in Ω . In order to incorporate this condition into the model, it can be written as a variational inequality as follows. Let

$$K = \{p \in L_2(\Omega) : p \geq 0\},$$

and seek $\mathbf{u} \in [H^1(\Omega)]^n$ and $p \in K$ such that

$$\int_{\Omega} 2\mu\boldsymbol{\varepsilon}(\mathbf{u}) : \boldsymbol{\varepsilon}(\mathbf{v}) \, d\Omega - \int_{\Omega} p \nabla \cdot \mathbf{v} \, d\Omega = \int_{\Omega} \mathbf{f} \cdot \mathbf{v} \, d\Omega, \quad \forall \mathbf{v} \in [H^1(\Omega)]^n, \quad (7.41)$$

and

$$- \int_{\Omega} \nabla \cdot \mathbf{u}(q - p) \, d\Omega \leq 0, \quad \forall q \in K. \quad (7.42)$$

The same cavitation story goes for the Laplace formulation of Stokes equation. This one can be written as seek $\mathbf{u} \in [H^1(\Omega)]^n$ and $p \in K$ such that

$$\int_{\Omega} \mu \nabla \mathbf{u} : \nabla \mathbf{v} \, d\Omega - \int_{\Omega} p \nabla \cdot \mathbf{v} \, d\Omega = \int_{\Omega} \mathbf{f} \cdot \mathbf{v} \, d\Omega, \quad \forall \mathbf{v} \in [H^1(\Omega)]^n, \quad (7.43)$$

and

$$- \int_{\Omega} \nabla \cdot \mathbf{u}(q - p) \, d\Omega \leq 0, \quad \forall q \in K. \quad (7.44)$$

The well-posedness of both problems follows from the general theory presented by Brezzi, Hager, and Raviart [8].

7.3.2 Finite element formulations

Let $\mathcal{T}_h = \{T\}$ be a locally quasi-uniform triangulation of Ω into simplexes T of diameter h_T . Let \mathcal{E}_h denote the set of all element faces E , of size h_E , in \mathcal{T}_h . With each edge we associate a fixed unit normal vector \mathbf{n} , and denote the jump of a function $\mathbf{v} \in \Gamma_E$ over an interior edge by $\llbracket \mathbf{v} \rrbracket := \mathbf{v}^+ - \mathbf{v}^-$ and $\llbracket \mathbf{v} \rrbracket := \mathbf{v}^+$ for an exterior one, where $\mathbf{v}^\pm := \lim_{\epsilon \downarrow 0} \mathbf{v}(\mathbf{x} \mp \epsilon \mathbf{n})$ with $\mathbf{x} \in \Gamma_E$. We define the following nonconforming finite element space for the strain formulation

$$V_h := \{\mathbf{v} \in [L_2(\Omega)]^n : \mathbf{v} \in [P^1(T)]^n, \forall T \in \mathcal{T}_h, \mathbf{v} \text{ is continuous at} \\ \text{the midpoints of all interior faces, and } \mathbf{v} = 0 \\ \text{at the midpoints of all faces along } \partial\Omega\},$$

$$Q_h := \{q \in L_2(\Omega) : q|_T \in P^0(T), \forall T \in \mathcal{T}_h\},$$

i.e., we will use the Crouzeix-Raviart element which is known to be *inf-sup* stable. We seek $(\mathbf{u}_h, p_h) \in V_h \times Q_h$ such that

$$a_h(\mathbf{u}_h, \mathbf{v}) + b_h(\mathbf{v}, p_h) = (\mathbf{f}, \mathbf{v}), \quad \forall \mathbf{v} \in V_h, \quad (7.45)$$

$$b_h(\mathbf{u}_h, q - p_h) \leq 0, \quad \forall q \in Q_h \cap K, \quad (7.46)$$

where

$$a_h(\mathbf{u}, \mathbf{v}) := \sum_{T \in \mathcal{T}} \int_T 2\mu \boldsymbol{\varepsilon}(\mathbf{u}) : \boldsymbol{\varepsilon}(\mathbf{v}) dx + \sum_{E \in \mathcal{E}_h} \frac{\gamma}{h_E} \int_E \llbracket \mathbf{u} \rrbracket \cdot \llbracket \mathbf{v} \rrbracket ds,$$

and

$$b_h(\mathbf{v}, p) := - \sum_{T \in \mathcal{T}} \int_T \nabla \cdot \mathbf{v} q dx.$$

Here h_E denotes the smallest of the sizes h_T of the elements sharing edge E . We remark that the standard formulation for the Crouzeix-Raviart element is not stable for the symmetric velocity gradient formulation of Stokes problem because of the absence of a discrete Korn's inequality. The jumps across element edges are added in order to fix this problem. We refer to [7, 23] for details.

In order to solve the discrete system, (7.45) and (7.46), we apply an iterative algorithm of Uzawa type.

1. Let $k = 0$ and choose an initial p_h^k .
2. Solve the linear system (7.45) for velocity field \mathbf{u}_h^k .
3. Update pressure field $p_h^{k+1} = P_\Lambda(p_h^k - \nabla \cdot \mathbf{u}_h^k)$, where the operator $P_\Lambda(\vartheta) := \max(0, \vartheta)$.
4. If convergence not yet achieved, set $k = k + 1$ and go back to step 2.

For the Laplacian formulation we choose the following function spaces

$$V_h := \{\mathbf{v} \in [H_0^1(\Omega)]^n : \mathbf{v}|_T \in [P^2(T)]^n, \forall T \in \mathcal{T}_h\},$$

$$Q_h := \{q \in L_2(\Omega) : q \in C^0(\Omega), q|_T \in P^1(T), \forall T \in \mathcal{T}_h\},$$

i.e., we will use the Taylor-Hood element which is known to be stable. We seek $(\mathbf{u}_h, p_h) \in V_h \times Q_h$ such that

$$\int_{\Omega} \mu \nabla \mathbf{u}_h : \nabla \mathbf{v} \, d\Omega - \int_{\Omega} p_h \nabla \cdot \mathbf{v} \, d\Omega = \int_{\Omega} \mathbf{f} \cdot \mathbf{v} \, d\Omega, \quad \forall \mathbf{v} \in V_h, \quad (7.47)$$

and

$$- \int_{\Omega} \nabla \cdot \mathbf{u}_h (q - p_h) \, d\Omega \leq 0, \quad \forall q \in Q_h \cap K. \quad (7.48)$$

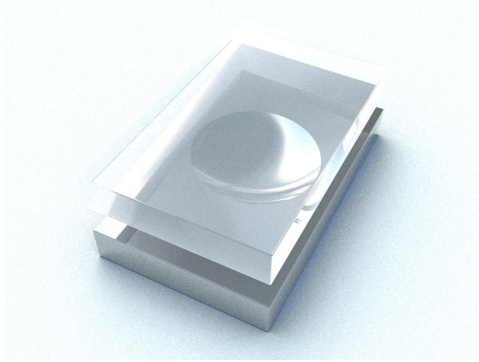
For the solution of the discrete system, (7.47) and (7.48), we also apply an iterative algorithm of Uzawa type similar to that one used for the strain formulation. However, recall that $p = -\lim_{\kappa \rightarrow \infty} \kappa \nabla \cdot \mathbf{u}$, but $\nabla \cdot V_h$ does not reside in Q_h , due to the fact that we are using Taylor-Hood elements, so in step 3 we find a continuous pressure corrector $p_d \in Q_h$.

1. Let $k = 0$ and choose an initial p_h^k .
2. Solve the linear system (7.47) for velocity field \mathbf{u}_h^k .
3. Find p_d from the system $\int_{\Omega} p_d q \, d\Omega = - \int_{\Omega} \nabla \cdot \mathbf{u}_h^k q \, d\Omega, \forall q \in Q_h$.
4. Update pressure field $p_h^{k+1} = P_{\Lambda}(p_h^k + p_d)$, where the operator $P_{\Lambda}(\vartheta) := \max(0, \vartheta)$.
5. If convergence not yet achieved, set $k = k + 1$ and go back to step 2.

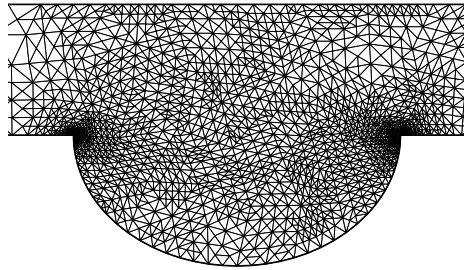
Error control is derived and adaptivity applied. The process is illustrated in Figure 21, showing mesh refinement, pressure contour lines and stream lines. We can see that recirculation in the pocket has started for this particular pocket depth. In Figure 22 we present the residual-based explicit error estimator progress during adaptivity for the Stokes 2D model.

7.4 Weak coupling of Reynolds model and Stokes model

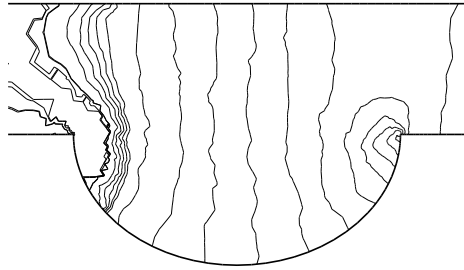
The Reynolds model is a reduced Stokes model, valid for narrow lubrication regions. In order to be able to handle non-narrow regions, there is a need to be able to transit to the more accurate Stokes model. A fundamental problem is how to couple the two models in a numerical simulation, preferably allowing for different meshes in the different domains. We present a weak coupling method for Reynolds and Stokes models for lubrication computations.



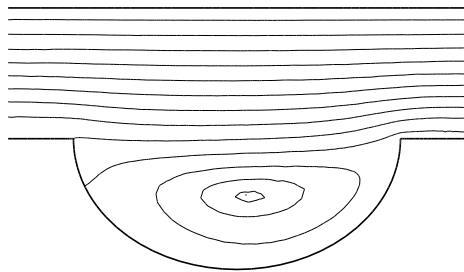
(a) Oil-pocket model.



(b) Mesh after ten refinements.



(c) Pressure contour lines.



(d) Stream lines.

Figure 21: Oil-pocket overview using Stokes 2D model.

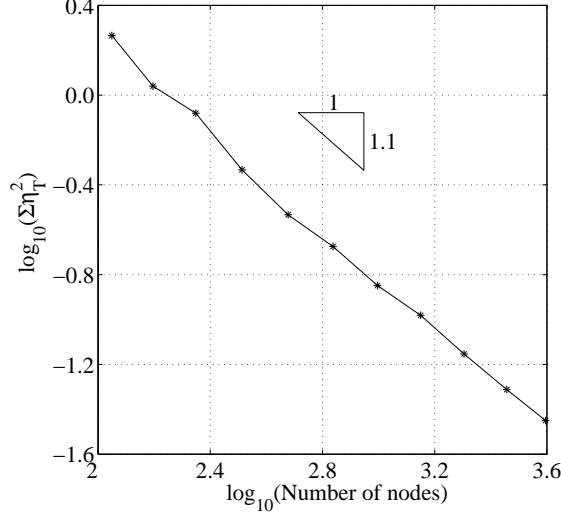


Figure 22: Residual-based explicit error estimator progress during adaptivity for the Stokes 2D model.

7.4.1 The continuous model

We are interested in a weak coupling across a vertical interface of the mixed formulation of Reynolds model and Stokes model previously considered.

The interface from the Reynolds side then appears one-dimensional, while the interface on the Stokes side is two-dimensional. Denote by Ω_R the Reynolds domain, Ω_S the Stokes domain, by Γ_{1D} the dimensionally reduced interface, and by $\Gamma_{2D} := \Gamma_{1D} \times H$ the full 2D interface. We have the following problem to solve taking cavitation into consideration:

$$\begin{aligned}
\frac{12\mu}{H^3} \mathbf{q} + \nabla p_R &= \frac{6\mu}{H^2} \mathbf{U} \text{ in } \Omega_R \subset \mathbb{R}^2, \\
\nabla \cdot \mathbf{q} &= 0 \text{ in } \Omega_R, \\
-\mu \Delta \mathbf{u} + \nabla p_S &= 0 \text{ in } \Omega_S \subset \mathbb{R}^3, \\
\nabla \cdot \mathbf{u} &= 0 \text{ in } \Omega_S, \\
\int_0^H \sigma_n(\mathbf{u}, p_S) dz + p_R &= 0 \text{ on } \Gamma_{1D}, \\
(\mathbf{q} - \int_0^H \mathbf{u} dz) \cdot \mathbf{n} &= 0 \text{ on } \Gamma_{1D}.
\end{aligned} \tag{7.49}$$

This problem must then be supplemented with boundary conditions on the exterior boundaries, which depend on the type of model adjacent to the exterior. These are handled in the usual way in the finite element setting.

7.4.2 Finite element formulation

To formulate our method, we suppose that we have regular finite element partitions \mathcal{T}_h^i , $i \in \{R, S\}$ of the two subdomains Ω_R and Ω_S into shape regular simplexes. These two meshes imply the existence of trace meshes on the interface

$$\mathcal{G}_h^i = \{E : E = T \cap \Gamma_{2D}, \forall T \in \mathcal{T}_h^i\}, i \in \{R, S\}.$$

From the finite element theory of mixed methods, it is well known that one must carefully select the combination of approximations for the flow variables and the pressure. In the case of the Reynolds model, a well known stable element combination is the lowest order Raviart-Thomas approximation for the flow rate, i.e., $\mathbf{q}^h \in V_h^R$, where

$$V_h^R := \{\mathbf{q} \in H(\operatorname{div}, \Omega) : \mathbf{q}|_T \in (P_0(T))^2 + \mathbf{x}P_0(T), \forall T \in \mathcal{T}_h^R\}$$

combined with a pressure space of element-wise constant pressures,

$$Q_h^R := \{p \in L_2(\Omega) : p|_T \in P_0(T), \forall T \in \mathcal{T}_h^R\}.$$

In the case of Stokes flow, we choose to use the well known stable Taylor-Hood element consisting of the velocity space

$$V_h^S := \{\mathbf{u} \in [C^0(\Omega)]^3 : \mathbf{u}|_T \in (P_2(T))^3, \forall T \in \mathcal{T}_h^S\}$$

and pressure space

$$Q_h^S := \{p \in C^0(\Omega) : p|_T \in P_1(T), \forall T \in \mathcal{T}_h^S\}.$$

Cavitation occurs when the pressure reaches atmospheric pressure, which we for definiteness define as $p = 0$. The lubricant cannot support subatmospheric pressure, so an additional condition is $p \geq 0$ in $\Omega_R \cup \Omega_S$. In order to incorporate this condition into the model, it can be written as a variational inequality. For this purpose we define the space

$$K = \{p \in L_2(\Omega) : p \geq 0\}.$$

We shall use a Lagrange multiplier method using piecewise constants on the 1D trace mesh \mathcal{G}_h^R for the fulfillment of the continuity requirement on the velocities. We seek $(\mathbf{q}^h, \mathbf{u}^h, p_R^h, p_S^h, \lambda^h) \in V_h^R \times V_h^S \times Q_h^R \times Q_h^S \times \mathcal{C}_h$, where

$$\mathcal{C}_h := \{\kappa \in L_2(\Gamma_{1D}) : \kappa|_E \in P_0(E), \forall E \in \mathcal{G}_h^R\},$$

such that

$$\begin{aligned} a_h((\mathbf{q}^h, \mathbf{u}^h), (\mathbf{v}_R, \mathbf{v}_S)) + b_h((p_R^h, p_S^h), (\mathbf{v}_R, \mathbf{v}_S)) \\ + c_h(\lambda^h, (\mathbf{v}_R, \mathbf{v}_S)) = f_h(\mathbf{v}_R), \end{aligned} \quad (7.50)$$

for all $(\mathbf{v}_R, \mathbf{v}_S) \in V_h^R \times V_h^S$,

$$b_h((p_R^h - w_R, p_S^h - w_S), (\mathbf{q}^h, \mathbf{u}^h)) \leq 0, \quad (7.51)$$

for all $(w_R, w_S) \in (Q_h^R \cap K) \times (Q_h^S \cap K)$, and

$$c_h(\kappa, \mathbf{q}^h, \mathbf{u}^h) = 0, \quad \forall \kappa \in \mathcal{C}_h. \quad (7.52)$$

Here

$$\begin{aligned} a_h((\mathbf{q}, \mathbf{u}), (\mathbf{v}_R, \mathbf{v}_S)) &:= \int_{\Omega_R} \frac{12\mu}{H^3} \mathbf{q} \cdot \mathbf{v}_R d\Omega + \int_{\Omega_S} \mu \nabla \mathbf{u} : \nabla \mathbf{v}_S d\Omega, \\ b_h((w_R, w_S), (\mathbf{v}_R, \mathbf{v}_S)) &:= - \int_{\Omega_R} w_R \nabla \cdot \mathbf{v}_R d\Omega - \int_{\Omega_S} w_S \nabla \cdot \mathbf{v}_S d\Omega, \\ c_h(\gamma, (\mathbf{v}_R, \mathbf{v}_S)) &:= \int_{\Gamma_{2D}} \gamma \mathbf{n} \cdot (\mathbf{v}_R - \int_0^H \mathbf{v}_S dz) ds, \\ f_h(\mathbf{v}_R) &:= \int_{\Omega_R} \frac{6\mu}{H^2} \mathbf{U} \cdot \mathbf{v}_R d\Omega. \end{aligned} \quad (7.53)$$

It is clear from the formulation that on every one-dimensional element side on \mathcal{G}_h^R the (constant) normal component of the flow rate will be set equal to the mean of the Stokes velocities over the height (multiplied by the height). The problem could thus alternatively be posed in a discrete space where this side condition is used directly in the definition of the space. The well-posedness of this problem follows from the general theory presented by Brezzi, Hager, and Raviart [8], and for the interface condition in this setting we refer to the closely related approach of Alonso et al. [1]. For solving this nonlinear saddle point problem, we have chosen to use an Uzawa iteration method. In order to find a good initial solution, we first assemble the finite element matrices emanating from full model (7.49), written using the unrestricted spaces (that are actually used in the iterations)

$$\begin{pmatrix} \mathbf{K}_S & \mathbf{B}_d & \mathbf{0} & \mathbf{0} & \mathbf{C}_S \\ \mathbf{B}_d^T & \mathbf{0} & \mathbf{0} & \mathbf{0} & \mathbf{0} \\ \mathbf{0} & \mathbf{0} & \mathbf{K}_q & \mathbf{K}_p & \mathbf{C}_R \\ \mathbf{0} & \mathbf{0} & \mathbf{K}_p^T & \mathbf{0} & \mathbf{0} \\ \mathbf{C}_S^T & \mathbf{0} & \mathbf{C}_R^T & \mathbf{0} & \mathbf{S}_\lambda \end{pmatrix} \begin{pmatrix} \mathbf{u}^h \\ \mathbf{p}_S^h \\ \mathbf{q}^h \\ \mathbf{p}_R^h \\ \boldsymbol{\lambda}^h \end{pmatrix} = \begin{pmatrix} \mathbf{0} \\ \mathbf{0} \\ \mathbf{F}_q \\ \mathbf{0} \\ \mathbf{0} \end{pmatrix}, \quad (7.54)$$

where the submatrices are the assembled element matrices according to the integrals found in (7.53), i.e. with $(\mathbf{v}_R, \mathbf{v}_S, w_R, w_S, \kappa) \in V_h^R \times V_h^S \times Q_h^R \times Q_h^S \times \mathcal{C}_h$ denoting generic basis functions spanning the relevant spaces, we

have

$$\begin{aligned}
\mathbf{K}_S &= \bigoplus_{T \in \mathcal{T}_h^S} \int_T \mu \nabla \mathbf{v}_S : \nabla \mathbf{v}_S \, d\Omega, \quad \mathbf{B}_d = - \bigoplus_{T \in \mathcal{T}_h^S} \int_T w_S \nabla \cdot \mathbf{v}_S \, d\Omega, \\
\mathbf{K}_q &= \bigoplus_{T \in \mathcal{T}_h^R} \int_T \frac{12\mu}{H^3} \mathbf{v}_R \cdot \mathbf{v}_R \, d\Omega, \quad \mathbf{K}_p = \bigoplus_{T \in \mathcal{T}_h^R} \int_T w_R \nabla \cdot \mathbf{v}_R \, d\Omega, \\
\mathbf{F}_q &= \bigoplus_{T \in \mathcal{T}_h^R} \int_T \frac{6\mu}{H^2} \mathbf{U} \cdot \mathbf{v}_R \, d\Omega, \\
\mathbf{C}_R &= \bigoplus_{E \in \mathcal{G}_h^R} \int_E \mathbf{n} \cdot \mathbf{v}_R \, ds, \quad \mathbf{C}_S = - \bigoplus_{E \in \mathcal{G}_h^R} \int_E \int_0^H \mathbf{n} \cdot \mathbf{v}_S \, dz \, ds, \quad \mathbf{S}_\lambda = \mathbf{0},
\end{aligned}$$

where \bigoplus denotes the assembly operator for the finite element matrix construction. We remark that in this particular case there is no need for stabilization of the multipliers, thus $\mathbf{S}_\lambda = \mathbf{0}$. A simple stabilization method could for instance mimic the idea of letting neighboring edges along \mathcal{G}_h^R be connected by springs with spring constants k_λ , giving

$$\mathbf{S}_\lambda = \bigoplus_{E \in \mathcal{G}_h^R} k_\lambda \begin{pmatrix} 1 & -1 \\ -1 & 1 \end{pmatrix}.$$

The system (7.54) is fed repeatedly into a direct linear equation solver. In each round is a simple cavitation requirement $p_S^h = \max(p_S^h, 0)$ enforced and a modification of the corresponding residuals (out-of-balance residual forces) carried out. This process is repeated until $p_S^h \geq 0$ throughout the Stokes domain. The artificial pressure boundary conditions are then released and the model with current solution state is handed over to Usawa taking cavitation into consideration using a pressure projection on the run. The Stokes and Reynolds models are solved in parallel as described in in previous chapters. We supply the details.

A core operation in Uzawa algorithm is to update the pressure field. However, recall that $p = -\lim_{\kappa \rightarrow \infty} \kappa \nabla \cdot \mathbf{u}$, but $\nabla \cdot \mathbf{V}_h^S$ does not reside in Q_h^S , due to the fact that we are using Taylor-Hood elements, so in step 3 we find

a continuous pressure corrector $p_d \in Q_h^S$.

1. Let $k = 0$ and choose as initial pressure solution ${}^k \mathbf{p}_S^h$ and ${}^k \mathbf{p}_R^h$ provided by the solution strategy of the linear system (7.54) just described.
2. Solve the condensed version of the linear system (7.54)

$$\begin{pmatrix} \mathbf{K}_S & \mathbf{0} & \mathbf{C}_S \\ \mathbf{0} & \mathbf{K}_q & \mathbf{C}_R \\ \mathbf{C}_S^T & \mathbf{C}_R^T & \mathbf{S}_\lambda \end{pmatrix} \begin{pmatrix} {}^k \mathbf{u}^h \\ {}^k \mathbf{q}^h \\ {}^k \boldsymbol{\lambda}^h \end{pmatrix} = \begin{pmatrix} -\mathbf{B}_d {}^k \mathbf{p}_S^h \\ \mathbf{F}_q - \mathbf{K}_p {}^k \mathbf{p}_R^h \\ \mathbf{0} \end{pmatrix},$$

for the vector fields ${}^k \mathbf{u}^h$ and ${}^k \mathbf{q}^h$ and the Lagrange multipliers ${}^k \boldsymbol{\lambda}^h$.

3. Find a continuous pressure corrector $p_d \in Q_h^S$ from the system $\int_{\Omega_S} p_d q \, d\Omega = - \int_{\Omega_S} \nabla \cdot \mathbf{u}^h q \, d\Omega, \forall q \in Q_h^S \Leftrightarrow \mathbf{M}_d \mathbf{p}_d = \mathbf{B}_d {}^k \mathbf{u}^h$, where \mathbf{M}_d is the lumped mass matrix, which makes the update fast.
4. Update pressure fields
$$\begin{cases} {}^{k+1} \mathbf{p}_S^h = P_\Lambda({}^k \mathbf{p}_S^h + \omega_S \mathbf{p}_d) \\ {}^{k+1} \mathbf{p}_R^h = P_\Lambda(\mathbf{F}_q + \omega_R \mathbf{K}_p^T {}^k \mathbf{q}^h) \end{cases}$$
 where ω_S and ω_R are relaxation parameters and the operator $P_\Lambda(\boldsymbol{\vartheta}) := \max(\mathbf{0}, \boldsymbol{\vartheta})$.
5. If convergence not yet achieved, set $k = k + 1$ and go back to step 2.

The projection operator P_Λ is applied point-wise on the nodal values for the pressure, which by construction leads to $\{p_R^h, p_S^h\} \in K$.

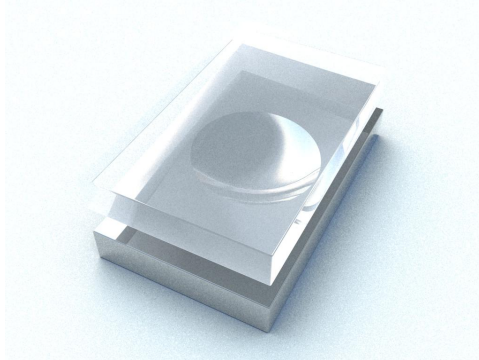
For the numerical evaluation of the integrals involved in the coupling matrices, \mathbf{C}_R and \mathbf{C}_S , a 2-point Gauss quadrature scheme is used on the edges of the one-dimensional trace mesh \mathcal{G}_h^R and a 3-point Gauss quadrature scheme for companion surface integrals on the Stokes mesh.

Finally in Figure 23, we illustrate a typical coupling situation where the 3D Stokes part is modeled with Taylor-Hood tetrahedra elements. As expected a Couette flow profile is generated in the coupling zones.

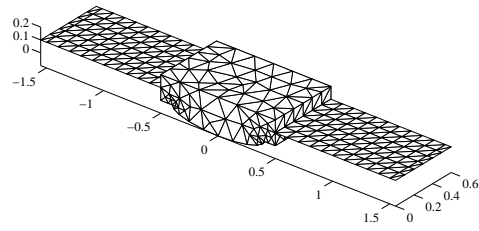
8 Computational aspects

For the development of element routines *Mathematica* has been used. All basis functions and their derivatives according to parameter space has been symbolically derived and, after optimization according to number of floating point operations needed, automatically translated to Matlab code and written to m-files.

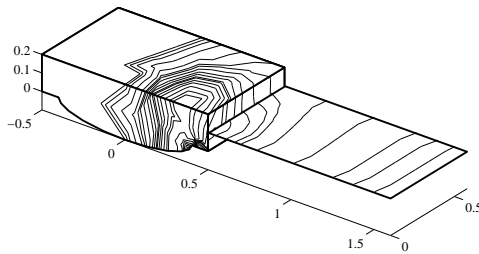
Apart from standard Taylor-Hood triangle and tetrahedra, interpolating pressure linear and velocity quadratic, the following two elements are used, namely Raviart-Thomas in 2D and Crouzeix-Raviart in 2D and 3D.



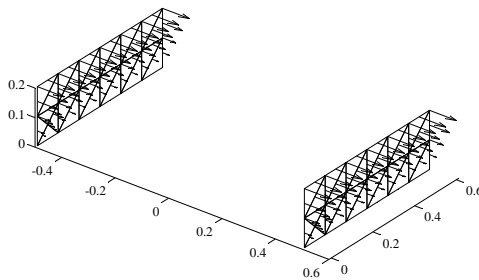
(a) Oil-pocket model.



(b) Mesh of complete model.



(c) Pressure contour lines.



(d) Couette flow profile at coupling zones.

Figure 23: Oil-pocket overview using coupling model.

8.1 Raviart-Thomas element

The Raviart-Thomas (\mathcal{RT}_k) triangular and tetrahedral elements of order k are tailor-made finite elements for approximation of vector fields in such formulations where only normal continuity is required over the element faces. They are suitable for flow-pressure formulation of fluid problems. For mixed forms of second order elliptic applications, standard $H^1(\Omega)$ -continuous approximations are well-known to cause problems in that they allow spurious modes with non-zero energy that do not exist in the continuous problem. The \mathcal{RT}_k elements are designed to approximate $H(\text{div}; \Omega)$, and does therefore not suffer from this problem. That's the reason for their popularity in the so called mixed finite element formulation.

Here we will focus on the lowest order Raviart-Thomas triangular element in 2D that is used in the thesis. This element is edge based rather than nodal and is constructed such that the normal component of each vector valued basis function φ_i is constant one on element edge E_i and zero on the two other edges, for $i \in \{1, 2, 3\}$. This construction will assure continuity in the normal, but not tangential, direction of a vector field over the element edges. To be more precise, let the vector field under consideration reside in the lowest Raviart-Thomas finite element space, i.e. $\mathbf{q}_h \in \mathcal{RT}_0$, where [8]

$$\mathcal{RT}_0 := \{\mathbf{q} \in H(\text{div}; \Omega) : \mathbf{q}|_T \in ([P_0(T)]^2 + \mathbf{x}P_0(T)), \forall T \in \mathcal{T}_h\},$$

and $P_0(T)$ is the space of zero degree polynomials on the element $T \in \mathcal{T}_h$, a locally quasi-uniform triangulation of Ω into simplexes T of local mesh size h . This means that the support is restricted to the two triangles adjacent to their common edge, or one triangle if we have an exterior edge under consideration. By direct computation it can be verified that

$$\text{div } \mathbf{q} \in P_0(T), \quad \text{and} \quad \mathbf{q} \cdot \mathbf{n}_i \in P_0(E_i),$$

where E_i are the edges of T and \mathbf{n}_i a unit normal vector to E_i for $i \in \{1, 2, 3\}$. It is possible to show that a piecewise polynomial function is in $H(\text{div}; \Omega)$ if and only if it has continuous normal components across the edges in the triangulation. This ensures that \mathcal{RT}_0 consists of all vector fields \mathbf{q} that are locally $\mathbf{q}|_T \in ([P_0(T)]^2 + \mathbf{x}P_0(T))$, and whose constant normal components across the edges are continuous.

The standard way in the finite element community to make use of a reference element for definition of the basis functions turns out to be a bit complicated in this case. In order to make elements that are continuous in the normal direction of the mapped reference element, we must assume that the geometry mapping is affine. This is usually not the case, and a more elaborate Piola transformation has to be involved. So, the construction of

the basis functions for the Raviart-Thomas spaces is most easily done in the physical configuration. Consider an element with corner nodes \mathbf{x}_i , edge vectors \mathbf{e}_i associated with edges E_i , and with edge unit normal vectors

$$\mathbf{n}_i = \begin{pmatrix} 0 & -1 \\ 1 & 0 \end{pmatrix} \frac{\mathbf{e}_i}{\|\mathbf{e}_i\|}.$$

The lowest order element basis functions can be written

$$\boldsymbol{\varphi}_i = \begin{pmatrix} a_i + c_i x \\ b_i + c_i y \end{pmatrix},$$

and to construct the vector valued basis $\{\boldsymbol{\varphi}_1, \boldsymbol{\varphi}_2, \boldsymbol{\varphi}_3\}$ on the element we need to solve

$$\boldsymbol{\varphi}_i \cdot \mathbf{n}_j = \delta_{ij},$$

at the three midpoints $\mathbf{x}_{ei} = \frac{1}{2}(\mathbf{x}_i + \mathbf{x}_{i+1}) \bmod 3$ of the edges. This is a simple linear algebra problem

$$\begin{pmatrix} n_{1x} & n_{1y} & \mathbf{n}_1 \cdot \mathbf{x}_{e1} \\ n_{2x} & n_{2y} & \mathbf{n}_2 \cdot \mathbf{x}_{e2} \\ n_{3x} & n_{3y} & \mathbf{n}_3 \cdot \mathbf{x}_{e3} \end{pmatrix} \begin{pmatrix} a_i \\ b_i \\ c_i \end{pmatrix} = \mathbf{f}_i, \quad \text{with} \quad (\mathbf{f}_i)_j = \delta_{ij}.$$

The three basis functions are illustrated in Figure 24. Note that this does not yet define the basis functions for \mathcal{T}_h uniquely, because there are two unit normal vectors to an edge. A choice for the normal can for example be made according to the numbering of the nodes in \mathcal{T}_h . For instance, let the edge vectors \mathbf{e}_i point to the node with the largest index.

8.2 Crouzeix-Raviart element

The non-conforming Crouzeix-Raviart (\mathcal{CR}) element, for triangles and tetrahedra, is a finite element that can interpolate both the field variable and the divergence of the field variable. Thus the difficult problem of locking in the incompressible limit showed by standard FE methods is eliminated. The \mathcal{CR} element is thereby suitable for (nearly) incompressible problems, such as incompressible flow. However, for linear elasticity a stability term has to be added to the weak form in order to make the \mathcal{CR} element stable. This is because without the stabilization term the \mathcal{CR} element can rotate around its side nodes.

Here, we will focus on the first order (linear) \mathcal{CR} element, which has its unknowns located at the center of gravity on the element sides, see Figure 25 for the triangle case. This implies that continuity between elements is only fulfilled at these points. The linear \mathcal{CR} element, is constructed simply defining the standard linear triangle or tetrahedra shape functions on the

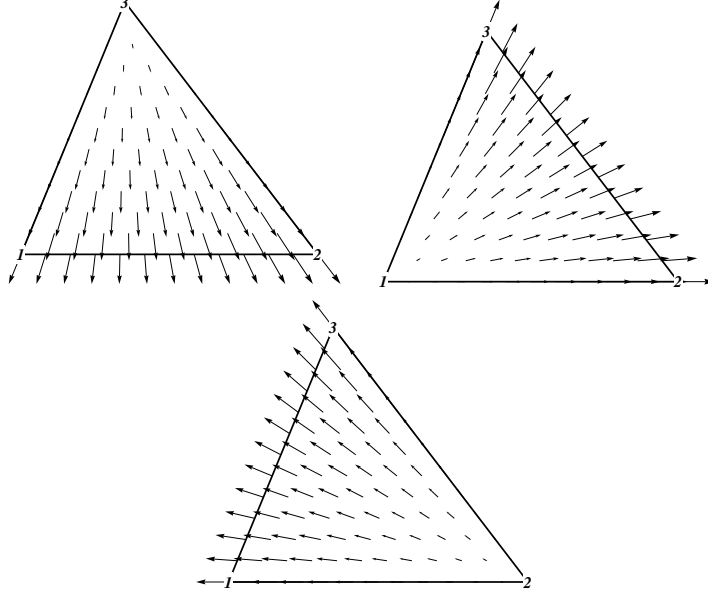


Figure 24: Lowest order Raviart-Thomas basis functions.

inscribed one, Figure 25, and then letting them be extended to the whole element. Consequently, a shape function affiliated with a side under consideration is constant one along that side and minus one at the opposite node.

Next, we show the interpolant features for the \mathcal{CR} element. Let $\pi_h \mathbf{u}$ denote the interpolation of \mathbf{u} . Further, choose the interpolant $\pi_h \mathbf{u}$ such that the average value of the exact \mathbf{u} on each element side is equal to the nodal value, i.e.,

$$\pi_h \mathbf{u}(\mathbf{x}_i) = \frac{1}{|E_i|} \int_{E_i} \mathbf{u}(\mathbf{x}_{E_i}) dE_i,$$

for element side E_i . Now, the \mathcal{CR} element can in a mean sense interpolate the divergence of the field variable on an element T , which is shown by the following manipulations

$$\int_T \nabla \cdot \mathbf{u} dT = \sum_i \int_{E_i} \mathbf{n} \cdot \mathbf{u} dE_i = \sum_i \int_{E_i} \mathbf{n} \cdot \pi_h \mathbf{u} dE_i = \int_T \nabla \cdot \pi_h \mathbf{u} dT.$$

where Gauss' theorem was used. Thus, the interpolant approximates \mathbf{u} in a mean sense and the divergence of the interpolant approximates the divergence of \mathbf{u} in (another) mean sense. A standard low order FE approximation lacks this possibility of simultaneously approximating the solution and its divergence, which can be interpreted as the underlying cause of locking.

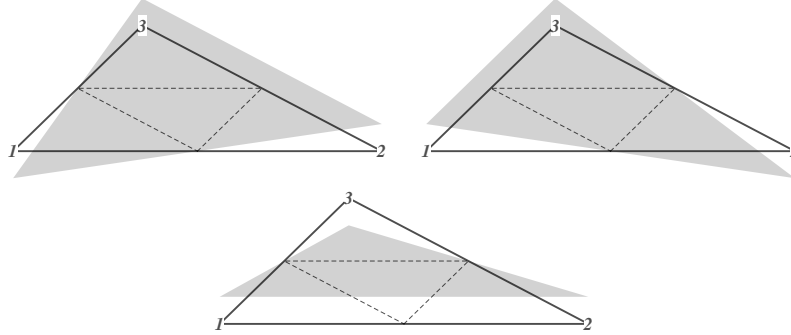


Figure 25: The three Crouzeix-Raviart basis functions.

8.3 Coupling matrices

After the involved surface integrals in C_R and C_S has been carried out in local parameter space, we need to address the values of the shape functions to their appropriate nodal degrees of freedom. As we usually do not know the actual orientation of the tetrahedra given by the program that performed the mesh of the 3D domain, it is therefore necessary to solve the inverse problem; Given a four node tetrahedra with nodal coordinates $\mathbf{x}_1, \mathbf{x}_2, \mathbf{x}_3$ and \mathbf{x}_4 and a point \mathbf{x}_c under consideration anywhere on its surface. Find the corresponding parameter values ξ, η and ζ . To be more precise, we need to solve the following system

$$[\mathbf{x}_1, \mathbf{x}_2, \mathbf{x}_3, \mathbf{x}_4] \cdot \boldsymbol{\varphi} = \mathbf{x}_c \text{ with basis functions } \boldsymbol{\varphi} = (\xi, \eta, \zeta, 1 - \xi - \eta - \zeta)^T.$$

This is a simple linear algebra problem, and the solution is given by

$$\begin{pmatrix} x_1 - x_4 & x_2 - x_4 & x_3 - x_4 \\ y_1 - y_4 & y_2 - y_4 & y_3 - y_4 \\ z_1 - z_4 & z_2 - z_4 & z_3 - z_4 \end{pmatrix} \begin{pmatrix} \xi \\ \eta \\ \zeta \end{pmatrix} = \begin{pmatrix} x_c - x_4 \\ y_c - y_4 \\ z_c - z_4 \end{pmatrix}.$$

Now it's straightforward to feed them into both the linear and quadratic tetrahedra shape functions and distribute them accordingly.

8.4 Element assembly

The assembly of sparse matrices is a key operation in finite element methods. A naive and plain implementation consumes a huge amount of time in Matlab.

```
%--- Allocate sparse global stiffness matrix.
```

```

K = sparse(nDof,nDof);
%--- Assemble all the elements.
for ie = 1:ne
    %--- Element stiffness matrix.
    Ke = elementStiffness(ie);
    %--- Map local dof to global.
    [iK,jK] = topology(ie);
    %--- Assemble.
    K(iK,jK) = K(iK,jK) + Ke;
end

```

Such an assembly of large finite element models was not the main purpose when Matlab was designed. A quick look at the internal data structures for a sparse matrix, gives a clear indication of the time thief involved. To understand why the above example are so slow, we need to understand how Matlab stores its sparse matrices. A sparse matrix is in general stored, and particular our global stiffness matrix of order `nDof` times `nDof`, as three ordinary vectors that holds information about nonzero entries in the sparse array under consideration. Let's call them `iS`, the row indices bucket, `jS`, the column indices bucket and finally `cS` the bucket of coefficients. As Matlab is an old friend of Fortran, arrays are stored in column order, with sorted row indices `iS`. This implies a massive reorganization of the triplets (`iS`, `jS`, `cS`) whenever a new nonzero coefficient calls for space in the assembly phase.

To solve the problem we create and furnish the mentioned list of triplets ourselves, and let Matlab convert them into a sparse matrix all at once. In this process we rely on the nice implemented property that, if there are duplicates, which a finite element matrix always has, the duplicates are summed, which is exactly what we want when assembling a finite element matrix. This workaround gives a speedup factor of ~ 150 when dealing with `nDof` of order five and, is expected to be even more significant as `nDof` grows.

A problem is to allocate enough space for the three buckets (`iS`, `jS`, `cS`) in advance. An `nDof`² approach will likely fill up the computer memory so, start with a reasonable, in some way problem dependent, size and let them grow nice and smooth during the assembly phase. An example follows

```

%--- Initial allocation of sparse array buckets.
mS = 1000;
iS = zeros(mS,1);
jS = zeros(mS,1);
cS = zeros(mS,1);
nS = 0;
%--- Assemble all the elements.

```

```

for ie = 1:ne
    %--- Element stiffness matrix.
    Ke = elementStiffness(ie);
    %--- Map local dof to global.
    [iG,jG] = topology(ie);
    nG      = length(iG);
    nG2     = nG*nG;
    %--- Watch out for bucket overflow.
    if ((nS + nG2) > mS)
        mS      = 2*mS + nG2;
        iS(mS) = 0;
        jS(mS) = 0;
        cS(mS) = 0;
    end
    %--- Add on.
    kG      = 1:nG2;
    kS      = nS + kG;
    iS(kS) = iG(1+mod(kG-1,nG));
    jS(kS) = jG(ceil(kG/nG));
    cS(kS) = Ke(:);
    nS     = kS(end);
end
%--- Finally, give birth to the sparse global stiffness array.
K = sparse(iS(1:nS),jS(1:nS),cS(1:nS),nDof,nDof);

```

9 Summary of appended papers

In this section a brief summary of the appended papers is given.

Paper I. We present an adaptive finite element method for a cavitation model based on Reynolds equation. *A posteriori* error estimates and adaptive algorithms are derived, and numerical examples illustrating the theory are supplied. In order to incorporate into the model the fact that the lubricant cannot support sub-atmospheric pressure we formulate it as a variational inequality. To solve the cavitation problem numerically, we introduce a regularized version of the variational inequality using a penalty parameter tied to the local mesh size. Adaptivity is then based upon *a posteriori* error control in an energy-like norm. A method based on goal-oriented adaptive error control in general functionals of the solution is also presented.

Paper II. A lubrication model based on the more physically adequate Stokes equation, that, in comparison to the simplified Reynolds model, can

handle more demanding situations that comes with the computational domain at hand. We are using Crouzeix-Raviart element. The stability for the velocity gradient formulation used is fixed by adding contribution to the stiffness matrix from jumps over the element edges. For the Laplacian formulation a mathematical problem is that the pressure, as usual, is penalized as a limit process of the divergence of the vector field and does therefore not reside in the same function space as the pressure itself. We find a continuous pressure corrector that reside in the proper function space to be used in the Uzawa iteration algorithm. Adaptivity is then based upon *a posteriori* error control. A simplified error control that is an analogy with the Hencky problem in elastoplasticity is applied. Numerical results comparing the Stokes model with the Reynolds model are supplied.

Paper III. The Reynolds model modeled with mixed-finite element methods, i.e. different function spaces for the dependent variable and the fluxes. So, a given boundary problem is decomposed into two or more equivalent problems. It is crucial to select the combination of approximations for the flow variables and the pressure variable. We use the lowest order Raviart-Thomas approximation for the flux, which is known to be stable. Adaptive mesh refinement and error control is taken into account. The paper concludes with some numerical examples.

Paper IV. The Reynolds model is a reduced Stokes model, valid for narrow lubrication regions. In order to be able to handle non-narrow regions, there is a need to be able to transit to the more accurate Stokes model. A fundamental problem is how to couple the two models in a numerical simulation, preferably allowing for different meshes in the different domains. In this paper, we present a weak coupling method for Reynolds and Stokes models for lubrication computations. For the non-narrow region a mixed finite element method is used. The two meshes are glued together using 1D trace meshes and a Lagrange multiplier approach.

10 Future trends and ideas

The ultimate goal is to optimize the shape of the surface texture in order to tailor the surfaces to their expected field of application. To that extent we need to scrutinize the oil-pocket scenario even further and a more extensive physical model description is necessary, i.e. towards Navier-Stokes.

The coupling of Reynolds equation in narrow regions to the governing equations of the non-narrow regions containing a more elaborate model will be formulated as a discontinuous Galerkin problem followed by Nitsche's method [28], in order to glue the regions together along the internal boundaries.

There are also new and promising applications using oil-pocket techniques. One of them investigated experimentally at the moment is piston rings, where the lubricant model and the ring dynamics has to be solved simultaneously, i.e.,

$$\begin{cases} \nabla \cdot (h^3 \nabla p) = 6\mu U \frac{dh}{dx} + 12\mu \frac{dh}{dt} \\ m \frac{\partial^2 \bar{h}}{\partial t^2} = F(p) \end{cases} .$$

To sum up, a "functional analysis" approach to the scenario opens up for application in areas that at first sight seems to be completely different. For instance use of "oil-pocket" techniques on external surfaces of vehicles, such as cars, trains and aeroplanes, in order to reduce drag. In this case is one surface identified as the solid surface of the vehicle and the other one the onset flow. The "lubricated region" then corresponds to the boundary layer.

References

- [1] Alonso A., Dello Russo A., Padra C., Rodríguez, R., *An adaptive finite element scheme to solve fluid-structure vibration problems on non-matching grids*, Comput. Visual. Sci., 2001;**4**:67–78
- [2] Anno J. N., Walowit J. A., Allen C. M., *Microasperity lubrication*, Trans. ASME: J. Lub. Tech., 1968;**90**:351–355.
- [3] Archard J. F., *Contact and rubbing of flat surfaces*, J. Appl. Phys., 1953;**24**:981–988.
- [4] Bhushan B., *Principles and Applications of Tribology*, Wiley-Interscience, 1999.
- [5] Bowden F. P., Tabor D., *Friction and lubrication of solids, Vol I and II*, Oxford University Press, 1951 and 1964.
- [6] Brenner S. C., Scott L. R., *The mathematical theory of finite element methods*, 2nd ed., Springer, 2002.
- [7] Brenner S. C., *Korn's inequalities for piecewise H^1 vector fields*, Mathematics of Computation, 2004;**73**(247):1067–1087.
- [8] Brezzi F., Hager W. W., Raviart P.-A., *Error estimates for the finite element solution of variational inequalities. Part II. Mixed methods*, Numer. Math., 1978;**31**:1–16.

- [9] Capriz G., Cimatti G., *Free boundary problems in the theory of hydrodynamic lubrication: a survey*. In *Free Boundary Problems: Theory and Applications, Volume II*, (eds.) Fasano A., Primicerio, M., Pitman Boston, 1983;613–635.
- [10] Dowson D., *History of Tribology*, Longman New York, 1979.
- [11] Dowson D., Taylor C. M., *Fundamental aspects of cavitation in bearings*. In "Cavitation and related phenomena in lubrication", (eds.) Godet M., Taylor C. M., Proc 1st Leeds-Lyon Symposium on Tribology, Mechanical Engineering Publications, London, 1975.
- [12] Dyson A., *Air entrainment and boundary conditions in hydrodynamic lubrication*. In "Cavitation and related phenomena in lubrication", (eds.) Godet M., Taylor C. M., Proc 1st Leeds-Lyon Symposium on Tribology, Mechanical Engineering Publications, London, 1975.
- [13] Eriksson K., Estep D., Hansbo P., Johnson C., *Computational Differential Equations*, Studentlitteratur, Sweden, 1996.
- [14] Etsion I., Burstein I., *A model for mechanical seals with regular micro-surface structure*, Trib. Trans., 1996;**39**:677–683.
- [15] Etsion I., Kligerman Y., Halperin G., *Analytical and experimental investigation of laser-textured mechanical face seals*, Trib. Trans., 1999;**42**:511–516.
- [16] Floberg L., *On hydrodynamic lubrication with special reference to sub-cavity pressures and number of streamers in cavitation regions*, Acta Polytech. Scand. Ser., ME 19, 1965.
- [17] Floberg L., *Sub-cavity pressures and number of oil streamers in cavitation regions with special reference to the infinite journal bearing*, Acta Polytech. Scand. Ser., ME 37, 1968.
- [18] Floberg L., *Cavitation boundary conditions with regard to the number of streamers and tensile strength of the liquid*, In Conway-Jones J. M., Discussion. 1st Leeds-Lyon Symp. Cavitation Relat. Phenom. Lubr., pp 31–35. London, New York: Mech. Eng. Publ. Ltd., 1975.
- [19] Frêne J., Nicolas D., Degueurce B., Berthe D., Godet M., *Hydrodynamic lubrication*, Elsevier, Amsterdam, 1997.
- [20] Greenwood J. A., Williamson J. B. P., *Contact of Nominally Flat Surfaces*, Proc. Roy. Soc. London, 1966;**A295**:300–319.

- [21] Gumbel L., *Monatsblatter Berlin Bezirksver*, VDI, 1914;**5**.
- [22] Hamilton D. B., Walowit J. A., Allen C. M., *A theory of lubrication by microirregularities*, Trans. ASME: J. Basic Engng., 1966;**88**:177–185.
- [23] Hansbo P., Larsson M. G., *Discontinuous Galerkin and the Crouzeix-Raviart element: Application to elasticity*, ESAIM: Mathematical Modelling and Numerical Analysis, 2005;**37**(1):63–72.
- [24] Johnson C., *Adaptive finite element methods for the obstacle problem*, Mathematical Models and Methods in Applied Sciences, 1992;**2**:483–487.
- [25] Johnson K. L., *Contact Mechanics*, Cambridge Univ. Press, 1985.
- [26] Mizuno T., Okamoto M., *Effects of lubricant viscosity at pressure and sliding velocity on lubricating conditions in the compression-friction test on sheet metals*, Trans. ASME: J. Lub. Tech., 1982;**104**:53–59.
- [27] Nilsson B., *Adaptive finite element methods for the Reynolds thin film model with cavitation*, Lic. Eng. Thesis, Department of Applied Mechanics, Chalmers University of Technology, 2005.
- [28] Nitsche J. A., *Über ein Variationsprinzip zur Lösung Dirichlet-Problemen bei Verwendung von Teilräumen, die keinen Randbedingungen unterworfen sind*, Abhandlungen aus dem Mathematischen Seminar der Universität Hamburg, 1971;**36**:9–15.
- [29] Olsson K., *Cavitation in dynamically loaded bearings*, Trans. Chalmers University Tech. Gothenberg, 1965;**308**.
- [30] Lord Rayleigh, *On the pressure developed in a liquid during the collapse of a spherical cavity*, Phil. Mag., 1917, Sixth series, 34, 94.
- [31] Reynolds O., *On the theory of lubrication and its application to Mr Beauchamp Tower's experiments, including an experimental determination of the viscosity of olive oil*, Phil. Trans. Roy. Soc. London, 1886, Ser. A 177:157–233.
- [32] Salant R. F., Shen D., *Effects of shaft surface roughness on the hydrodynamics of rotary lip seals*, presented at 10th Nordic Symposium on Tribology, Stockholm, 2002.
- [33] Scholz R., *Numerical solution of the obstacle problem by the penalty method*, Computing 1984;**32**:297–306.

- [34] Sommerfeld, A., *Zur hydrodynamischen Theorie der Schmiermittelreibung*, Zeit. Math. Phys., 1904;**50**.
- [35] Stieber W., *Das Schwimmlager. Hydrodynamische Theorie des Gleitlagers*, VDI, Berlin, 1933.
- [36] Stribeck R., *Die wesentlichen Eigenschaften der Gleit- und Rollenlager*, Zeitschrift des VDI, 1902;**46,37**:1341–1348, 1432–1438, 1463–1470.
- [37] Swift H. W., *The stability of lubricating films in journal bearings*, Proc. Inst. Civ. Engrs., 1931;**233**:267–288.
- [38] Taylor C. M., *Separation cavitation in lightly loaded fluid film bearings with both surfaces in motion, Part I: Theoretical considerations, Part II: Analysis of the cylinder plane and journal bearings configurations*, J. Mech. Eng. Sci., 1974;**16**:147–155.
- [39] Wang X., Kato K., Adachi K., Aizawa, K., *The effect of laser texturing of SiC surface on the critical load for the transition of water lubrication mode from hydrodynamic to mixed*, Tribology Int., 2001;**34**:703–711.
- [40] Wu S. R., *A penalty formulation and numerical approximation of the Reynolds-Hertz problem of elastohydrodynamic lubrication*, International Journal of Engineering Science, 1984;**24**:1001–1013.

Paper I

Adaptive finite element methods for hydrodynamic lubrication with cavitation

Bertil Nilsson^{1,*},[†] and Peter Hansbo²

¹*Functional Surfaces Research Group, School of Business and Engineering,
Halmstad University, Halmstad, Sweden*

²*Department of Applied Mechanics, Chalmers University of Technology, Goteborg S-412 96, Sweden*

SUMMARY

We present an adaptive finite element method for a cavitation model based on Reynolds' equation. *A posteriori* error estimates and adaptive algorithms are discussed, and numerical examples illustrating the theory are supplied. Copyright © 2007 John Wiley & Sons, Ltd.

Received 31 May 2006; Revised 11 January 2007; Accepted 19 February 2007

KEY WORDS: Reynolds' equation; cavitation; finite element; penalty

1. INTRODUCTION

The motivation for this work is the need for accurate computations of the hydrostatic pressure in a lubricant entrapped between the tool and workpiece in a metal-forming process or in a sliding bearing. The ultimate goal is to be able to optimize the surface structure so as to take advantage of cavitation effects in the lubricant.

Often, the computations performed in order to assess the effects of surface pit geometries are based on highly simplified assumptions, see, e.g. Etsion *et al.* [1, 2], Wang *et al.* [3]. We propose to instead solve the full model numerically as part of an optimization loop. To this end, we here initiate a study of adaptive finite element modelling of hydrodynamic lubrication including cavitation effects. The cavitation will introduce steep pressure gradients that cannot be resolved on a coarse computational mesh. Consequently, an adaptive algorithm to automatically refine the mesh locally, based on error estimation, is crucial for accurate results. To our knowledge, the only

*Correspondence to: Bertil Nilsson, Functional Surfaces Research Group, School of Business and Engineering, Halmstad University, Halmstad, Sweden.

[†]E-mail: bertil.nilsson@set.hh.se

Contract/grant sponsor: The Swedish Foundation for Strategic Research through the ProViking Graduate School

paper dealing with adaptivity for this problem proper is Wu and Oden [4], where an *a priori* error estimate was used as error indicator. Using such an approach, the problem of unknown constants precludes accurate estimation of the error and allows only error *indication*, i.e. information about where the error is large (in a relative sense). We follow instead the *a posteriori* approach laid out in Johnson and Hansbo [5], and in particular Johnson [6], which deals with a problem closely related to ours (however, without numerical examples).

In this paper, we will focus on control of the error in energy-like norms (root-mean-square control of pressure gradients) and goal-oriented adaptive control for functionals of the error (e.g. of the pressure resultant).

The cavitation problem that we consider can be written as a variational inequality. We will use a penalty approach to reformulate the problem as a variational equality, and our adaptive algorithm will be closely tied to the penalty formulation. For a more general method for error control of variational inequalities, applicable also to the problem at hand, we refer to Suttmeier [7].

We emphasize that the basic theory for *a posteriori* error estimates for the problem at hand is not new but was given by Johnson [6] for energy norm and by French *et al.* [8] for pointwise errors. Our contribution lies in the more general error estimates, in the implementation details, and in the numerical examples.

2. THE CONTINUOUS PROBLEM

Consider a thin lubricant with viscosity μ enclosed between two surfaces Γ_1 and Γ_2 in relative motion. We assume that Γ_1 (identified with the xy -plane) is stationary and that Γ_2 moves with velocity $\mathbf{v} = (V, 0, 0)$. The Reynolds' equation can then be written as

$$-\nabla \cdot (H^3 \nabla P) = -6\mu V \frac{\partial H}{\partial x}$$

where $H(x, y)$ is the local thickness of the lubricant film, and P is the pressure. For the physical reasoning behind this model, see, e.g. Capriz and Cimatti [9]. We assume that P is zero at the boundaries of the domain Ω of interest (zero taken as the atmospheric pressure).

The lubricant cannot support subatmospheric pressure, so an additional condition is $P \geq 0$ in Ω . In order to incorporate this condition into the model, it is often written as a variational inequality as follows. Let c be a typical thickness of the film and set

$$p := \frac{Pc^2}{6\mu V}, \quad d := \frac{H}{c}, \quad \text{and} \quad f := -\frac{\partial d}{\partial x}$$

Then the cavitation model can be formulated as follows: let

$$K = \{v \in H_0^1(\Omega) : v \geq 0\}$$

and seek $p \in K$ such that

$$\int_{\Omega} d^3 \nabla p \cdot \nabla (v - p) \, d\Omega \geq \int_{\Omega} f(v - p) \, d\Omega \quad \forall v \in K \quad (1)$$

see [9].

In order to solve the cavitation problem numerically, we first introduce the following regularized version of (1): given a small penalty parameter $\varepsilon \in \mathbb{R}^+$, we seek $p_\varepsilon \in H_0^1(\Omega)$ such that

$$\int_{\Omega} d^3 \nabla p_\varepsilon \cdot \nabla v \, d\Omega + \int_{\Omega} d^3 \beta(p_\varepsilon) v \, d\Omega = \int_{\Omega} f v \, d\Omega \quad \forall v \in H_0^1(\Omega) \tag{2}$$

where

$$\beta(s) = \begin{cases} 0, & s \geq 0 \\ s/\varepsilon, & s < 0 \end{cases}$$

This formulation was studied by Scholz [10] in the context of obstacle problems, and was used as a starting point for formulating *a posteriori* error estimates by Johnson [6] (see also Wu [11] for application to the problem at hand). From [10], we know that the solution of (2) converges to the solution of (1) in the sense that

$$\int_{\Omega} d^3 |\nabla p - \nabla p_\varepsilon|^2 \, d\Omega \leq C \varepsilon \int_{\Omega} f^2 \, d\Omega$$

The idea used in [6, 10] was to tie ε to the mesh size h in a finite element method for solving (2). In order to make dimensional sense (which is important for the conditioning of the discrete system of equations), it is clear that $\varepsilon \sim h^2$, in which case the error in the penalty formulation is of the same order as the discretization error of a linear finite element method. Thus, this approach is best suited for low-order finite element methods (linear and bilinear). For higher-order finite elements, we will either have a penalty error dominating the discretization error or, alternatively, with $\varepsilon \sim h^q$, $q > 2$, obtain a badly conditioned system of equations.

3. FINITE ELEMENT APPROXIMATION

3.1. Formulation

Let $\mathcal{T} = \{T\}$ be a locally quasiuniform triangulation of Ω into simplexes T of local mesh size h (in the following regarded as a piecewise constant function such that $h(x) = h|_T$ for $x \in T$) and let

$$V_h = \{v \in H_0^1(\Omega) : v|_T \in P^1(T), \forall T \in \mathcal{T}\}$$

i.e. we will use constant-strain triangles. Furthermore, we will tie the penalty parameter ε to the local mesh size, following [6, 10], according to $\varepsilon = \gamma^{-1} h^2$, where γ is a constant.

We seek $p_h \in V_h$ such that

$$\int_{\Omega} d^3 \nabla p_h \cdot \nabla v \, d\Omega + \int_{\Omega} d^3 \beta(p_h) v \, d\Omega = \int_{\Omega} f v \, d\Omega \quad \forall v \in V_h \tag{3}$$

or, explicitly,

$$\int_{\Omega} d^3 \nabla p_h \cdot \nabla v \, d\Omega + \int_{\Omega} d^3 \gamma h^{-2} p_h^- v \, d\Omega = \int_{\Omega} f v \, d\Omega \quad \forall v \in V_h \tag{4}$$

where we used the notation

$$w^- := \min(w, 0)$$

This non-linear problem we solved iteratively using fixed-point iterations. We lumped the mass matrix resulting from the penalty term using nodal quadrature, and the condition $p_h \geq 0$ was checked nodewise. In all nodes where $p_h < 0$, penalty was applied.

3.2. A posteriori error control in the natural norm

We consider error control in the natural norm induced by the finite element formulation, following Johnson [6], denoted by $e = p_\varepsilon - p_h$. We have the following *a posteriori* error representation

$$\|d^{3/2}\nabla e\|_{L_2(\Omega)} + \|d^{3/2}\gamma^{1/2}h^{-1}e^-\|_{L_2(\Omega)} \leq C_1 \sum_{T \in \mathcal{T}} \rho_T + C_2 \sum_{T \in \mathcal{T}} \rho_{\partial T} \quad (5)$$

where

$$\rho_T = h \|f + \nabla \cdot (d^3 \nabla p_h) - d^3 \gamma h^{-2} p_h^-\|_{L_2(T)}$$

$$\rho_{\partial T} = \frac{1}{2} h^{1/2} \|d^3 [\mathbf{n} \cdot \nabla p_h]\|_{L_2(\partial T)}$$

with $[\mathbf{n} \cdot \nabla p_h]$ denoting the jump in normal derivative across element sides ∂T , and

$$[v] = \begin{cases} v^+ - v^- & \text{on } \partial T_{\text{int}}, \\ v^+ & \text{on } \partial T_{\partial \Omega}, \end{cases} \quad v^\pm = \lim_{\delta \downarrow 0} v(\mathbf{x} \mp \delta \mathbf{n}_T)$$

This is a consequence of the following argument, given in [6]. We first note the orthogonality relation

$$\int_{\Omega} d^3 \nabla e \cdot \nabla v \, d\Omega + \int_{\Omega} d^3 \gamma h^{-2} e^- v \, d\Omega = 0 \quad \forall v \in V_h \quad (6)$$

Then, with π_h a suitable interpolant (e.g. that of Clément [12]) onto V_h , and using the monotonicity of $v \mapsto v^-$,

$$(v^- - w^-)(v - w) \geq (v^- - w^-)^2$$

we have

$$\begin{aligned} \|d^{3/2}\nabla e\|_{L_2(\Omega)}^2 + \|d^{3/2}\gamma^{1/2}h^{-1}e^-\|_{L_2(\Omega)}^2 &= \int_{\Omega} d^3 |\nabla e|^2 \, d\Omega + \int_{\Omega} d^3 \gamma h^{-2} |e^-|^2 \, d\Omega \\ &\leq \int_{\Omega} d^3 |\nabla e|^2 \, d\Omega + \int_{\Omega} d^3 \gamma h^{-2} e^- e \, d\Omega \\ &= \int_{\Omega} d^3 \nabla p_\varepsilon \cdot \nabla e \, d\Omega + \int_{\Omega} d^3 \gamma h^{-2} p_\varepsilon^- e \, d\Omega \\ &\quad - \int_{\Omega} d^3 \nabla p_h \cdot \nabla e \, d\Omega - \int_{\Omega} d^3 \gamma h^{-2} p_h^- e \, d\Omega \\ &= \int_{\Omega} f e \, d\Omega - \int_{\Omega} d^3 \nabla p_h \cdot \nabla e \, d\Omega - \int_{\Omega} d^3 \gamma h^{-2} p_h^- e \, d\Omega \end{aligned}$$

$$\begin{aligned}
 &= \int_{\Omega} f(e - \pi_h e) \, d\Omega - \int_{\Omega} d^3 \nabla p_h \cdot \nabla(e - \pi_h e) \, d\Omega \\
 &\quad - \int_{\Omega} d^3 \gamma h^{-2} p_h^- (e - \pi_h e) \, d\Omega
 \end{aligned}$$

Using integration by parts followed by Cauchy’s inequality and interpolation estimates yielding the constants

$$C_1 = \sup_{v \in H_0^1(\Omega)} \frac{h^{-1} \|v - \pi_h v\|_{L_2(T)}}{\|d^{3/2} \nabla v\|_{L_2(T)}}, \quad C_2 = \sup_{v \in H_0^1(\Omega)} \frac{h^{-1/2} \|v - \pi_h v\|_{L_2(\partial T)}}{\|d^{3/2} \nabla v\|_{L_2(T)}}$$

the error representation formula (5) follows.

It is clear that the constants C_1 and C_2 cannot be computed exactly, but they may be estimated as approximate solutions to the eigenvalue problem of finding $u \in H^1(K)$ and $\lambda \in \mathbb{R}$ such that

$$\lambda \int_T d^3 \nabla u \cdot \nabla v \, dx = \int_T (u - \pi_h u)(v - \pi_h v) \, dx \quad \forall v \in H^1(K)$$

Then C_1 is given by $C_1 = \sqrt{\lambda_{\max}}/h$; C_2 is computed analogously. (For this computation, it is easier to let π_h denote the nodal interpolant, which, however, requires more smoothness than that assumed in the interpolation estimate in order to make sense, see [12]. This is a technical point of no practical importance in the current context.) For example, on an equilateral triangular element with $H^1(K)$ replaced by $P^2(K)$, and assuming d constant and $h := \sqrt{2 \operatorname{meas}(T)}$, we find

$$C_1 \approx 0.501d^{-3/2}, \quad C_2 \approx 0.635d^{-3/2}$$

3.3. Goal-oriented a posteriori error control

We next consider error control for functionals of the error, or ‘quantities of interest’, following Becker and Rannacher [13]. The total error in this approach is found as the product of two terms:

1. The residual, obtained by plugging the finite element solution into the differential equation. This quantity measures the inability of the finite element solution to solve the equation in a pointwise sense and is completely local.
2. The solution z of a linearized continuous dual problem; a generalized Green’s function (a.k.a. influence function) which gives information about the effect of the local error upon the quantity of interest.

The important questions to address in this context are the linearization of the dual problem and the computation of the dual solution z . In the following, we will discuss different ways to deal with these questions. We begin with a brief description of the goal-oriented approach in the present setting.

Denote by $e = p_\varepsilon - p_h$ and $e_\beta = \beta(p_\varepsilon) - \beta(p_h)$. Defining the residual $R \in H^{-1}(\Omega)$ by

$$\langle R, v \rangle := \int_{\Omega} f v \, d\Omega - \int_{\Omega} d^3 \nabla p_h \cdot \nabla v \, d\Omega - \int_{\Omega} d^3 \beta(p_h) v \, d\Omega \quad \forall v \in H_0^1(\Omega) \tag{7}$$

where $\langle \cdot, \cdot \rangle$ denotes duality pairing, we have the following error equation:

$$\int_{\Omega} d^3 \nabla e \cdot \nabla v \, d\Omega + \int_{\Omega} d^3 e_{\beta} v \, d\Omega = \langle R, v \rangle \quad \forall v \in H_0^1(\Omega) \quad (8)$$

and the orthogonality property

$$\int_{\Omega} d^3 \nabla e \cdot \nabla v \, d\Omega + \int_{\Omega} d^3 e_{\beta} v \, d\Omega = 0 \quad \forall v \in V_h \quad (9)$$

In order to estimate functionals of the error, we follow [5, 13] and argue by duality as follows. For brevity of notation, assume that we have a general non-linear variational problem: find $p \in V$ such that

$$\int_{\Omega} A(p)v \, d\Omega = \int_{\Omega} f v \, d\Omega \quad \forall v \in V$$

and a FEM counterpart: find $p_h \in V_h$ such that

$$\int_{\Omega} A(p_h)v \, d\Omega = \int_{\Omega} f v \, d\Omega \quad \forall v \in V_h$$

We then have the following Galerkin orthogonality property:

$$\int_{\Omega} (A(p) - A(p_h))v \, d\Omega = 0 \quad \forall v \in V_h$$

or

$$\int_{\Omega} B \cdot (p - p_h)v \, d\Omega = 0 \quad \forall v \in V_h$$

where

$$B := \int_0^1 A'(\xi p + (1 - \xi)p_h) \, d\xi \quad (10)$$

Note that B constitutes an *exact* linearization, since

$$\int_0^1 \frac{d}{d\xi} A(\xi p + (1 - \xi)p_h) \, d\xi = [A(\xi p + (1 - \xi)p_h)]_0^1 = A(p) - A(p_h)$$

and

$$\int_0^1 \frac{d}{d\xi} A(\xi p + (1 - \xi)p_h) \, d\xi = \int_0^1 A'(\cdot) \frac{d}{d\xi} (\xi p + (1 - \xi)p_h) \, d\xi = B \cdot (p - p_h)$$

Next, we must define a linearized dual continuous problem as follows: find z such that

$$B^T \cdot z = g$$

where g can be chosen freely, and where B^T is the adjoint of B , defined by

$$\int_{\Omega} B^T \cdot p v \, d\Omega = \int_{\Omega} p B \cdot v \, d\Omega$$

for all $p \in V$ and $v \in V$. Then

$$\begin{aligned}
 \int_{\Omega} (p - p_h) g \, d\Omega &= \int_{\Omega} (p - p_h) B^T \cdot z \, d\Omega \\
 &= \int_{\Omega} B \cdot (p - p_h) z \, d\Omega \\
 &= \int_{\Omega} (A(p) - A(p_h)) z \, d\Omega \\
 &= \int_{\Omega} (f - A(p_h))(z - \pi_h z) \, d\Omega
 \end{aligned} \tag{11}$$

To obtain an error estimate involving a quantity of interest, a suitable g must be chosen. In our case we are interested in the error in the pressure resultant, in which case $g = 1$ is the proper choice. We note also that in a scalar case B can be computed directly by

$$B = \frac{A(p) - A(p_h)}{p - p_h} \quad \text{if } p - p_h \neq 0, \quad B = 0 \quad \text{otherwise} \tag{12}$$

However, computing B exactly still requires knowledge of the exact solution and two possible practical strategies are:

- Use the rectangle rule for computing the integral in (10) to obtain $B(p, p_h) \approx A'(p_h)$. This is usually an inexpensive method since A' is represented by the Newton matrix which is normally computed anyway in a non-linear iteration scheme, but it does introduce a rather severe linearization error.
- Compute an improved approximation p_h^* of p and use $B(p, p_h) \approx B(p_h^*, p_h)$. This requires a substantial additional computational effort since p_h^* is computed to a higher accuracy than p_h . Of course, p_h^* can then be used as the solution used for design purposes, but technically the error is computed for p_h , not p_h^* . If we want to be economical, we then need some information as to how much the error decreases going from p_h to p_h^* which may not be so easy to come by.

In this paper we shall consider and compare these two strategies applied to the lubrication problem.

Approximate linearization: Here we introduce the adjoint problem of finding $z \in H_0^1(\Omega)$ such that

$$\int_{\Omega} d^3 \nabla z \cdot \nabla v \, d\Omega + \int_{\Omega} \beta'(p_h) z v \, d\Omega = \int_{\Omega} g v \, d\Omega \quad \forall v \in H_0^1(\Omega) \tag{13}$$

for a given g , where we note that

$$\beta'(p_h) = \begin{cases} 0, & p_h \geq 0 \\ \varepsilon^{-1}, & p_h < 0 \end{cases}$$

'Exact' linearization: Here we use (12) and search $z \in H_0^1(\Omega)$ such that

$$\int_{\Omega} d^3 \nabla z \cdot \nabla v \, d\Omega + \int_{\Omega} b z v \, d\Omega = \int_{\Omega} g v \, d\Omega \quad \forall v \in H_0^1(\Omega) \quad (14)$$

where

$$b(x) = \begin{cases} d^3 e_{\beta}(x)/e(x) & \text{if } e(x) \neq 0 \\ 0 & \text{if } e(x) = 0 \end{cases}$$

and we note that $0 \leq b \leq d^3/\varepsilon$. This idea was introduced by French *et al.* [8] to obtain maximum norm control of the error for a closely related problem.

Having solved the dual problem numerically, we make the specific choice of $v = e$ and deduce, following (11), that

$$\int_{\Omega} g e \, d\Omega \approx \int_{\Omega} f(z - \pi_h z) \, d\Omega - \int_{\Omega} d^3 \nabla p_h \cdot \nabla(z - \pi_h z) \, d\Omega - \int_{\Omega} d^3 \beta(p_h)(z - \pi_h z) \, d\Omega \quad (15)$$

This relation is then used for both the approximate and exact linearization cases.

The strategy for numerical evaluation of the error is now as follows. In order to solve (14) approximately, we need to approximate b . This we do by solving the problem (3) on two meshes, the one used to compute p_h and one where all elements have been divided once more. On the finer mesh, we also solve the dual problem (14) or, in case of the approximate linearization, (13). This is done in order to evaluate approximately $z - \pi_h z$. For indication of which elements that are to be refined, we note that the integral over Ω can be written as a sum of element integrals. The size of the element integrals is then used as an indicator; we refine the 30% of the elements with the highest indicator in each adaptive step. We shall in particular be concerned with the choice $g = 1$, since this gives us the error in the pressure resultant. The pressure resultant is the quantity of interest in the lubrication problem; the ultimate goal is to optimize the pit geometries in such a way as to maximize this quantity.

4. NUMERICAL EXAMPLES

In order to investigate the performance of the methods proposed, a few numerical examples will be presented. Unfortunately, experimental results demonstrating in detail the local behaviour of the pressure image is, to our knowledge, not published. Though some integrated experimental results, such as lift, has been given by Etsion *et al.* [1, 2] and Wang *et al.* [3].

The only parameter involved in the algorithm and used in the numerical calculations is γ , the global constant which ties the penalty parameter ε to the local mesh size, according to $\varepsilon = \gamma^{-1} h^2$. We remark that, since $h \rightarrow 0$ as the mesh is refined, the strength of the penalty increases automatically in areas where the mesh is refined. These are also the areas in which the error contribution is estimated to be large. In all examples that follow we set $\gamma = 1000$. An important strength of the method is that γ is just a potentiometer for speed of convergence and does not influence the final solution. All integrals involved are integrated using two-point Gauss quadrature. The characteristic channel height c is in all examples defined to be equal to the nominal channel height and all other unimportant scaling parameters is chosen so that the product $6\mu V := 1$.

4.1. One-dimensional chain-tooth

We consider a simple one-dimensional chain-tooth according to Figure 1. The geometry of the tooth is simply a half square and the channel height is twice the peak height of the tooth. The boundary conditions are $p = 0$ at the inlet and outlet of the domain.

A comparison between a pure Reynolds solution and the adaptive finite element cavitation method with *a posteriori* error control in the natural norm is given in Figure 2. We can see that we essentially reconstruct the behaviour of the classical solution when the continuity boundary conditions are applied. The important note is of course that we do not need to *a priori* define the boundary location between the fluid and cavitation phases. As can be seen in Figure 2, the classical approach of first computing p^R from a pure Reynolds solution, followed by approximating $p \approx \max(0, p^R)$ (known as the half-Sommerfeld condition, cf. [14]) is not very accurate.

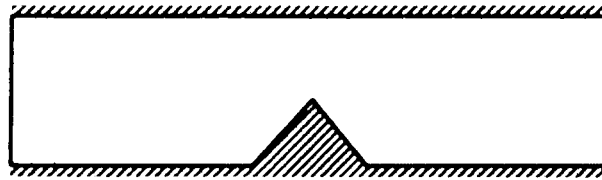


Figure 1. One-dimensional tooth model.

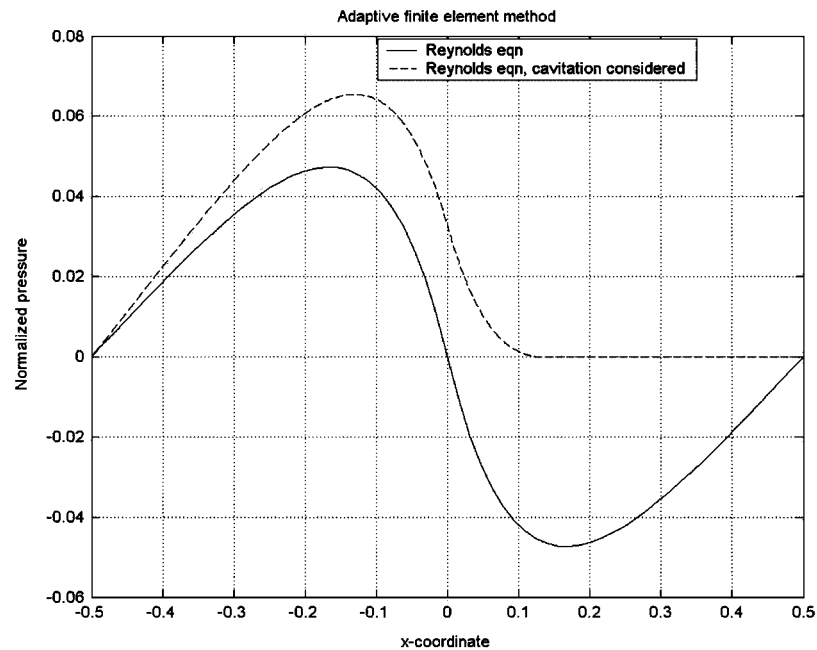


Figure 2. One-dimensional tooth model. Comparison of pure Reynolds solution with proposed cavitation model.

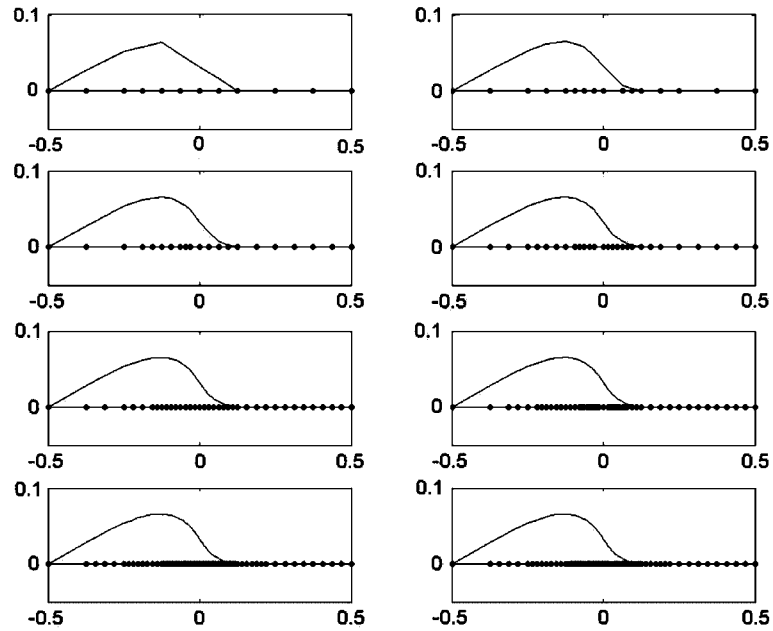


Figure 3. One-dimensional tooth model. Adaptivity refinement progress.

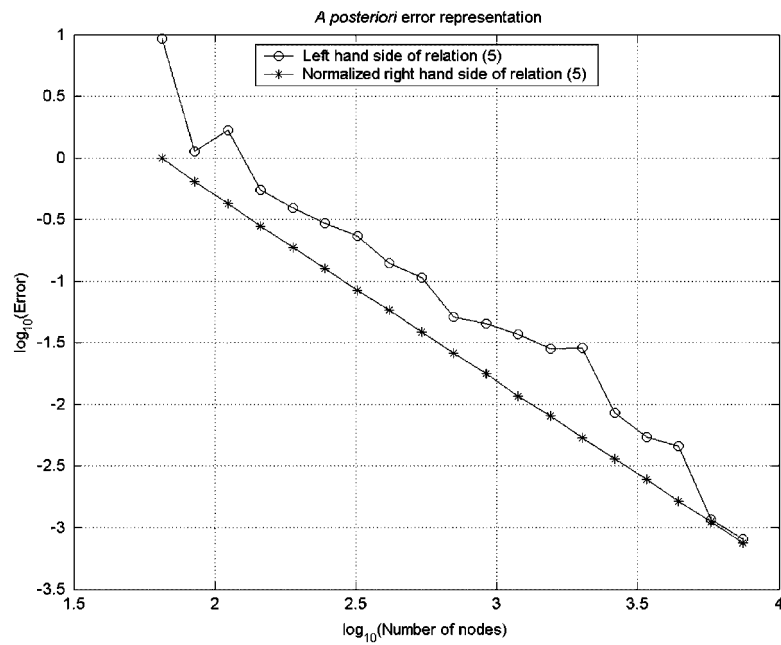


Figure 4. One-dimensional tooth model. Convergence of *a posteriori* error representation according to relation (5).

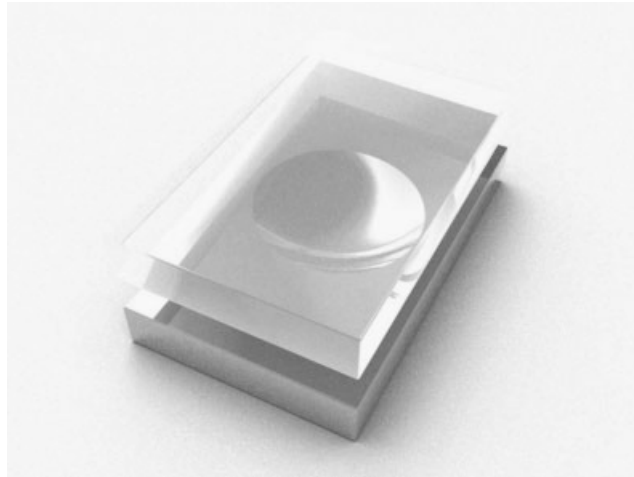


Figure 5. Hemi-spherical oil-pocket model.

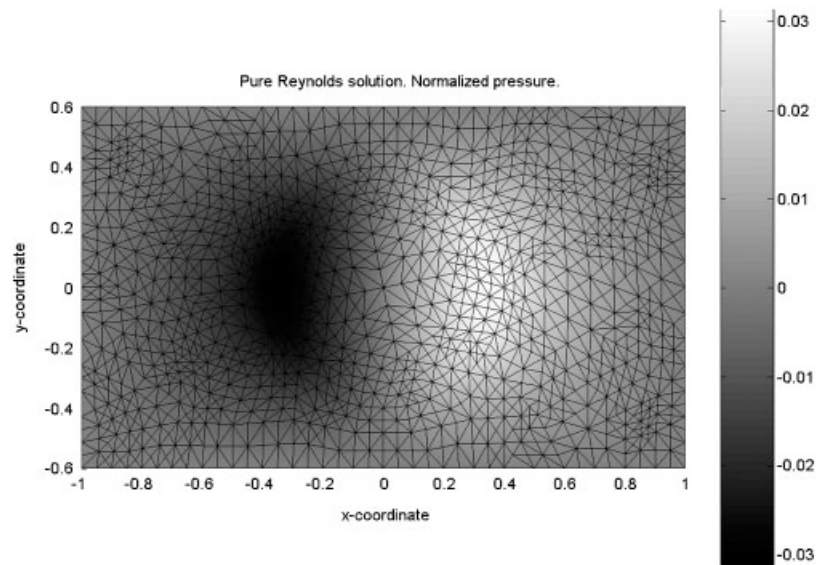


Figure 6. Hemi-spherical oil-pocket model. Pure Reynolds solution on a coarse mesh.

In Figure 3 we visualize the adaptivity refinement progress inserting new nodes. In each step, the elements that give the largest third of the element contributions to the total *a posteriori* error according to relation (5) are subdivided into two new ones. The decrease of the total error according to refinement, measured by the number of nodes, is presented in Figure 4.

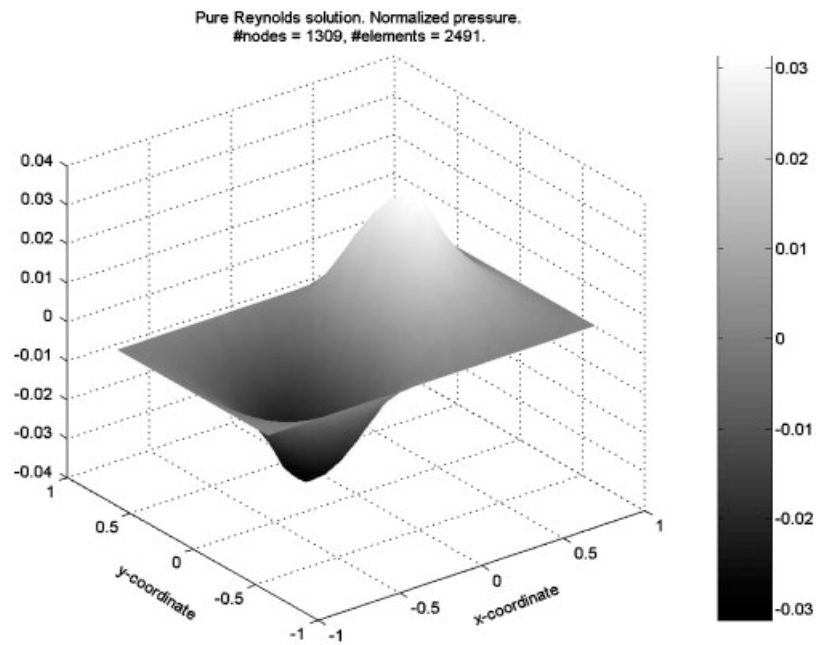


Figure 7. Hemi-spherical oil-pocket model. Pure Reynolds solution on a semi-fine mesh.

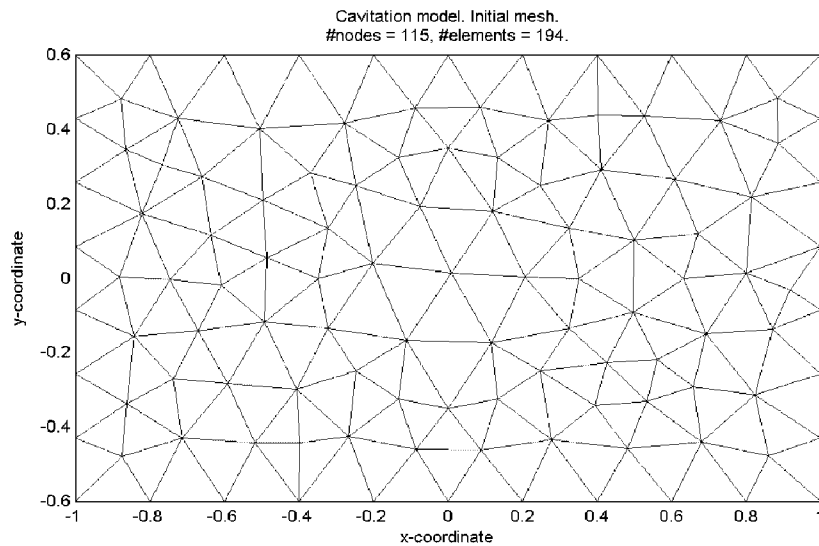


Figure 8. Cavitation model. Initial mesh.

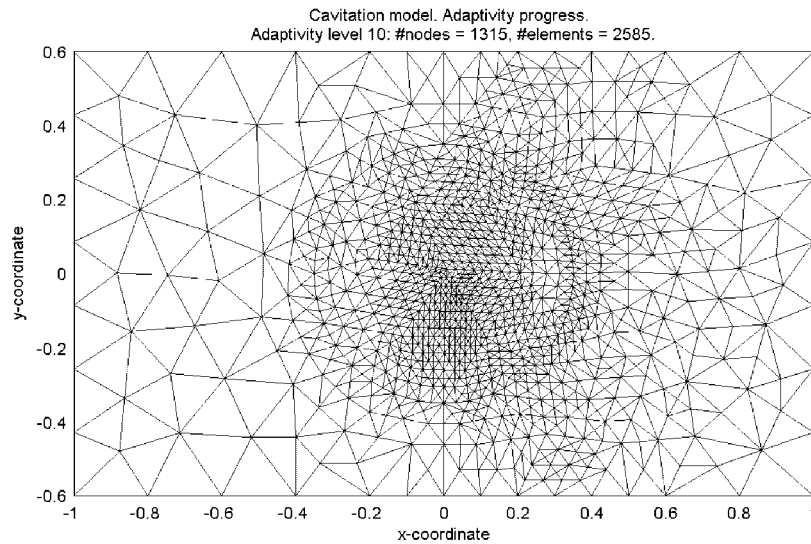


Figure 9. Hemi-spherical oil-pocket model. Adaptivity progress.

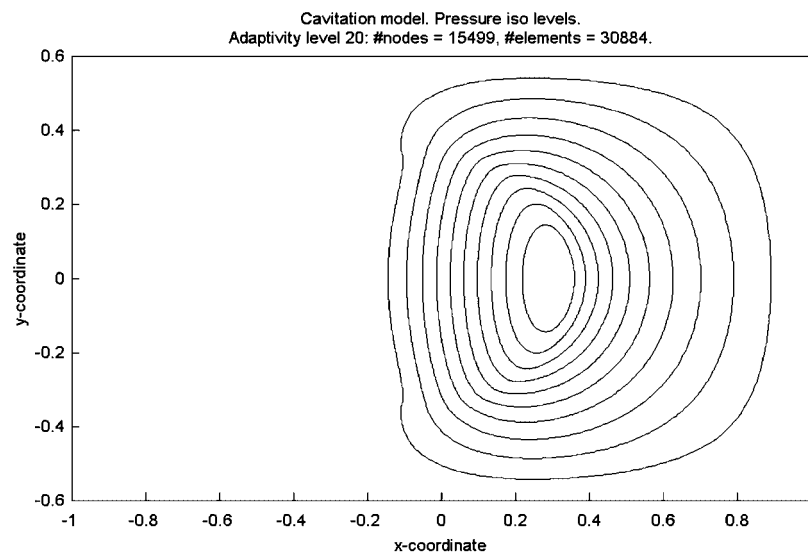


Figure 10. Hemi-spherical oil-pocket model. Pressure iso levels.

4.2. Two-dimensional oil-pocket

We consider a two-dimensional oil-pocket in the shape of a hemi-sphere, Figure 5. The geometry is furnished as follows. The channel height is twice the impact depth and half of the impact radius. Boundary condition is $p = 0$ on external boundary of the domain.

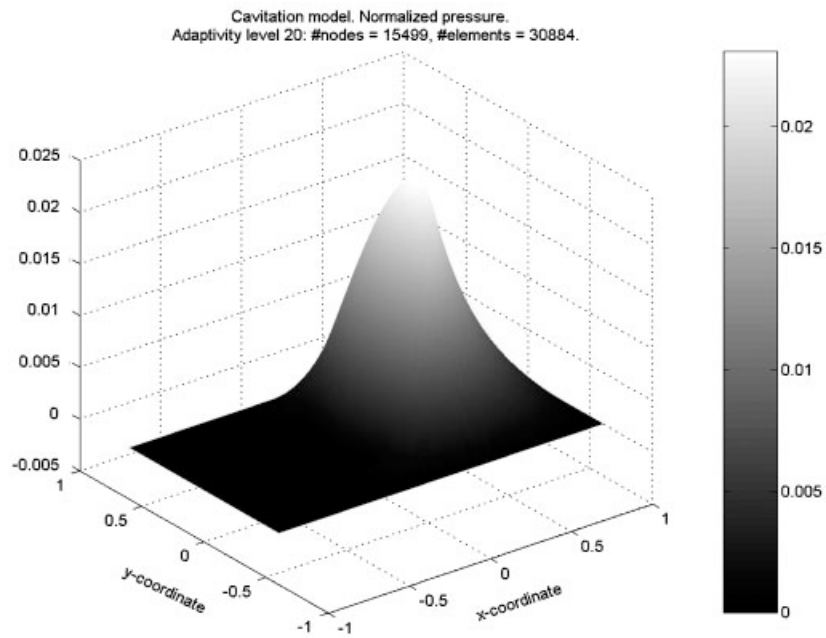


Figure 11. Hemi-spherical oil-pocket model. Cavitation model, solution on a fine mesh.

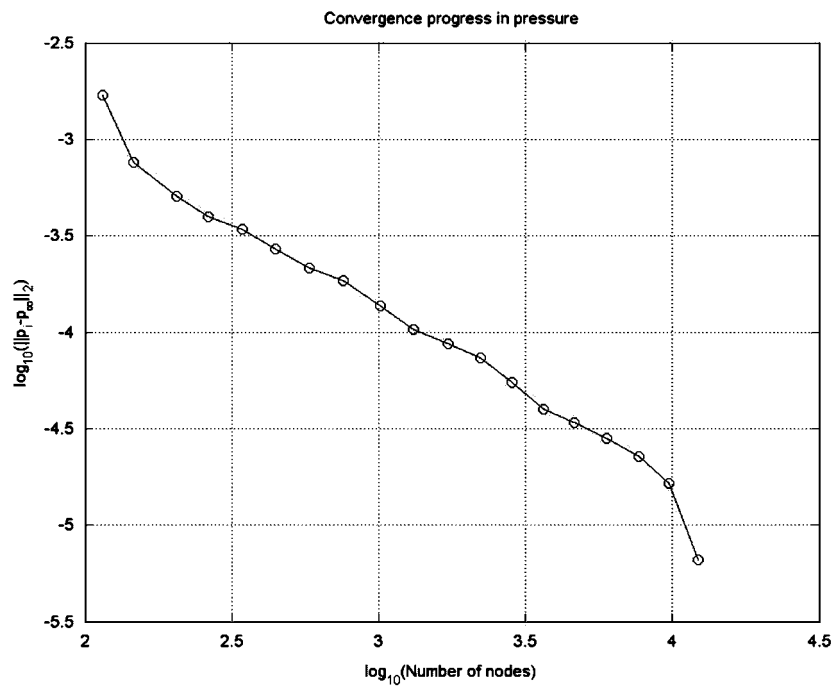


Figure 12. Hemi-spherical oil-pocket model. Cavitation model, convergence of pressure in natural norm.

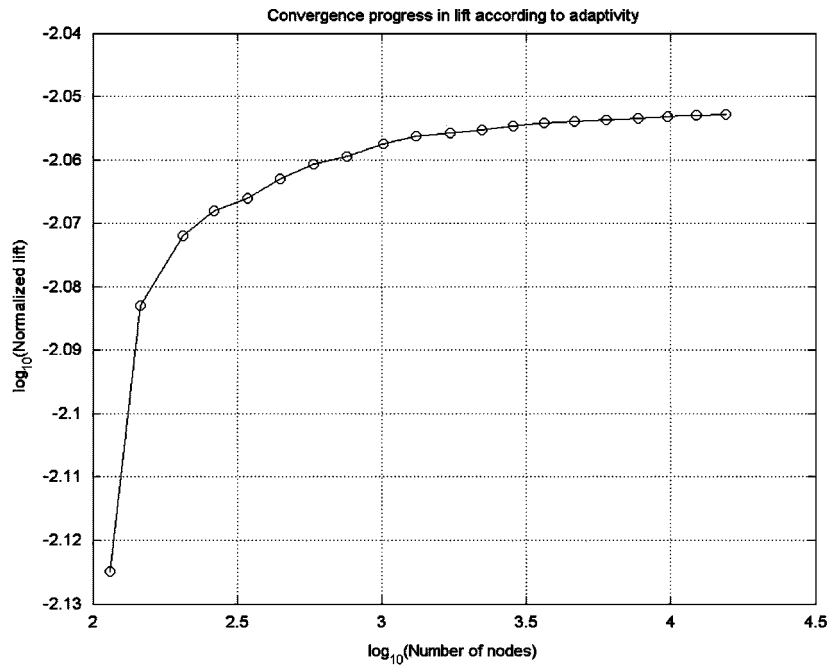


Figure 13. Hemi-spherical oil-pocket model. Cavitation model, convergence of lift.

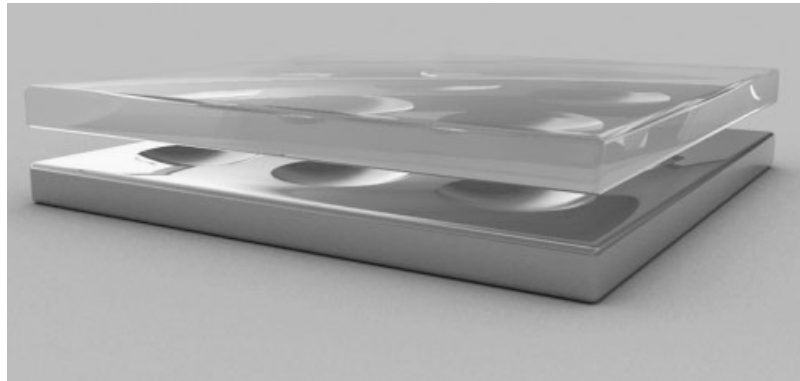


Figure 14. Infinite array of pockets.

First a pure Reynolds solution on a coarse mesh, Figure 6, followed by solution on a semi-fine one, Figure 7.

The following four Figures 8–11 illustrate error control in the natural norm starting with the initial mesh and after adaptive refinement step 20. We can clearly see the focus towards regions with high gradients in the solution as a result of the error-oriented adaptive refinement process.

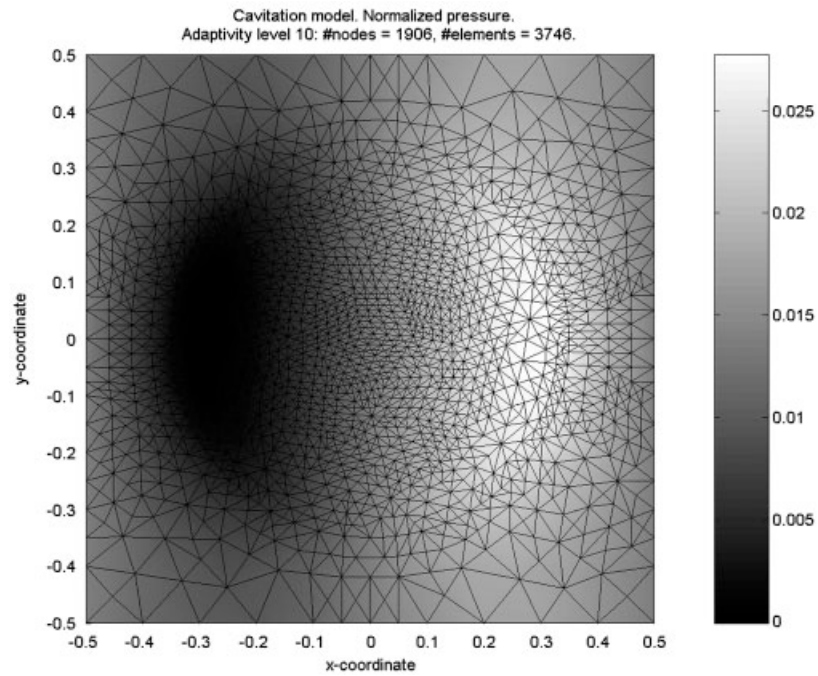


Figure 15. Infinite array of pockets. Cavitation model, pressure distribution in one cell.

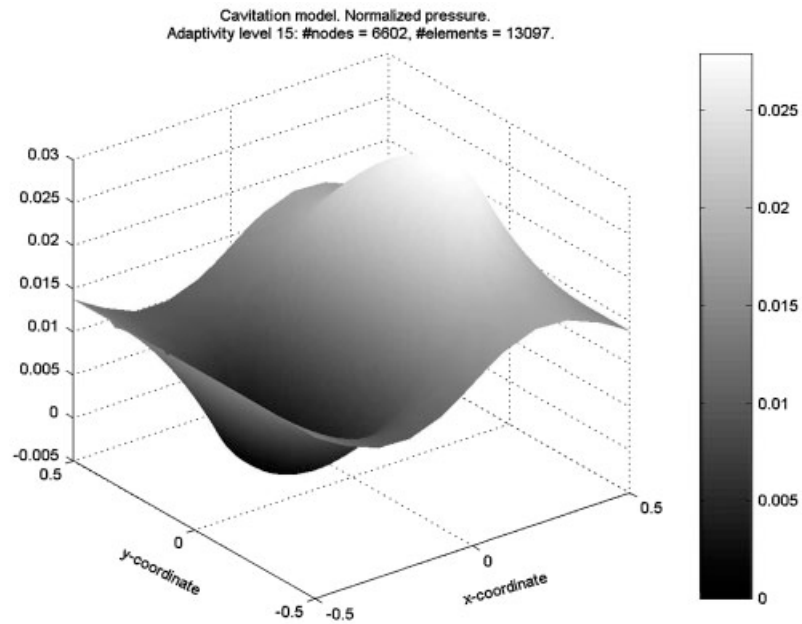


Figure 16. Infinite array of pockets. Cavitation model, pressure distribution in one cell.

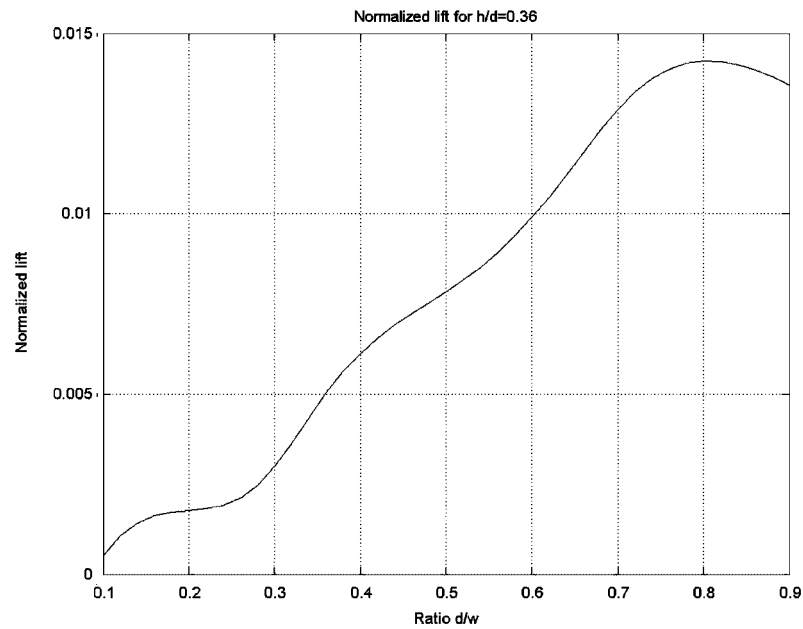


Figure 17. Infinite array of pockets. Cavitation model, lift as function of area ratio d/w .

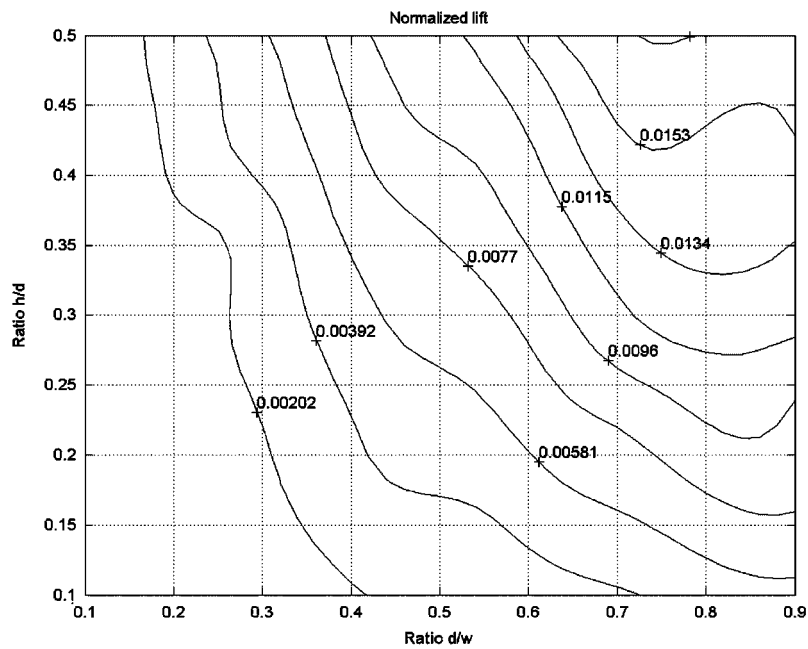


Figure 18. Infinite array of pockets. Cavitation model, contour plot of lift according to area ratio d/w and depth/diameter ratio h/d .

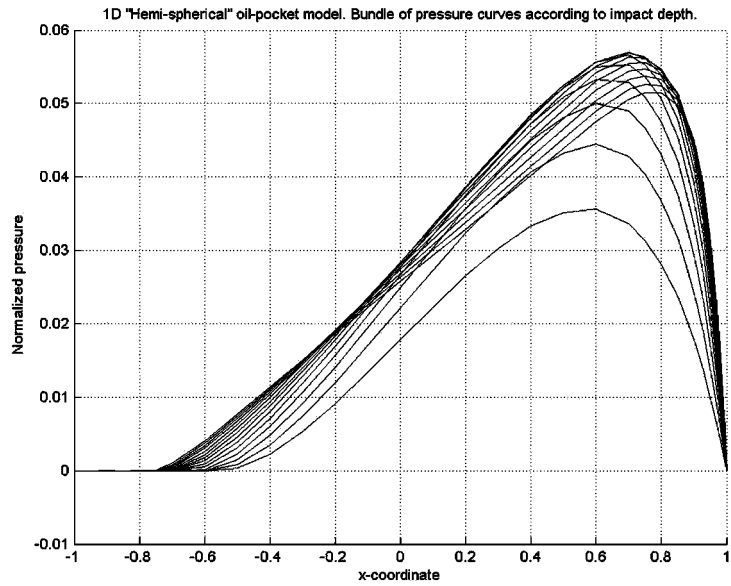


Figure 19. One-dimensional 'hemi-spherical' oil-pocket model. Bundle of pressure curves according to impact depth.

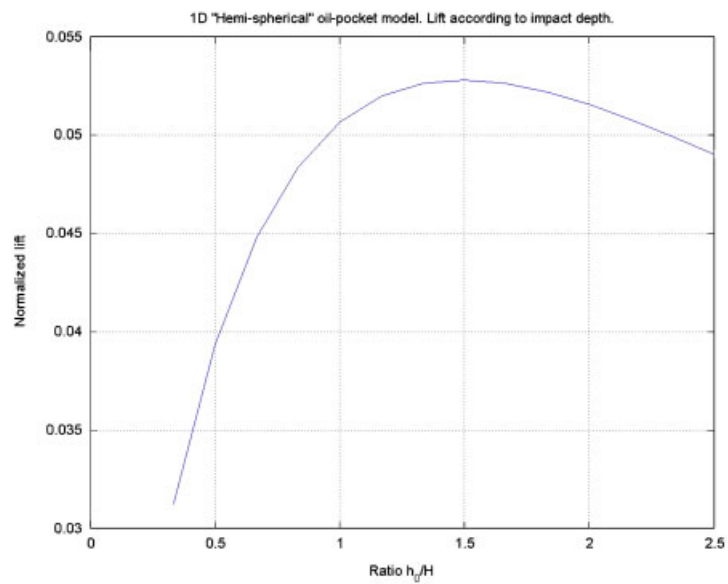


Figure 20. One-dimensional 'hemi-spherical' oil-pocket model. Lift according to impact depth.

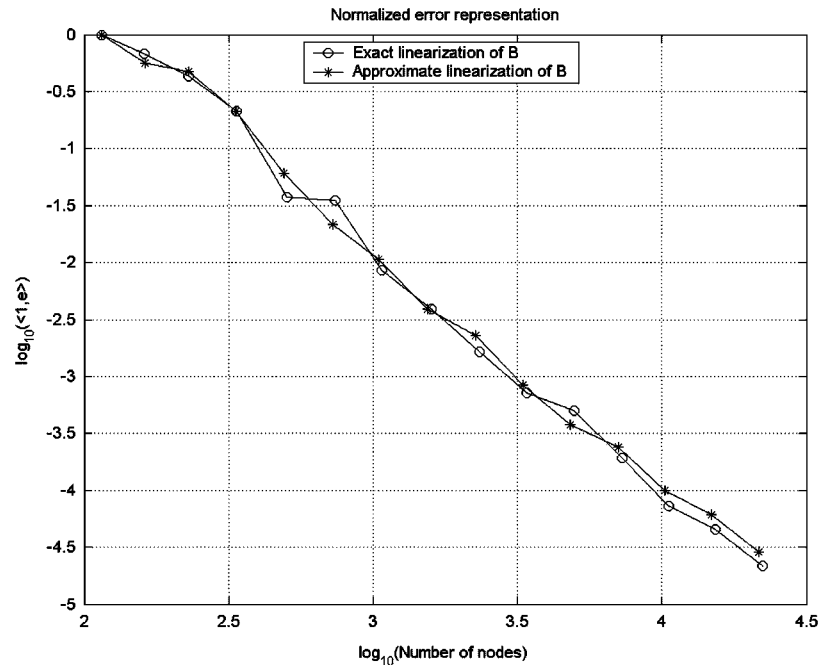


Figure 21. Hemi-spherical oil-pocket model. Convergence of residual error representation according to relation (15). Each dot represents an adaptive step.

The convergence of the pressure solution in the natural norm is shown in Figure 12, and the convergence of lift in Figure 13.

4.3. Optimization of two-dimensional oil-pocket area ratio

We consider the same two-dimensional single oil-pocket layout as in the previous example, but now assembled as an infinite array of quadrilateral cells, containing one centred pocket each, Figure 14.

Our aim is to investigate how the lift is influenced by the size and depth of the oil-pocket. One cell is considered and cyclic boundary conditions are imposed using multipoint constraints in order to simulate the infinite array. The analysis is summarized in Figures 15–18. In the last figure, d/w denotes the oil-pocket impact diameter over cell width and h/d is the oil-pocket impact depth over diameter. Inspecting Figure 17 we can identify an optimal impact diameter but hardly do the same for the impact depth, which, however, is clearly identifiable in a one-dimensional setting as evident in the last two figures: in Figure 19 the pressure curves for increasing impact depth clearly indicate a certain depth better than the others; the total lift as function of centre impact depth over nominal clearance between the surfaces accompanies the scenario, Figure 20. The worrisome question as to why the two-dimensional case is less predictive than the one-dimensional has to be left as an open question for the moment (cf. Section 5).

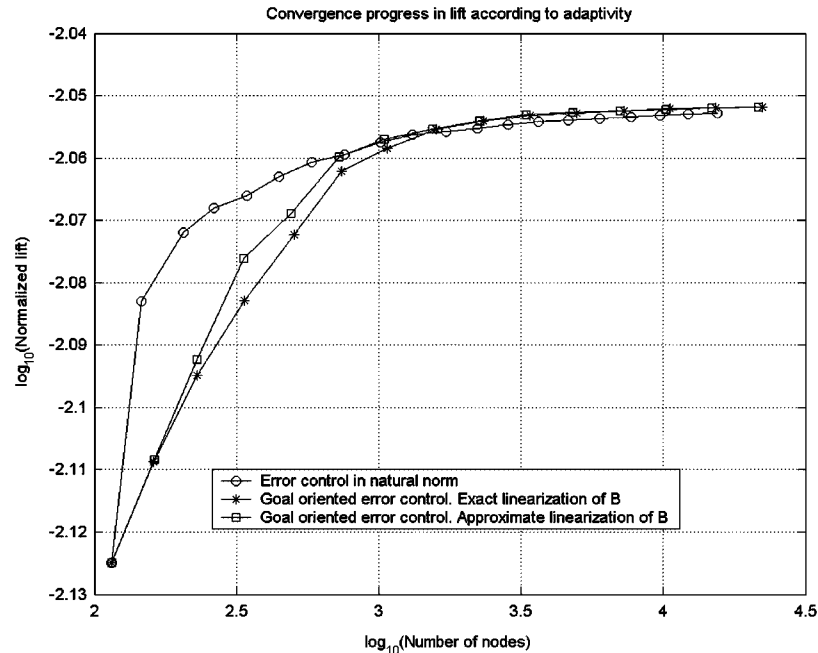


Figure 22. Hemi-spherical oil-pocket model. Convergence in lift. Each dot represents an adaptivity step.

4.4. Goal-oriented a posteriori error control and comparison

We consider again the two-dimensional oil-pocket with the shape of a hemi-sphere, Figure 5. In Figure 21 we present the decrease of the total residual error $\langle 1, e \rangle$ representation given in relation (15) relative to the number of nodes, for the two different strategies to compute the tangent matrix B . Finally, in Figure 22 we compare, relative to the convergence in lift, the formulation of error control in the natural norm with the two goal-oriented strategies.

5. DISCUSSION

As expected, the goal-oriented finite element method is more effective in predicting the lift even for a rather coarse mesh. On the other hand, more work is needed at each refinement step for the goal-oriented method, so it is not obvious to judge if one method is in favour over the other. Error estimation in the natural norm cannot give us information about the error in lift, but if the change in computational lift is monitored separately, the simpler natural norm adaptivity must, for our purposes, be considered sufficiently good for adapting the mesh.

In order to optimize and fully investigate the shape of the oil-pockets, our results indicate that the two-dimensional model does not have a good predictive quality. This we conjecture depends on the shortcomings of the Reynolds thin film model. We believe that the simulations must rely on more accurate modelling, using incompressible Stokes or Navier–Stokes flow, at least in regions with rapidly varying height. Thus, future work will focus on the coupling of narrow regions with relative non-narrow regions (e.g. oil-pockets) using different physical models.

REFERENCES

1. Etsion I, Burstein L. A model for mechanical seals with regular microsurface structure. *Tribology Transactions* 1996; **39**:677–683.
2. Etsion I, Kligerman Y, Halperin G. Analytical and experimental investigation of laser-textured mechanical seal faces. *Tribology Transactions* 1999; **42**:511–516.
3. Wang X, Kato K, Adachi A, Aizawa K. Load carrying capacity map for the surface texture design of SiC thrust bearing sliding in water. *Tribology International* 2003; **36**:189–197.
4. Wu SR, Oden JT. A note on applications of adaptive finite elements to elasto-hydrodynamic lubrication problems. *Communications in Applied Numerical Methods* 1987; **3**:485–494.
5. Johnson C, Hansbo P. Adaptive finite element methods in computational mechanics. *Computer Methods in Applied Mechanics and Engineering* 1992; **101**:143–181.
6. Johnson C. Adaptive finite element methods for the obstacle problem. *Mathematical Models and Methods in Applied Sciences* 1992; **2**:483–487.
7. Suttmeier F-T. General approach for *a posteriori* error estimates for finite element solutions of variational inequalities. *Computational Mechanics* 2001; **27**:317–323.
8. French DA, Larsson S, Nochetto RH. Pointwise *a posteriori* error analysis for an adaptive penalty finite element method for the obstacle problem. *Computational Methods in Applied Mathematics* 2001; **1**:18–38.
9. Capriz G, Cimatti G. Free boundary problems in the theory of hydrodynamic lubrication: a survey. In *Free Boundary Problems: Theory and Applications*, vol. II, Fasano A, Primicerio M (eds). Pitman: Boston, 1983; 613–635.
10. Scholz R. Numerical solution of the obstacle problem by the penalty method. *Computing* 1984; **32**:297–306.
11. Wu SR. A penalty formulation and numerical approximation of the Reynolds–Hertz problem of elasto-hydrodynamic lubrication. *International Journal of Engineering Science* 1984; **24**:1001–1013.
12. Clément P. Approximation by finite element functions using local regularization. *RAIRO Modélisation Mathématique et Analyse Numérique* 1975; **9 R-2**:77–84.
13. Becker R, Rannacher R. A feed-back approach to error control in finite element methods: basic analysis and examples. *East-West Journal of Numerical Mathematics* 1996; **4**:237–264.
14. Frêne J, Nicolas D, Degueurce B, Berthe D, Godet M. *Hydrodynamic Lubrication*. Elsevier: Amsterdam, 1997.

Paper II

A STOKES MODEL WITH CAVITATION FOR THE NUMERICAL SIMULATION OF HYDRODYNAMIC LUBRICATION

BERTIL NILSSON AND PETER HANSBO

ABSTRACT. We present a cavitation model based on Stokes' equation and formulate adaptive finite element methods for its numerical solution. *A posteriori* error estimates and adaptive algorithms are derived, and numerical examples illustrating the theory are supplied, in particular with comparison to the simplified Reynolds model of lubrication.

1. INTRODUCTION

The motivation for this work is the need for accurate computations of the hydrostatic pressure in a lubricant entrapped between the tool and workpiece in a metal forming process or in a sliding bearing. The ultimate goal is to be able to optimize the surface structure so as to maximize the lift from the pressure in the fluid. The usual tool for analyzing this problem is the Reynolds' model [15], which however has severe limitations in that it is not well suited for handling large variations in the geometry of the lubrication layer. One way of decreasing resistance between the tool and workpiece is to make pits in the surface of the workpiece in order to generate cavitation with resulting pressure redistribution. If the pit geometry cannot be allowed to vary in an arbitrary fashion, optimization of the pit geometry becomes untenable.

In this paper, we will present a model for Stokesian flow with cavitation and formulate adaptive finite element methods for its solution. We will focus on control of the error in energy-like norms, and present numerical results comparing the Stokes model with the Reynolds model.

2. THE CONTINUOUS PROBLEM

Consider a domain Ω in \mathbb{R}^n , $n = 2$ or $n = 3$ with boundary $\partial\Omega$. We consider a lubricant with viscosity μ . The Stokes equation can then be written

$$(1) \quad -2\mu\nabla \cdot \varepsilon(\mathbf{u}) + \nabla p = \mathbf{f} \text{ and } \nabla \cdot \mathbf{u} = 0 \quad \text{in } \Omega,$$

Key words and phrases. cavitation, Stokes problem, adaptivity, error estimate .

with, for ease of presentation, $\mathbf{u} = 0$ on $\partial\Omega$. Here, \mathbf{u} is the velocity of the lubricant,

$$\boldsymbol{\varepsilon}(\mathbf{u}) = \frac{1}{2} (\nabla \otimes \mathbf{u} + (\nabla \otimes \mathbf{u})^T)$$

is the symmetric velocity gradient, p is the pressure, and \mathbf{f} is a force term. We have also used the notation

$$(\nabla \cdot \boldsymbol{\tau})_i = \sum_{j=1}^n \frac{\partial \tau_{ij}}{\partial x_j}.$$

Cavitation occurs when the pressure reaches atmospheric pressure, which we for definiteness define as $p = 0$. The lubricant cannot support subatmospheric pressure, so an additional condition is $p \geq 0$ in Ω . In order to incorporate this condition into the model, it can be written as a variational inequality as follows. Let

$$K = \{p \in L_2(\Omega) : p \geq 0\},$$

and seek $\mathbf{u} \in [H^1(\Omega)]^n$ and $p \in K$ such that

$$(2) \quad \int_{\Omega} 2\mu \boldsymbol{\varepsilon}(\mathbf{u}) : \boldsymbol{\varepsilon}(\mathbf{v}) \, d\Omega - \int_{\Omega} p \nabla \cdot \mathbf{v} \, d\Omega = \int_{\Omega} \mathbf{f} \cdot \mathbf{v} \, d\Omega, \quad \forall \mathbf{v} \in [H^1(\Omega)]^n$$

and

$$(3) \quad - \int_{\Omega} \nabla \cdot \mathbf{u} (q - p) \, d\Omega \leq 0, \quad \forall q \in K.$$

The well-posedness of this problem follows from the general theory presented by Brezzi, Hager, and Raviart [6].

3. FINITE ELEMENT APPROXIMATION

3.1. Formulation. In order to discretize this problem, we let \mathcal{T}_h denote a triangulation of Ω into simplices T of diameter h_T , and let \mathcal{E}_h denote the set of element faces E , of size h_E , in \mathcal{T}_h . We split \mathcal{E}_h into two disjoint subsets

$$\mathcal{E}_h = \mathcal{E}_I \cup \mathcal{E}_B$$

where \mathcal{E}_I is the set of edges in the interior of Ω and \mathcal{E}_B is the set of edges on the boundary. Further, with each edge we associate a fixed unit normal \mathbf{n} such that for edges on the boundary \mathbf{n} is the exterior unit normal. We denote the jump of a function $\mathbf{v} \in \boldsymbol{\Gamma}_h$ at an edge E by $[[\mathbf{v}]] = \mathbf{v}^+ - \mathbf{v}^-$ for $E \in \mathcal{E}_I$ and $[[\mathbf{v}]] = \mathbf{v}^+$ for $E \in \mathcal{E}_B$, and the average $\langle \mathbf{v} \rangle = (\mathbf{v}^+ + \mathbf{v}^-)/2$ for $E \in \mathcal{E}_I$ and $\langle \mathbf{v} \rangle = \mathbf{v}^+$ for $E \in \mathcal{E}_B$, where $\mathbf{v}^{\pm} = \lim_{\epsilon \downarrow 0} \mathbf{v}(\mathbf{x} \mp \epsilon \mathbf{n})$ with $\mathbf{x} \in E$.

We define the following nonconforming finite element space:

$$V_h := \{ \mathbf{v} \in [L_2(\Omega)]^n : \mathbf{v} \in [P^1(T)]^n, \forall T \in \mathcal{T}_h, \mathbf{v} \text{ is continuous at the midpoints of all interior faces, and } \mathbf{v} = 0 \text{ at the midpoints of all faces along } \partial\Omega \}.$$

$$Q_h := \{q \in L_2(\Omega) : q|_T \in P^0(T), \forall T \in \mathcal{T}_h\},$$

i.e., we will use the Crouzeix-Raviart element which is known to be *inf-sup* stable. We seek $(\mathbf{u}_h, p_h) \in V_h \times Q_h$ such that

$$(4) \quad a_h(\mathbf{u}_h, \mathbf{v}) + b_h(\mathbf{v}, p_h) = (\mathbf{f}, \mathbf{v}), \quad \forall \mathbf{v} \in V_h$$

$$(5) \quad b_h(\mathbf{u}_h, q - p_h) \leq 0, \quad \forall q \in Q_h \cap K.$$

Here,

$$(6) \quad a_h(\mathbf{u}, \mathbf{v}) := \sum_{T \in \mathcal{T}_h} \int_T 2\mu \boldsymbol{\varepsilon}(\mathbf{u}) : \boldsymbol{\varepsilon}(\mathbf{v}) \, dx + \sum_{E \in \mathcal{E}_h} \frac{\gamma}{h_E} \int_E [[\mathbf{u}]] \cdot [[\mathbf{v}]] \, ds$$

and

$$(7) \quad b_h(\mathbf{v}, q) := - \sum_{T \in \mathcal{T}_h} \int_T \nabla \cdot \mathbf{v} \, q \, dx.$$

Here, h_E denotes the smallest of the sizes h_T of the elements sharing edge E . We remark that the standard formulation for the Crouzeix-Raviart element is not stable for the symmetric velocity gradient formulation of Stokes problem because of the absence of a discrete Korn's inequality. The jumps across element borders are added in order to fix this problem. We refer to [4, 10] for details.

3.2. Solution method. In order to solve the non-linear discrete system (4) and (5), we apply an iterative algorithm of Uzawa type.

- (1) Let $k = 0$ and choose an initial p_h^k .
- (2) Solve the linear system (4) for the velocity field \mathbf{u}_h^k .
- (3) Update the pressure field $p_h^{k+1} = P_\Lambda(p_h^k - \nabla \cdot \mathbf{u}_h^k)$ elementwise, where the operator $P_\Lambda(\vartheta) := \max(0, \vartheta)$.
- (4) Set $k = k + 1$ and go back to step (2).

3.3. A posteriori error control. The question of error control for mixed variational inequalities has not been extensively treated in the literature. Though it fits in the general framework of Becker and Rannacher [2], the only paper the authors are aware of that explicitly treats the case at hand is [17], where, however, the fact that there is a variational inequality not only for the multiplier, but also for the primal variable, is used in a crucial way. We shall here instead explore a simple alternative to [2, 17] based on the observation that the cavitation problem is reminiscent of the Hencky problem in elasto-plasticity, and then follow Johnson and Hansbo [13] in deriving a posteriori error estimates. We then first consider the compressible case and consider the Stokes problem as the limit of the corresponding elasticity problem with the bulk modulus tending to infinity. The elasticity problem in question can be formulated as follows: find the velocity \mathbf{u} and the stress $\boldsymbol{\sigma}$ such that

$$\begin{aligned}
(8) \quad \boldsymbol{\sigma} &= 2\mu \boldsymbol{\varepsilon}^D(\mathbf{u}) + \Pi(\kappa \nabla \cdot \mathbf{u}) \mathbf{1} \quad \text{in } \Omega \\
-\nabla \cdot \boldsymbol{\sigma} &= \mathbf{f} \quad \text{in } \Omega \\
\mathbf{u} &= 0 \quad \text{on } \partial\Omega
\end{aligned}$$

Here, κ is the bulk modulus, $\mathbf{1}$ is the identity tensor, $\boldsymbol{\tau}^D = \boldsymbol{\tau} - \frac{1}{3} \text{tr } \boldsymbol{\tau} \mathbf{1}$ is the deviatoric part of $\boldsymbol{\tau}$, with $\text{tr } \boldsymbol{\tau} = \sum_k \tau_{kk}$, and

$$(9) \quad \Pi(v) = \begin{cases} v & \text{if } v \leq 0, \\ 0 & \text{if } v > 0. \end{cases}$$

To simplify the analysis, we shall consider a regularized version of (8) in the form of a penalty method. Given $\epsilon > 0$, find $\boldsymbol{\sigma} \in W = \{\boldsymbol{\tau} : \tau_{ji} = \tau_{ij} \in L_2(\Omega)\}$ and $\mathbf{u} \in [H_0^1]^n$ such that

$$(10) \quad \begin{aligned} c(\boldsymbol{\sigma}, \boldsymbol{\tau}) + \epsilon^{-1}(\text{tr } \boldsymbol{\sigma} - \Pi(\text{tr } \boldsymbol{\sigma}), \boldsymbol{\tau}) - (\boldsymbol{\varepsilon}(\mathbf{u}), \boldsymbol{\tau}) &= 0, \quad \forall \boldsymbol{\tau} \in W \\ (\boldsymbol{\sigma}, \boldsymbol{\varepsilon}(\mathbf{u})) - (\mathbf{f}, \mathbf{v}) &= 0, \quad \forall \mathbf{v} \in [H_0^1]^n. \end{aligned}$$

Here

$$(\mathbf{f}, \mathbf{v}) = \int_{\Omega} \mathbf{f} \cdot \mathbf{v} \, dx, \quad (\boldsymbol{\sigma}, \boldsymbol{\tau}) = \int_{\Omega} \boldsymbol{\sigma} : \boldsymbol{\tau} \, dx,$$

and $c(\boldsymbol{\sigma}, \boldsymbol{\tau})$ is the *complementary energy* functional

$$(11) \quad c(\boldsymbol{\sigma}, \boldsymbol{\tau}) := \int_{\Omega} \left(\frac{1}{2\mu} \boldsymbol{\sigma}^D : \boldsymbol{\tau}^D + \frac{1}{3\kappa} \text{tr } \boldsymbol{\sigma} \text{tr } \boldsymbol{\tau} \right) d\Omega.$$

Note that (10) formally tends to (8) as $\epsilon \rightarrow 0$. The regularization is introduced with the purpose of simplifying the statement and proof of the *a posteriori* error estimate, and the actual (small) value of ϵ will be insignificant. In the following, we shall use the notation

$$\boldsymbol{\eta}(\boldsymbol{\sigma}) = \frac{1}{\epsilon} (\text{tr } \boldsymbol{\sigma} - \Pi(\text{tr } \boldsymbol{\sigma})) \mathbf{1}.$$

3.3.1. Finite element formulation. The regularized and slightly compressible form of (4)–(5) now takes the form: find $(\boldsymbol{\sigma}_h, \mathbf{u}_h) \in W \times V_h$ such that

$$(12) \quad c(\boldsymbol{\sigma}_h, \boldsymbol{\tau}) + (\boldsymbol{\eta}(\boldsymbol{\sigma}_h), \boldsymbol{\tau}) = (\boldsymbol{\varepsilon}(\mathbf{u}_h), \boldsymbol{\tau})$$

for all $\boldsymbol{\tau} \in W$,

$$(13) \quad \sum_{T \in \mathcal{T}_h} (\boldsymbol{\sigma}_h, \boldsymbol{\varepsilon}(\mathbf{v}))_T + \sum_{E \in \mathcal{E}_h} \frac{\gamma}{h_E} (\llbracket \mathbf{u}_h \rrbracket, \llbracket \mathbf{v} \rrbracket)_E = (\mathbf{f}, \mathbf{v})$$

for all $\mathbf{v} \in V_h$. Here, Equation (12) can be thought of as holding pointwise in the element; it is formulated as a weak statement for convenience only.

3.3.2. *An energy norm error estimate for the elasticity equations.* To prepare for the full error estimate, we first need to establish an error estimate for the elasticity equations without cavitation. A closely related estimate was recently derived for fully discontinuous finite element methods in [11]. We write the discretized elasticity equations as follows. Find $\mathbf{u}_h \in V_h$ such that

$$(14) \quad \sum_{T \in \mathcal{T}_h} (\boldsymbol{\sigma}(\mathbf{u}_h), \mathbf{v})_T + \sum_{E \in \mathcal{E}_h} \frac{\gamma}{h_E} (\llbracket \mathbf{u}_h \rrbracket, \llbracket \mathbf{v} \rrbracket)_E = (\mathbf{f}, \mathbf{v}), \quad \forall \mathbf{v} \in V_h,$$

where the elastic stress tensor is defined as

$$(15) \quad \boldsymbol{\sigma}(\mathbf{u}) = 2\mu \boldsymbol{\varepsilon}(\mathbf{u}) + (\kappa - 2\mu/3) \nabla \cdot \mathbf{u} \mathbf{1}.$$

We let \mathbf{u} denote the exact solution to the continuous problem corresponding to (14) and introduce the following norm

$$(16) \quad \|\mathbf{v}\|^2 = \sum_{T \in \mathcal{T}_h} (\boldsymbol{\sigma}(\mathbf{v}), \boldsymbol{\varepsilon}(\mathbf{v}))_T$$

on $H_0^1 \cup V_h$. For the three-dimensional case, we shall use the following decomposition of 3×3 tensor fields (for the two-dimensional case, we analogously use the decomposition introduced in [3]). Below we denote by $H(\text{curl}, \Omega)$ the space of vector-valued functions in $[L_2(\Omega)]^3$ for which the curl is also in $[L_2(\Omega)]^3$.

Lemma 1. *Let $\boldsymbol{\chi} \in L^2(\Omega, \mathbf{R}^{3 \times 3})$ be a second order tensor field. Then there exist $\mathbf{z} \in H_0^1(\Omega)$ and $\boldsymbol{\phi} \in [H(\text{curl}, \Omega)]^3$ such that*

$$(17) \quad \boldsymbol{\chi} = \boldsymbol{\sigma}(\mathbf{z}) + \mathbf{Curl} \boldsymbol{\phi}$$

where

$$(18) \quad \mathbf{Curl} \boldsymbol{\phi} = \begin{bmatrix} \frac{\partial \phi_{13}}{\partial x_2} - \frac{\partial \phi_{12}}{\partial x_3} & \frac{\partial \phi_{11}}{\partial x_3} - \frac{\partial \phi_{13}}{\partial x_1} & \frac{\partial \phi_{12}}{\partial x_1} - \frac{\partial \phi_{11}}{\partial x_2} \\ \frac{\partial \phi_{23}}{\partial x_2} - \frac{\partial \phi_{22}}{\partial x_3} & \frac{\partial \phi_{21}}{\partial x_3} - \frac{\partial \phi_{23}}{\partial x_1} & \frac{\partial \phi_{22}}{\partial x_1} - \frac{\partial \phi_{21}}{\partial x_2} \\ \frac{\partial \phi_{33}}{\partial x_2} - \frac{\partial \phi_{32}}{\partial x_3} & \frac{\partial \phi_{31}}{\partial x_3} - \frac{\partial \phi_{33}}{\partial x_1} & \frac{\partial \phi_{32}}{\partial x_1} - \frac{\partial \phi_{31}}{\partial x_2} \end{bmatrix}$$

and the following stability estimate holds

$$(19) \quad \|\mathbf{z}\|_{H^1(\Omega)} + \|\mathbf{Curl} \boldsymbol{\phi}\|_{L_2(\Omega)} \leq C \|\boldsymbol{\chi}\|_{L_2(\Omega)}.$$

Proof. We let \mathbf{z} solve the variational problem

$$(\boldsymbol{\sigma}(\mathbf{z}), \boldsymbol{\varepsilon}(\mathbf{v})) = (\boldsymbol{\chi}, \boldsymbol{\varepsilon}(\mathbf{v})) \quad \forall \mathbf{v} \in [H^1(\Omega)]^n,$$

and thus $\|\mathbf{z}\|_{H^1(\Omega)} \leq C \|\boldsymbol{\chi}\|_{L_2(\Omega)}$ by Korn's inequality. Further, $\nabla \cdot (\boldsymbol{\sigma}(\mathbf{z}) - \boldsymbol{\chi}) = 0$ in the distributional sense; thus the divergence of each row $[\boldsymbol{\sigma}(\mathbf{z}) - \boldsymbol{\chi}]_i$ of

the matrix $\boldsymbol{\sigma}(\mathbf{z}) - \boldsymbol{\chi}$ is zero and may be represented in terms of the curl of functions $\boldsymbol{\phi}_i = [\phi_{i1} \ \phi_{i2} \ \phi_{i3}] \in H(\text{curl}, \Omega)$. This implies that there exists a matrix $\boldsymbol{\phi} = [\boldsymbol{\phi}_1^T \ \boldsymbol{\phi}_2^T \ \boldsymbol{\phi}_3^T]^T \in [H(\text{curl}, \Omega)]^3$ such that

$$\boldsymbol{\chi} - \boldsymbol{\sigma}(\mathbf{z}) = \mathbf{Curl} \boldsymbol{\phi},$$

$$\|\mathbf{Curl} \boldsymbol{\phi}\|_{L_2(\Omega)} = \|\boldsymbol{\chi} - \boldsymbol{\sigma}(\mathbf{z})\|_{L_2(\Omega)} \leq C \|\boldsymbol{\chi}\|_{L_2(\Omega)}.$$

□

Note that if $\boldsymbol{\chi}$ is symmetric, $\mathbf{Curl} \boldsymbol{\phi}$ is also symmetric.

We are now ready to formulate our main result. In the following, C denotes a generic constant independent of the meshsize, not necessarily the same at different instances.

Theorem 1. *The following a posteriori error estimate holds*

$$(20) \quad \|\mathbf{u} - \mathbf{u}_h\|^2 \leq C \sum_{T \in \mathcal{T}_h} \eta_T^2$$

where the element indicator η_T is defined by

$$\begin{aligned} \eta_T^2 &= h_T^2 \|\mathbf{f} + \nabla \cdot \boldsymbol{\sigma}(\mathbf{u}_h)\|_{L_2(T)}^2 + \frac{\gamma^2}{h_T} \|\llbracket \mathbf{u}_h \rrbracket\|_{L_2(\partial T)}^2 \\ &\quad + h_T \|\llbracket \boldsymbol{\sigma}(\mathbf{u}_h) \cdot \mathbf{n} \rrbracket\|_{L_2(\partial T)}^2. \end{aligned}$$

Proof. Letting $\mathbf{e} = \mathbf{u} - \mathbf{u}_h$ be the error and using the decomposition (17) with $\boldsymbol{\chi} = \boldsymbol{\sigma}(\mathbf{e})$ and elementwise applied derivatives we obtain

$$\begin{aligned} \|\mathbf{e}\|^2 &= \sum_{T \in \mathcal{T}_h} (\boldsymbol{\sigma}(\mathbf{e}), \boldsymbol{\varepsilon}(\mathbf{e}))_T \\ &= \sum_{T \in \mathcal{T}_h} (\boldsymbol{\varepsilon}(\mathbf{e}), \boldsymbol{\sigma}(\mathbf{z}))_T + \sum_{T \in \mathcal{T}_h} (\boldsymbol{\varepsilon}(\mathbf{e}), \mathbf{Curl} \boldsymbol{\phi})_T \\ (21) \quad &= I + II \end{aligned}$$

We proceed with estimates of the two terms.

For the first term I we first eliminate the exact elasticity solution \mathbf{u} and use the definition of the finite element method (14) to subtract the continuous Scott-Zhang interpolant $\pi \mathbf{z} \in V_h$, cf. Brenner and Scott [5], as follows

$$\begin{aligned} I &= \sum_{T \in \mathcal{T}_h} (\boldsymbol{\sigma}(\mathbf{e}), \boldsymbol{\varepsilon}(\mathbf{z}))_T \\ &= (\mathbf{f}, \mathbf{z}) - \sum_{T \in \mathcal{T}_h} (\boldsymbol{\sigma}(\mathbf{u}_h), \boldsymbol{\varepsilon}(\mathbf{z}))_T \\ &= (\mathbf{f}, \mathbf{z} - \pi \mathbf{z}) - \sum_{T \in \mathcal{T}_h} (\boldsymbol{\sigma}(\mathbf{u}_h), \boldsymbol{\varepsilon}(\mathbf{z} - \pi \mathbf{z}))_T. \end{aligned}$$

Next, using Green's formula we arrive at

$$\begin{aligned} I &= \sum_{T \in \mathcal{T}_h} (\mathbf{f} + \nabla \cdot \boldsymbol{\sigma}(\mathbf{u}_h), \mathbf{z} - \pi \mathbf{z})_T \\ &\quad - \sum_{E \in \mathcal{E}_h} ([\mathbf{n} \cdot \boldsymbol{\sigma}(\mathbf{u}_h)]], \mathbf{z} - \pi \mathbf{z})_E \\ &= I_1 + I_2, \end{aligned}$$

where \mathbf{n} is fixed on each edge in accordance with the direction of the jump. These terms may now be directly estimated in a straightforward manner using the Cauchy-Schwartz inequality, the trace inequality

$$\|v\|_{L_2(\partial T)}^2 \leq C \left(h_T^{-1} \|v\|_{L_2(T)}^2 + h_T \|\nabla v\|_{L_2(T)}^2 \right),$$

cf. Thomée [18], standard interpolation error estimates, cf. [5], and finally the stability estimate (19) as follows.

Term I_1 . Using the Cauchy-Schwartz inequality on the sum and scaling with suitable powers of h_T we obtain

(22)

$$I_1 \leq \left(\sum_{T \in \mathcal{T}_h} h_T^2 \|\mathbf{f} + \nabla \cdot \boldsymbol{\sigma}(\mathbf{u}_h)\|_{L_2(T)}^2 \right)^{1/2} \left(\sum_{T \in \mathcal{T}_h} h_T^{-2} \|\mathbf{z} - \pi \mathbf{z}\|_{L_2(T)}^2 \right)^{1/2}$$

Next using interpolation error estimates we have

$$(23) \quad \sum_{T \in \mathcal{T}_h} h_T^{-2} \|\mathbf{z} - \pi \mathbf{z}\|_{L_2(T)}^2 \leq C \|\mathbf{z}\|_{H^1(\Omega)}^2$$

Term I_2 . Using the Cauchy-Schwartz inequality on the sum with suitable scaling we get

(24)

$$I_2 \leq \left(\sum_{E \in \mathcal{E}_h} h_T \|[\mathbf{n} \cdot \boldsymbol{\sigma}(\mathbf{u}_h)]]\|_{L_2(E)}^2 \right)^{1/2} \left(\sum_{E \in \mathcal{E}_h} h_T^{-1} \|\mathbf{z} - \pi \mathbf{z}\|_{L_2(E)}^2 \right)^{1/2}$$

Using the trace inequality followed by an interpolation error estimate we have

$$(25) \quad \sum_{E \in \mathcal{E}_h} h_T^{-1} \|\mathbf{z} - \pi \mathbf{z}\|_{L_2(E)}^2 \leq C \|\mathbf{z}\|_{H^1(\Omega)}^2.$$

Collecting the estimates and using the stability estimate (19) we finally get

$$(26) \quad I \leq C \left(\sum_{T \in \mathcal{T}_h} \eta_T^2 \right)^{1/2} \|\mathbf{z}\|_{H^1(\Omega)} \leq C \left(\sum_{T \in \mathcal{T}_h} \eta_T^2 \right)^{1/2} \|\mathbf{e}\|$$

To estimate the second term II we first use Green's formula and the symmetry of $\mathbf{Curl} \phi$ to conclude that

$$(27) \quad \begin{aligned} II &= \sum_{T \in \mathcal{T}_h} (\varepsilon(\mathbf{e}), \mathbf{Curl} \phi)_T \\ &= \sum_{E \in \mathcal{E}_h} ([\mathbf{u}_h], \mathbf{n} \cdot \mathbf{Curl} \phi)_E \end{aligned}$$

since $\nabla \cdot \mathbf{Curl} \phi = \mathbf{0}$. Next we note that we can write the right-hand side in the following form

$$(28) \quad \begin{aligned} II &= \sum_{E \in \mathcal{E}_h} ([\mathbf{u}_h], \mathbf{n} \cdot \mathbf{Curl} \phi)_E \\ &= \sum_{T \in \mathcal{T}_h} (\mathbf{u}_h - \mathbf{w}, \mathbf{n} \cdot \mathbf{Curl} \phi)_{\partial T} \end{aligned}$$

for any continuous function \mathbf{w} which is zero on the boundary $\partial\Omega$. We can now estimate the contributions from each triangle as follows

$$(29) \quad (\mathbf{u}_h - \mathbf{w}, \mathbf{n} \cdot \mathbf{Curl} \phi)_{\partial T} \leq \|\mathbf{u}_h - \mathbf{w}\|_{H^{\frac{1}{2}}(\partial T)} \|\mathbf{n} \cdot \mathbf{Curl} \phi\|_{H^{-\frac{1}{2}}(\partial T)}$$

Next using the normal trace inequality

$$(30) \quad \|\mathbf{n} \cdot \mathbf{v}\|_{H^{-\frac{1}{2}}(\partial T)} \leq C (\|\mathbf{v}\|_{L_2(T)} + h_T \|\nabla \cdot \mathbf{v}\|_{L_2(T)})$$

see Larson and Målqvist [14], applied to each row of $\mathbf{Curl} \phi$, we obtain the following inequality

$$(31) \quad \|\mathbf{n} \cdot \mathbf{Curl} \phi\|_{H^{-\frac{1}{2}}(\partial T)} \leq C \|\mathbf{Curl} \phi\|_{L_2(T)}$$

which together with (28) and (29) give

$$(32) \quad \begin{aligned} II &\leq C \left(\sum_{T \in \mathcal{T}_h} \|\mathbf{u}_h - \mathbf{w}\|_{H^{\frac{1}{2}}(\partial T)}^2 \right)^{1/2} \left(\sum_{T \in \mathcal{T}_h} \|\mathbf{Curl} \phi\|_{L_2(T)}^2 \right)^{1/2} \\ &\leq C \left(\sum_{T \in \mathcal{T}_h} \|\mathbf{u}_h - \mathbf{w}\|_{H^{\frac{1}{2}}(\partial T)}^2 \right)^{1/2} \|\mathbf{e}\| \end{aligned}$$

Finally, the following inequality, see [14] for a detailed proof, holds

$$(33) \quad \inf_{\mathbf{w} \in [C(\Omega)]^n} \sum_{T \in \mathcal{T}_h} \|\mathbf{u}_h - \mathbf{w}\|_{H^{\frac{1}{2}}(\partial T)}^2 \leq C \sum_{T \in \mathcal{T}_h} h_T^{-1} \|[\mathbf{u}_h]\|_{L_2(\partial T)}^2$$

and thus we obtain the estimate

$$(34) \quad II \leq C \left(\sum_{T \in \mathcal{T}_h} h_T^{-1} \| [\mathbf{u}_h] \|_{L_2(\partial T)}^2 \right)^{1/2} \| \mathbf{e} \|$$

Collecting the estimates of terms I and II , the theorem follows. \square

3.3.3. Error estimation in the complementary energy norm. Having established an *a posteriori* estimate for the linear elasticity problem, we now return to our regularized cavitation problem. To obtain an error estimate in complementary energy norm for the Hencky problem, we subtract the finite element problem from the continuous problem to obtain

$$c(\boldsymbol{\sigma} - \boldsymbol{\sigma}_h, \boldsymbol{\tau}) + (\boldsymbol{\eta}(\boldsymbol{\sigma}) - \boldsymbol{\eta}(\boldsymbol{\sigma}_h), \boldsymbol{\tau}) = (\boldsymbol{\varepsilon}(\mathbf{u}) - \boldsymbol{\varepsilon}(\mathbf{u}_h), \boldsymbol{\tau}) \quad \forall \boldsymbol{\tau} \in W.$$

We define $\| \boldsymbol{\sigma} \|_c^2 := c(\boldsymbol{\sigma}, \boldsymbol{\sigma})$ and $\mathbf{e}_u := \mathbf{u} - \mathbf{u}_h$, and set $\boldsymbol{\tau} = \boldsymbol{\sigma} - \boldsymbol{\sigma}_h$ to find that

$$\begin{aligned} \| \boldsymbol{\sigma} - \boldsymbol{\sigma}_h \|_c^2 &= (\boldsymbol{\varepsilon}(\mathbf{u} - \mathbf{u}_h), \boldsymbol{\sigma} - \boldsymbol{\sigma}_h) - (\boldsymbol{\eta}(\boldsymbol{\sigma}) - \boldsymbol{\eta}(\boldsymbol{\sigma}_h), \boldsymbol{\sigma} - \boldsymbol{\sigma}_h) \\ &\leq (\boldsymbol{\varepsilon}(\mathbf{e}_u), \boldsymbol{\sigma} - \boldsymbol{\sigma}_h), \end{aligned}$$

where the last step follows from the following easily checked monotonicity relation:

$$(v - \Pi(v) - (w - \Pi(w)))(v - w) \geq 0.$$

Replacing $\boldsymbol{\sigma}(\mathbf{u}_h)$ by $\boldsymbol{\sigma}_h$ in Theorem 1 and the proof thereof, we conclude that

$$(35) \quad \| \boldsymbol{\sigma} - \boldsymbol{\sigma}_h \|_c^2 \leq C \sum_{T \in \mathcal{T}_h} \eta_T^2.$$

Finally, in a standard mixed method for slightly compressible elasticity, one replaces the divergence free condition corresponding to (5) with

$$(36) \quad - \sum_{T \in \mathcal{T}_h} \int_T \nabla \cdot \mathbf{u}^h q \, dx - \sum_{T \in \mathcal{T}_h} \int_T \frac{1}{\kappa} p^h q \, dx = 0,$$

for all $q \in Q_h$. Now, since the Crouzeix–Raviart approximation has the property $\nabla \cdot V_h \subset Q_h$ element-wise, we may simply identify

$$p^h = -\kappa \nabla \cdot \mathbf{u}^h,$$

which is typically not possible in other discrete mixed methods. Thus we can formally let $\kappa \rightarrow \infty$ and set $\boldsymbol{\sigma}_h = 2\mu \boldsymbol{\varepsilon}^D(\mathbf{u}_h) - p_h \mathbf{1}$ elementwise. This stress is then used to drive the adaptive scheme.

For deciding which elements to refine in the adaptive process, the size of the η_T is used as an indicator. We refine the 30% of the elements with the highest indicator in each adaptive step.

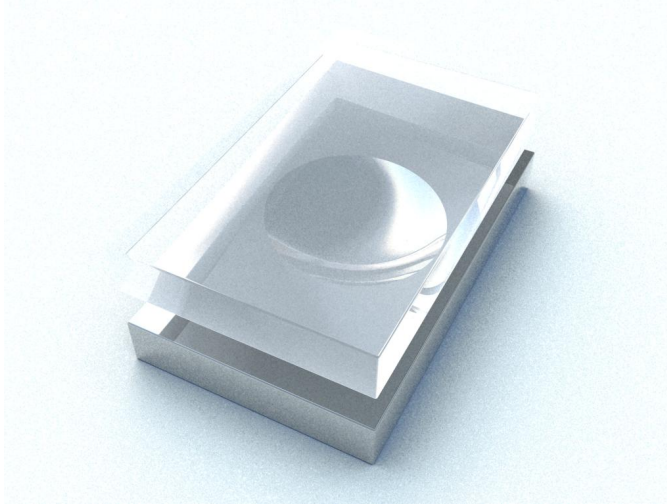


FIGURE 1. Oil pocket model.

4. NUMERICAL EXAMPLES

In order to investigate the performance of the methods proposed, a few numerical examples will be presented. Unfortunately, experimental results demonstrating in detail the local behavior of the pressure and velocity images is, to our knowledge, not published. Though some integrated experimental results, such as lift, has been given by Etsion [7], [8] and Wang et. al. [19].

The object for our study is a single parabolic shaped oil pocket, Figure 1. A central longitudinal cut through the gap between the metal sheet and work piece comprise our 2D computational model. The dimensions of the nominal channel and a particular pocket can be seen in Figure 2. Our aim is to study the behavior of the physics as the depth of the oil pocket increases while the opening width of the pocket and channel height stays the same. Boundary conditions used for the pressure is $p = 0$ at inlet and outlet. Velocity is set to zero along the floor of the channel and pocket boundary. Finally is the show driven by $u_x = 1, u_y = 0$ at the ceiling. The lubricant viscosity $\mu = 1$.

The initial mesh has a typical element side length of 0.1. In Figure 2 we visualize the adaptivity refinement progress inserting new nodes giving a sequence of meshes under consideration for a particular pocket depth. In each step the elements that give the largest third of the element contributions to the total error according to relation (35) are subdivided along their longest side into two new ones. After refinement step 10 is the area ratio approximately 80 for the largest element over the smallest. Likewise is the

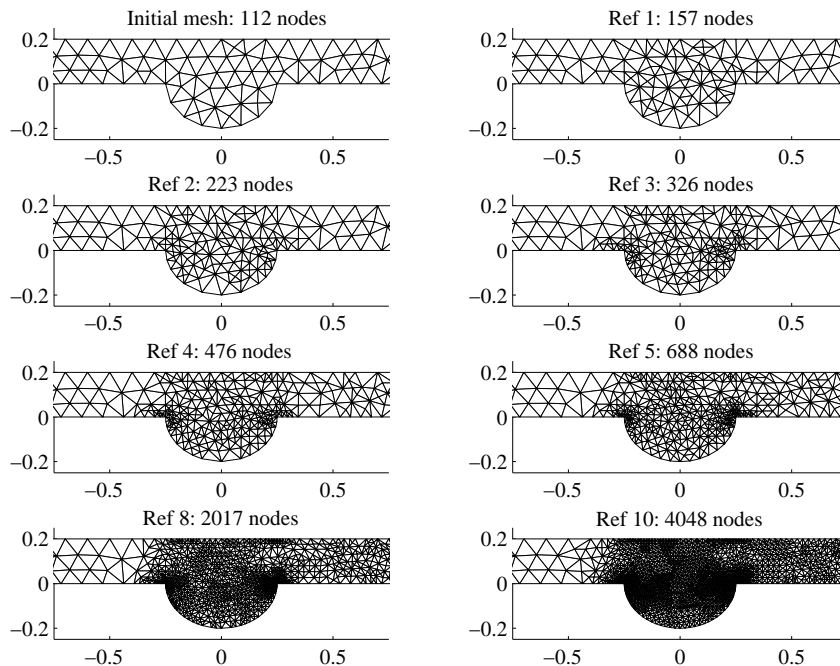


FIGURE 2. Sequence of refined meshes.

longest element side over the shortest one found to be about 20. The process indicates a sound adaptivity to take place at the two sharp corners of the oil pocket, which of course are the two dramatic regions of the domain.

The decrease of the total error according to refinement, measured by the number of nodes, is presented in Figure 3. Each dot indicates an adaptivity step.

From a starting pressure $p = 0$ throughout the initial domain is the pressure field inherited to the next refined mesh using linear interpolation during the adaptivity process. Despite this, is the typical number of iterations 500, though decreasing with refinement level, for the Usawa algorithm using well tuned relaxation, to converge according to $\|p_h^{k+1} - p_h^k\| < 10^{-9}$ for a particular mesh. All integrals involved are integrated using a 4-point Gauss quadrature scheme.

In Figure 4 we present row-wise for increased pocket depth, pressure, u_y , and stream function contour lines. We can see from the stream lines that we have recirculation in the pocket for a pocket depth somewhere between row two and three. In the left column is the cavitation zone identified to be located at the sharp upstream edge of the pocket. The important note

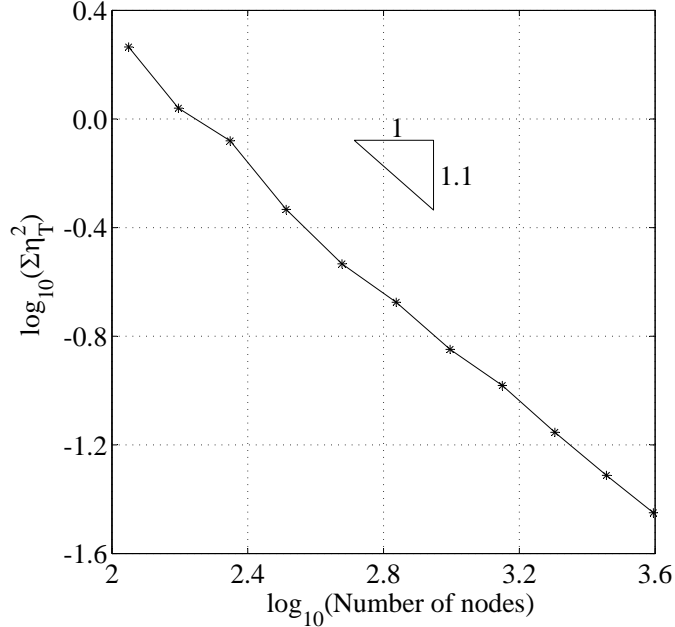


FIGURE 3. Convergence for the right hand side of the error estimate (35).

is of course that we do not need to *a priori* define the boundary location between the fluid and cavitation phases. This is automatically taken care of by the refinement process.

A comparison of pressure at ceiling between an adaptive Reynolds cavitation model [15] and the present Stokes cavitation model is given in Figure 5. The former tends to overestimate the pressure and also presents a sharper peak value, at least for moderate oil-pocket depths, while the Stokes model shows a more smooth realistic outfit. The classical way to approach the cavitation problem in the Reynolds community via continuity boundary conditions or first computing p^R from a pure Reynolds solution, followed by approximating $p \approx \max(0, p^R)$ (known as the half-Sommerfeld condition), is not very accurate at all compared to the cavitation models. The unrealistic peak in pressure at inlet is related to the fact that the symmetric velocity gradient formulation, not the Laplacian, is used for Stokes, resulting in unrealistic boundary effects (i.e., unrealistic for the present case, where the channel is cut off). However, this is of less practical importance as long as the inlet is placed considerable far away from the scene of interest in the

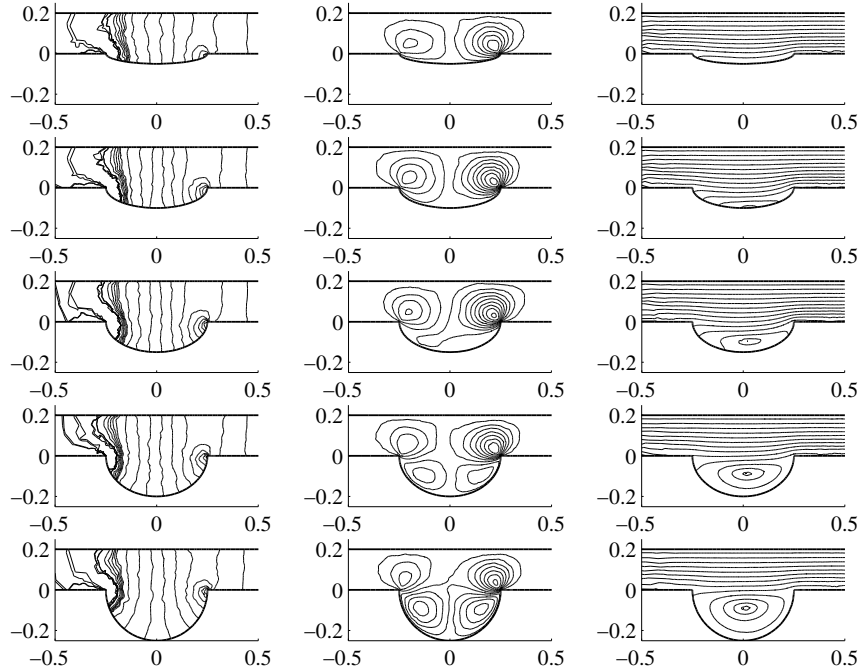


FIGURE 4. Pressure, u_y and stream function contour lines for increasing depth of the oil pocket.

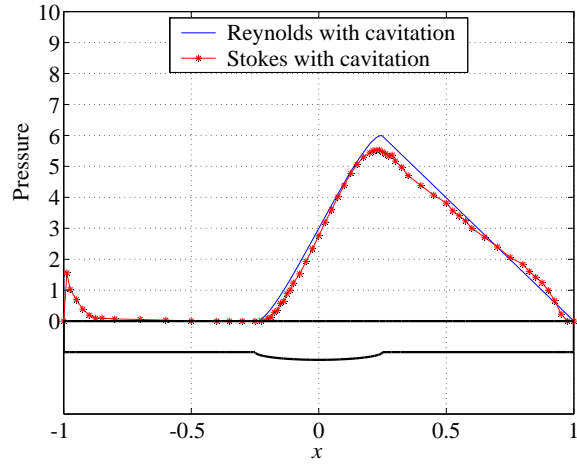
model. The pressure adapts rather fast to the correct one according to the formulation.

If we define impact to be the ratio of maximal channel height over minimal channel height Figure 6 indicates that both models are potent to indicate an oil pocket impact of ≈ 1.7 that is better than all other in order to produce best lift. This is in agreement with our earlier observation in Figure 4 indicating depth when recirculation is induced. A bouquet of figures 7-10 presents the mesh after 10 refinements and state of the flow for this particular pocket.

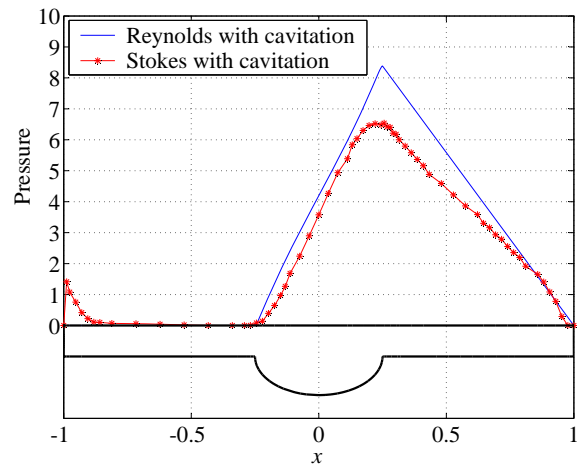
As the oil pocket depth increases the Reynolds model breaks down as can be seen in Figures 11-12. This is of course due to severe recirculation in the pocket, which interferes badly with one of the basic assumptions for the flow to be laminar in Reynolds model. However the Stokes model remains calm.

REFERENCES

- [1] G. Bayada, M. Chambat, The transition between the Stokes equation and the Reynolds equation: a mathematical proof, *Appl. Math. Optim.* 14 (1986) 73–93.



(a) Shallow pocket.



(b) Deeper pocket.

FIGURE 5. Pressure at ceiling for Reynolds and Stokes cavitation models for a shallow pocket and a rather deep one.

- [2] R. Becker, R. Rannacher, An optimal control approach to a posteriori error estimation in finite element methods, *Acta Numer.* 10 (2001) 1–102.
- [3] L. Beirão da Veiga, J. Niiranen, and R. Stenberg. A posteriori error estimates for the Morley plate bending element. *Numer. Math.*, 106(2):165–179, 2007.
- [4] S.C. Brenner, Korn’s inequalities for piecewise H^1 vector fields, *Mathematics of Computation* 2004; **73**(247):1067–1087.
- [5] S.C. Brenner, R.L Scott, *The Mathematical Theory of Finite Element Methods*, Springer, New York, 1994.

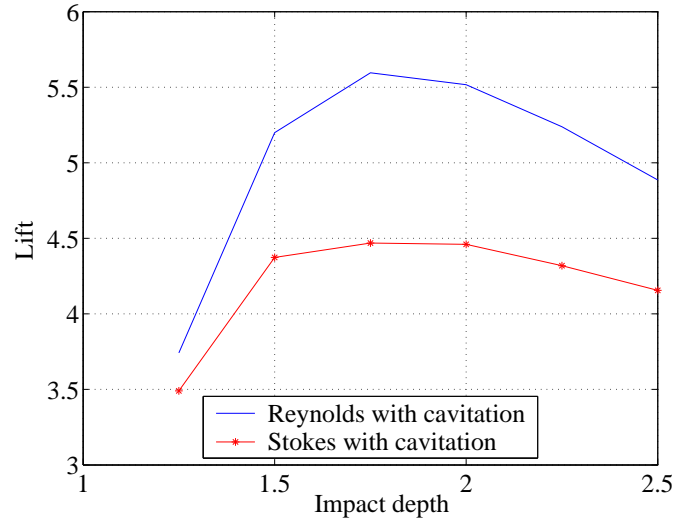


FIGURE 6. Lift for Stokes and Reynolds according to impact of the oil pocket.

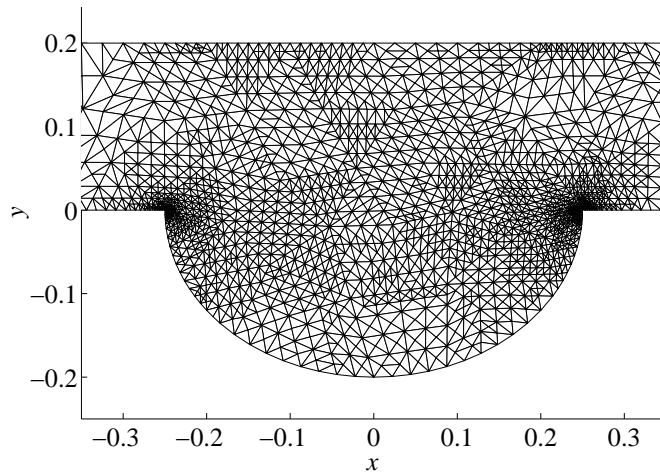


FIGURE 7. Element mesh.

- [6] F. Brezzi, W.W. Hager, P.-A. Raviart, Error estimates for the finite element solution of variational inequalities. Part II. Mixed methods, *Numer. Math.* 31 (1978) 1–16.
- [7] I. Etsion, L. Burstein, A model for mechanical seals with regular microsurface structure. *Tribology Transactions* 39 (1996) 677–683.

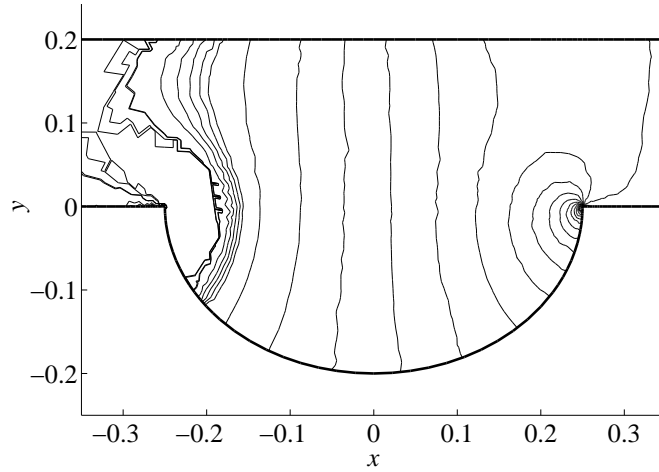
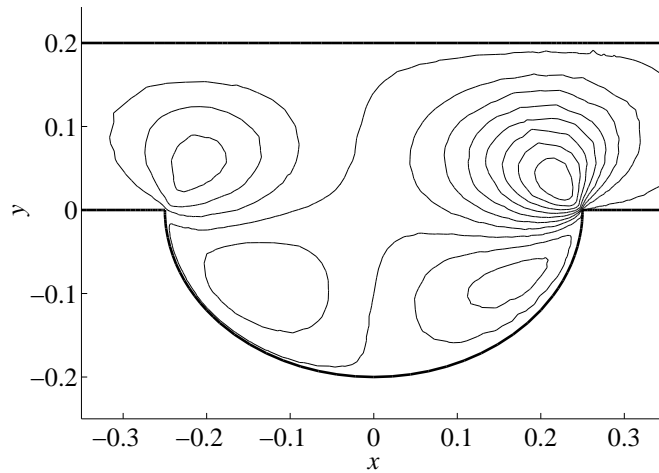


FIGURE 8. Pressure contour lines.

FIGURE 9. Velocity u_y contour lines.

- [8] I. Etsion, Y. Kligerman, G. Halperin, Analytical and Experimental Investigation of Laser-Textured Mechanical Seal Faces, *Tribology Transactions* 42 (1999) 511–516.
- [9] P. Hansbo, Three lectures on error estimation and adaptivity, in: E. Stein (Ed.), *Adaptive Finite Elements in Linear and Nonlinear Solid and Structural Mechanics*, CISM Courses and Lectures No. 416, Springer, (2005) 149–193.
- [10] P. Hansbo P, M.G. Larson, Discontinuous Galerkin and the Crouzeix-Raviart element: Application to elasticity, *ESAIM: Mathematical Modelling and Numerical Analysis* 2003; **37**(1):63–72.

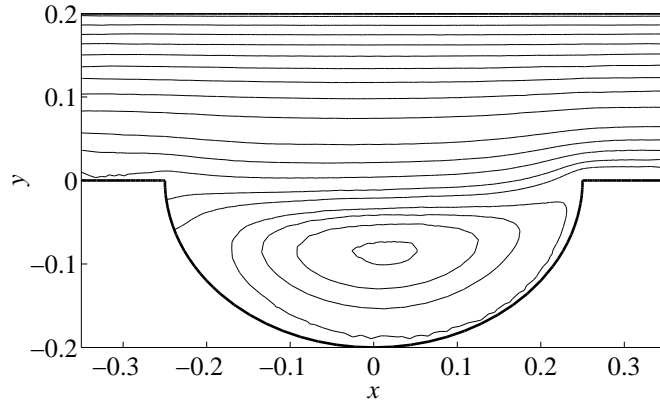


FIGURE 10. Stream function contour lines.

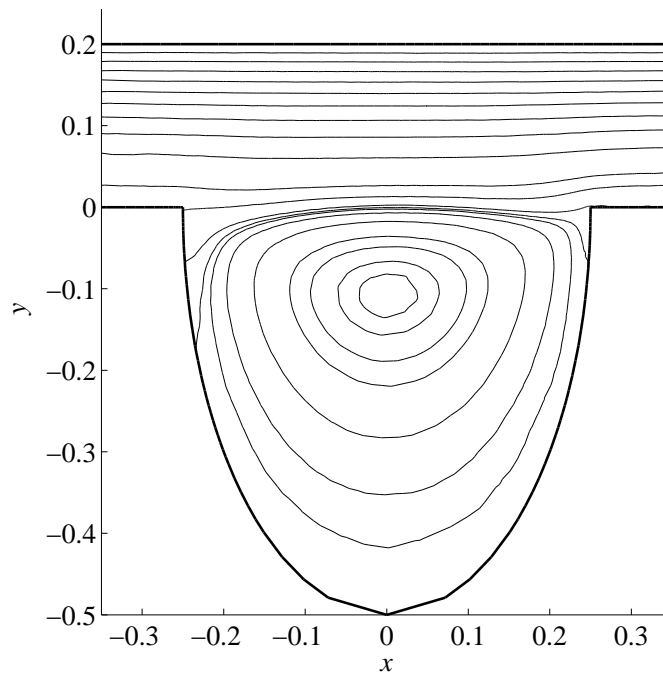


FIGURE 11. Stream function contour lines for a very deep pocket.

- [11] P. Hansbo P, M.G. Larson, Energy Norm A Posteriori Error Estimates for Discontinuous Galerkin Approximations of the Linear Elasticity Problem Preprint, Department of Mathematical Sciences, Chalmers University of Technology, 2009.

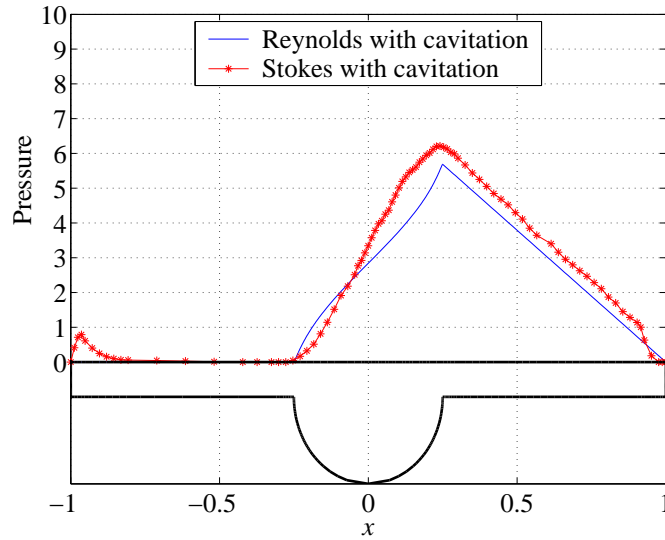


FIGURE 12. Pressure at ceiling for Reynolds and Stokes for a very deep pocket.

- [12] J. Haslinger, Mixed formulations of elliptic variational inequalities and its approximation, *Apl. Mat.* 26 (1981) 462–475.
- [13] C. Johnson, P. Hansbo, Adaptive finite element methods in computational mechanics, *Comput. Methods Appl. Mech. Engrg.* 101 (1992) 143–181.
- [14] M. G. Larson and A. Målqvist. A posteriori error estimates for mixed finite element approximations of elliptic problems. *Numer. Math.*, 108(3):487–500, 2008.
- [15] B. Nilsson, P. Hansbo, Adaptive finite element methods for hydrodynamic lubrication with cavitation, *Int. J. Numer. Methods Engrg.* 72 (2007) 1584–1604.
- [16] L. Slimane, A. Bendali, P. Laborde, Mixed formulations for a class of variational inequalities, *ESAIM: Math. Model. Numer. Anal.* 38 (2004) 177–201.
- [17] F.-T. Suttmeier, On computational methods for variational inequalities, *Comput. Mech.* 35 (2005) 401–408.
- [18] V. Thomée. *Galerkin Finite Element Methods for Parabolic Problems*. Springer-Verlag, Berlin, 1997.
- [19] X. Wang, K. Kato, A. Adachi, K. Aizawa, Load carrying capacity map for the surface texture design of SiC thrust bearing sliding in water, *Tribology International* 36 (2003) 189–197.

CENTER FOR APPLIED MATHEMATICS AND PHYSICS, HALMSTAD UNIVERSITY, SE-301 18 HALMSTAD, SWEDEN

DEPARTMENT OF MATHEMATICAL SCIENCES, CHALMERS UNIVERSITY OF TECHNOLOGY AND UNIVERSITY OF GOTHENBURG, SE-412 96 GÖTEBORG, SWEDEN

Paper III

A mixed finite element formulation of Reynolds equations with cavitation

Bertil Nilsson

*Center for Applied Mathematics and Physics, Halmstad University,
SE-301 18 Halmstad, Sweden*

Abstract

We present a cavitation model based on Reynolds equation and formulate a mixed finite element method for its numerical solution. A posteriori error estimates and adaptive algorithms are derived, and numerical examples illustrating the theory are supplied, in particular with comparison to the simplified Reynolds model of lubrication.

1 Introduction

The motivation for this work is the need for accurate computations of the hydrostatic pressure in a lubricant entrapped between the tool and workpiece in a metal forming process or in a sliding bearing. The ultimate goal is to be able to optimize the surface structure so as to minimize friction effects. The usual tool for analyzing this problem is the Reynolds model, which however has severe limitations in that it is not well suited for handling large variations in the geometry of the lubrication layer. One way of decreasing resistance between the tool and workpiece is to make pits in the surface of the workpiece in order to generate cavitation with resulting pressure redistribution. If the pit geometry cannot be allowed to vary in an arbitrary fashion, optimization of the pit geometry becomes untenable.

In this paper, we will present a mixed finite element model for Reynolds flow with cavitation and formulate adaptive finite element methods for its solution. We will focus on control of the error in energy-like norms, and present numerical results comparing the with the Reynolds model.

1.1 Reynolds equation

The first mathematical approach to tribology was undertaken by Leonard Euler with a geometrical resistance theory of "dry" friction - the *Interlocking Asperity Theory*. Euler's theory provides us with the two well known terms

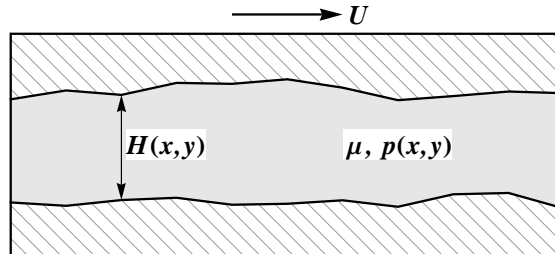


Figure 1: Reynolds channel.

for static and dynamic friction. The static friction coefficient is provided by the tangent of the asperity angle, while the dynamic friction coefficient is reduced by the kinetic term. But the true workhorse for many of years is of course the Reynolds equation. It has been used successfully to determine the pressure distribution in the fluid film for a wide range of applications from bearings, seals to sheet metal forming processes.

In the spirit of Figure 1, where a typical channel is furnished with the x -axis oriented as the relative surface velocity U and z -axis upwards, he made the following assumptions:

1. Body forces are neglected, i.e. there are no extra fields of forces acting on the fluid.
2. The pressure is constant through the thickness of the film.
3. The curvature of surfaces is large compared with film thickness. Surface velocities need not be considered as varying in direction.
4. There is no slip at the boundaries.
5. The lubricant is Newtonian, i.e. stress is proportional to rate of shear.
6. The flow is laminar.
7. Fluid inertia is neglected.
8. The viscosity is constant through the film thickness.

With these assumptions considered, the development of the equations can start. First, continuity of flow is examined.

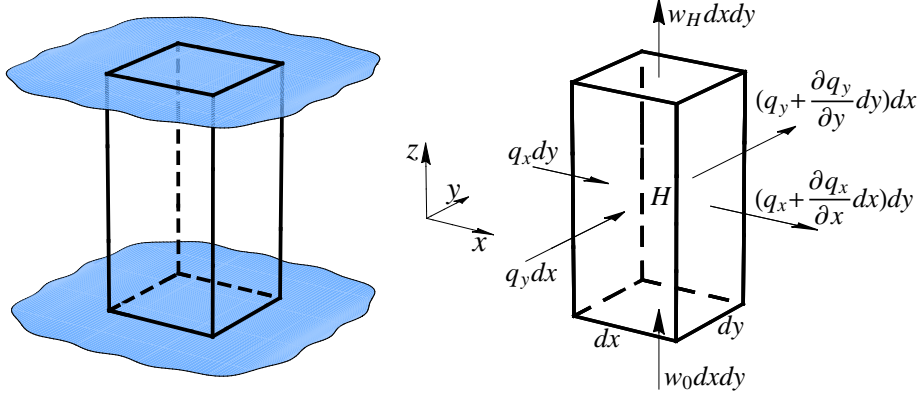


Figure 2: Continuity of flow in a column of height H .

1.1.1 Continuity of flow of a column

Consider a thin column of fluid of height $H(x, y)$ and base dx, dy , Figure 2. Fluid flows from the left at a rate q_x per unit width so the volume flow rate is $q_x dy$ into the column. The rate of flow out per unit width is

$$q_x + \frac{\partial q_x}{\partial x} dx, \quad (1)$$

where $\frac{\partial q_x}{\partial x}$ is the rate of change of flow in the x -direction. The actual flow out is

$$\left(q_x + \frac{\partial q_x}{\partial x} dx \right) dy. \quad (2)$$

In the y -direction the same argument applies. The flow rate in is $q_y dx$ and out is

$$\left(q_y + \frac{\partial q_y}{\partial y} dy \right) dx. \quad (3)$$

The vertical flow is rather different. If the floor of the column moves upwards at a velocity w_0 and if the roof moves upward as well at a speed w_H the volume of the column changes at a rate $(w_H - w_0) dx dy$. Although the base and roof are moving, at the instant considered the height is H , though a fraction of time later it will of course have altered.

An alternative possibility is that the floor and/or roof are porous, and fluid is flowing in at a velocity w_0 or out of the column at a velocity w_H . The fluid velocity can be considered constant over the very small base area $dx dy$ hence the increase of volume is at a rate $w_0 dx dy$ and fluid leaves at a rate $w_H dx dy$.

For continuity of flow, the fluid being of constant density, the rate flowing in must equal the rate flowing out. These can all be added up. Flowing into

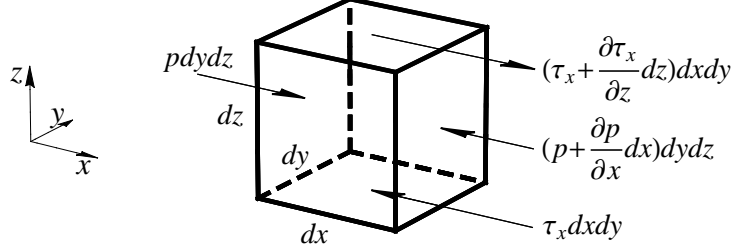


Figure 3: Equilibrium of an element.

the column

$$q_x dy + q_y dx + w_0 dx dy, \quad (4)$$

and flowing out

$$\left(q_x + \frac{\partial q_x}{\partial x} dx \right) dy + \left(q_y + \frac{\partial q_y}{\partial y} dy \right) dx + w_H dx dy. \quad (5)$$

These two are equal, equating them and canceling,

$$\frac{\partial q_x}{\partial x} dx dy + \frac{\partial q_y}{\partial y} dy dx + (w_H - w_0) dx dy = 0. \quad (6)$$

Now $dx dy$ is arbitrary and non zero, hence can be canceled giving the continuity of flow of a column as

$$\frac{\partial q_x}{\partial x} + \frac{\partial q_y}{\partial y} + (w_H - w_0) = 0. \quad (7)$$

If the top and bottom surfaces are impermeable, $w_H - w_0$ is the rate of change of height of the column according to time and may be written $\frac{\partial H}{\partial t}$. Having obtained the continuity it is necessary to look at the force balance of an element of the fluid.

1.1.2 Equilibrium of an element

Take a small element of fluid of sides dx , dy and dz , Figure 3, and consider first the forces in the x -direction only. On the left of the element there is a pressure p on the face of area $dydz$ giving a force of $p dy dz$ acting to the right. On the opposite face the pressure is

$$p + \frac{\partial p}{\partial x} dx, \quad (8)$$

and the corresponding force is

$$\left(p + \frac{\partial p}{\partial x} dx \right) dy dz. \quad (9)$$

There are shear stresses on the top and bottom faces producing forces. On the bottom face the shear stress τ_x gives a force $\tau_x dx dy$ acting to the left and on the top face, and acting to the right, is a force

$$\left(\tau_x + \frac{\partial \tau_x}{\partial z} dz \right) dx dy, \quad (10)$$

where the shear stress on the top face being $\tau_x + \frac{\partial \tau_x}{\partial z} dz$. These forces acting to the left and right must balance each other so

$$p dy dz + \left(\tau_x + \frac{\partial \tau_x}{\partial z} dz \right) dx dy = \left(p + \frac{\partial p}{\partial x} dx \right) dy dz + \tau_x dx dy, \quad (11)$$

expanding and canceling considering $dx dy dz$ an arbitrary non zero volume gives

$$\frac{\partial \tau_x}{\partial z} = \frac{\partial p}{\partial x}. \quad (12)$$

Now Newton's viscosity relation states

$$\tau_x = \mu \frac{\partial u}{\partial z}, \quad (13)$$

where u is the velocity of the fluid in the x -direction, so

$$\frac{\partial}{\partial z} \left(\mu \frac{\partial u}{\partial z} \right) = \frac{\partial p}{\partial x}. \quad (14)$$

In the y -direction where the velocity of the fluid is v the shear stresses and pressures can be equated and a similar equation follows

$$\frac{\partial \tau_y}{\partial z} = \frac{\partial p}{\partial y}, \quad \text{where} \quad \tau_y = \mu \frac{\partial v}{\partial z},$$

so

$$\frac{\partial}{\partial z} \left(\mu \frac{\partial v}{\partial z} \right) = \frac{\partial p}{\partial y}. \quad (15)$$

The pressure gradient in the z -direction is by assumption zero, so $\frac{\partial p}{\partial z} = 0$. Consider now equation (14) further. This can be integrated since p is not a function of z , thus

$$\mu \frac{\partial u}{\partial z} = \frac{\partial p}{\partial x} z + C_1. \quad (16)$$

Now both μ and u are functions of z but it is in this context too difficult to consider both at once so μ is taken as constant with respect to z as stated in assumption 8. It is important to realize that this is a big assumption and is only made for simplicity. The inclusion of $\frac{\partial \mu}{\partial z}$ can modify the equation very

considerably in certain circumstances. However, using this assumption, a further integration can be performed to give

$$\mu u = \frac{\partial p}{\partial x} \frac{z^2}{2} + C_1 z + C_2. \quad (17)$$

The boundary conditions are simple, according to assumption 4, i.e. no slip at the boundaries

$$\begin{cases} u(0) = U_0 \\ u(H) = U_H \end{cases}, \quad (18)$$

so (17) and (18) gives

$$u = \frac{1}{2\mu} \frac{\partial p}{\partial x} (z^2 - zH) + (U_H - U_0) \frac{z}{H} + U_0. \quad (19)$$

Finally the flow rate $q_x = \int_0^H u dz$ in the x -direction per unit width of y

$$q_x = -\frac{H^3}{12\mu} \frac{\partial p}{\partial x} + (U_0 + U_H) \frac{H}{2}. \quad (20)$$

If the same procedure is followed for y using equation (15) it is easily found that

$$q_y = -\frac{H^3}{12\mu} \frac{\partial p}{\partial y} + (V_0 + V_H) \frac{H}{2}, \quad (21)$$

where V_0 and V_H in the y -direction correspond to U_0 and U_H in the x -direction.

1.1.3 Full Reynolds equation

It is now possible to replace (20) and (21) into the continuity equation (7)

$$\frac{\partial}{\partial x} \left(\frac{H^3}{\mu} \frac{\partial p}{\partial x} \right) + \frac{\partial}{\partial y} \left(\frac{H^3}{\mu} \frac{\partial p}{\partial y} \right) = 6 \left(\frac{\partial}{\partial x} ((U_0 + U_H) H) + \frac{\partial}{\partial y} ((V_0 + V_H) H) + 2(w_H - w_0) \right). \quad (22)$$

This is the full Reynolds equation with everything varying.

1.1.4 Simplifications

Firstly, write U for the sum $U_0 + U_H$ and V for $V_0 + V_H$. These are merely short forms and do not involve any assumptions. Next, it is usually possible to arrange the axes so that either

$$\frac{\partial}{\partial x} (UH) = 0, \quad \text{or} \quad \frac{\partial}{\partial y} (VH) = 0.$$

The right hand side of (22) can therefore now be reduced to

$$6 \left(\frac{\partial}{\partial x}(UH) + 2(w_H - w_0) \right).$$

A further simplification is to realize that the velocity of a surface does not vary from one point to another, i.e. U is not a function of x so

$$\frac{\partial}{\partial x}(UH) = U \frac{\partial H}{\partial x}.$$

Furthermore, write $w_H - w_0$ as $\frac{\partial H}{\partial t}$; this is allowable if the surfaces are impermeable so no fluid seeps in or out and they are merely moving relative to each other. The right hand side of (22) now becomes

$$6 \left(U \frac{\partial H}{\partial x} + 2 \frac{\partial H}{\partial t} \right).$$

Keeping both these terms in is a matter of complexity. In steadily running situations, of course, $\frac{\partial H}{\partial t}$ is zero, so this term is usually omitted. Finally μ has been taken as constant in the z -direction, so why not consider it constant everywhere, giving

$$\frac{\partial}{\partial x} \left(H^3 \frac{\partial p}{\partial x} \right) + \frac{\partial}{\partial y} \left(H^3 \frac{\partial p}{\partial y} \right) = 6\mu U \frac{\partial H}{\partial x}, \quad (23)$$

or

$$\nabla \cdot (H^3 \nabla p) = 6\mu U \frac{\partial H}{\partial x}. \quad (24)$$

This is the Reynolds equation as usually quoted.

2 The continuous problem

By adding (20) and (21) taking continuity (7) and presented simplifications into consideration, we are able to reintroduce Reynolds equation and pose the problem as a mixed one of finding (\mathbf{q}, p) such that

$$\begin{aligned} \frac{12\mu}{H^3} \mathbf{q} + \nabla p &= \frac{6\mu}{H^2} \mathbf{U}, \\ \nabla \cdot \mathbf{q} &= 0, \end{aligned} \quad (25)$$

where it has been assumed that the thickness of the film does not change over time and that $\mathbf{U} = (U_0, U_H) = (0, U_H)$ and $\mathbf{V} = \mathbf{0}$. In weak form, this problem may be written as seeking $\mathbf{q} \in H(\text{div}; \Omega)$, where

$$H(\text{div}; \Omega) = \{ \mathbf{v} \in L_2(\Omega) : \|\nabla \cdot \mathbf{v}\|_{L_2(\Omega)} < \infty \},$$

and $p \in L_2(\Omega)$ such that

$$\int_{\Omega} \frac{12\mu}{H^3} \mathbf{q} \cdot \mathbf{v} \, d\Omega - \int_{\Omega} p \nabla \cdot \mathbf{v} \, d\Omega = \int_{\Omega} \frac{6\mu}{H^2} \mathbf{U} \cdot \mathbf{v} \, d\Omega, \quad \forall \mathbf{v} \in H(\text{div}; \Omega), \quad (26)$$

and

$$\int_{\Omega} \nabla \cdot \mathbf{q} w \, d\Omega = 0, \quad \forall w \in L_2(\Omega). \quad (27)$$

Boundary conditions for this problem are either handled strongly, in the case of conditions on the normal flow rate, or weakly in the case of conditions on the pressure.

3 The finite element method

3.1 Formulation

Let $\mathcal{T}_h = \{T\}$ be a locally quasi-uniform triangulation of Ω into simplexes T of local mesh size h . From the finite element theory of mixed methods, it is well known that one must carefully select the combination of approximations for the flow variables and the pressure variable. In case of the Reynolds model, a well known stable element combination is the lowest order Raviart-Thomas finite element spaces for the flux, i.e. $\mathbf{q}_h \in \mathcal{RT}_0$, defined as [5]

$$\mathcal{RT}_0 := \{\mathbf{q} \in H(\text{div}; \Omega) : \mathbf{q}|_T \in ([P_0(T)]^2 + \mathbf{x}P_0(T)), \forall T \in \mathcal{T}_h\},$$

where $P_0(T)$ is the space of zero degree polynomials on the element T , combined with element-wise constant pressure $p_h \in Q_h$, where

$$Q_h := \{w \in L_2(\Omega) : w|_T \in P_0(T), \forall T \in \mathcal{T}_h\}.$$

The Raviart-Thomas (\mathcal{RT}_k) triangular and tetrahedral elements of order k are tailor-made finite elements for approximation of vector fields in such formulations where only normal continuity is required over the element faces. They are suitable for flow-pressure formulation of fluid problems. For mixed forms of second order elliptic applications, standard $H^1(\Omega)$ -continuous approximations are well-known to cause problems in that they allow spurious modes with non-zero energy that do not exist in the continuous problem. The \mathcal{RT}_k elements are designed to approximate $H(\text{div}; \Omega)$, and does therefore not suffer from this problem. That's the reason for their popularity in the so called mixed finite element formulation.

The triangular element we exercise is edge based rather than nodal and is constructed such that the normal component of each vector valued basis function φ_i is constant one on element edge E_i and zero on the two other

edges, for $i \in \{1, 2, 3\}$. This construction will assure continuity in the normal, but not tangential, direction of a vector field over the element edges. This means that the support is restricted to the two triangles adjacent to their common edge, or one triangle if we have an exterior edge under consideration. By direct computation it can be verified that

$$\operatorname{div} \mathbf{q} \in P_0(T), \quad \text{and} \quad \mathbf{q} \cdot \mathbf{n}_i \in P_0(E_i),$$

where E_i are the edges of T and \mathbf{n}_i a unit normal vector to E_i for $i \in \{1, 2, 3\}$. It is possible to show that a piecewise polynomial function is in $H(\operatorname{div}; \Omega)$ if and only if it has continuous normal components across the edges in the triangulation. This ensures that \mathcal{RT}_0 consists of all vector fields \mathbf{q} that are locally $\mathbf{q}|_T \in ([P_0(T)]^2 + \mathbf{x}P_0(T))$, and whose constant normal components across the edges are continuous.

The standard way in the finite element community to make use of a reference element for definition of the basis functions turns out to be a bit complicated in this case. In order to make elements that are continuous in the normal direction of the mapped reference element, we must assume that the geometry mapping is affine. This is usually not the case, and a more elaborate Piola transformation has to be involved. So, the construction of the basis functions for the Raviart-Thomas spaces is most easily done in the physical configuration. Consider an element with corner nodes \mathbf{x}_i , edge vectors \mathbf{e}_i associated with edges E_i , and with edge unit normal vectors

$$\mathbf{n}_i = \begin{pmatrix} 0 & -1 \\ 1 & 0 \end{pmatrix} \frac{\mathbf{e}_i}{\|\mathbf{e}_i\|}.$$

The lowest order element basis functions can be written

$$\varphi_i = \begin{pmatrix} a_i + c_i x \\ b_i + c_i y \end{pmatrix},$$

and to construct the vector valued basis $\{\varphi_1, \varphi_2, \varphi_3\}$ on the element we need to solve

$$\varphi_i \cdot \mathbf{n}_j = \delta_{ij},$$

at the three midpoints $\mathbf{x}_{ei} = \frac{1}{2}(\mathbf{x}_i + \mathbf{x}_{i+1}) \bmod 3$ of the edges. This is a simple linear algebra problem

$$\begin{pmatrix} n_{1x} & n_{1y} & \mathbf{n}_1 \cdot \mathbf{x}_{e1} \\ n_{2x} & n_{2y} & \mathbf{n}_2 \cdot \mathbf{x}_{e2} \\ n_{3x} & n_{3y} & \mathbf{n}_3 \cdot \mathbf{x}_{e3} \end{pmatrix} \begin{pmatrix} a_i \\ b_i \\ c_i \end{pmatrix} = \mathbf{f}_i, \quad \text{with} \quad (\mathbf{f}_i)_j = \delta_{ij}.$$

The three basis functions are illustrated in Figure 4. Note that this does not yet define the basis functions for \mathcal{T}_h uniquely, because there are two unit

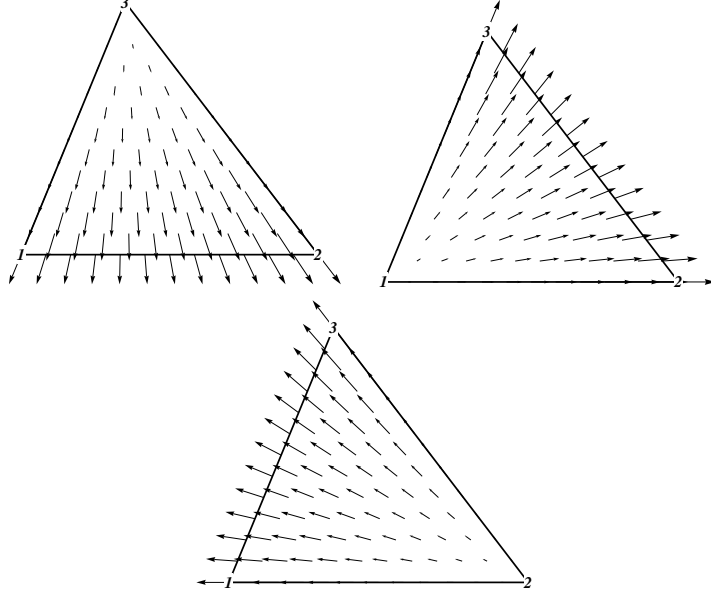


Figure 4: Lowest order Raviart-Thomas basis functions.

normal vectors to an edge. A choice for the normal can for example be made according to the numbering of the nodes in \mathcal{T}_h . For instance, let the edge vectors \mathbf{e}_i point to the node with the largest index.

Now we state our finite element problem as seek $(\mathbf{q}_h, p_h) \in \mathcal{RT}_0 \times Q_h$ such that

$$\int_{\Omega} \frac{12\mu}{H^3} \mathbf{q}_h \cdot \mathbf{v} \, d\Omega - \int_{\Omega} p_h \nabla \cdot \mathbf{v} \, d\Omega = \int_{\Omega} \frac{6\mu}{H^2} \mathbf{U} \cdot \mathbf{v} \, d\Omega, \quad \forall \mathbf{v} \in \mathcal{RT}_0, \quad (28)$$

and

$$\int_{\Omega} \nabla \cdot \mathbf{q}_h w \, d\Omega = 0, \quad \forall w \in Q_h. \quad (29)$$

3.2 Solution

For a given finite element discretization of the saddle point problem (28) and (29) we arrive at the following matrix formulation

$$\begin{pmatrix} \mathbf{A} & \mathbf{B} \\ \mathbf{B}^T & \mathbf{0} \end{pmatrix} \begin{pmatrix} \mathbf{q}_h \\ \mathbf{p}_h \end{pmatrix} = \begin{pmatrix} \mathbf{F} \\ \mathbf{0} \end{pmatrix}. \quad (30)$$

In order for this to be solved we need to have \mathbf{A} and $\mathbf{B}^T \mathbf{A}^{-1} \mathbf{B}$ invertible. Normally there is no problem in the finite element method for \mathbf{A} to be positive definite, but it is more crucial in the latter construction, due to the fact

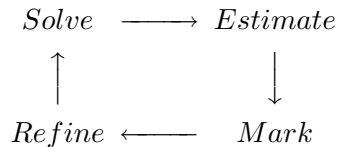
that \mathbf{B} is formed from a mix of the finite element spaces involved. However for our particular choice of spaces \mathcal{RT}_0 and Q_h the system is known to be solvable without any stability problems. The well-posedness of this problem follows from the general theory presented by Brezzi, Hager, and Raviart [5]. Cavitation occurs when the pressure reaches atmospheric pressure, which we for definiteness define as $p = 0$. The lubricant cannot support subatmospheric pressure, so an additional condition is $p \geq 0$ in Ω . In order to incorporate this condition into the model, we apply an iterative algorithm of Uzawa type to solve the system taking cavitation into consideration using a pressure projection on the run.

1. Let $k = 0$ and choose an initial \mathbf{p}_h^k .
2. Solve the linear system $\mathbf{A}\mathbf{q}_h^{k+1} = \mathbf{F} - \mathbf{B}\mathbf{p}_h^k$ for the flow field \mathbf{q}_h^{k+1} .
3. Perform Richardson update $\mathbf{p}_h^{k+1} = \mathbf{p}_h^k + \omega\mathbf{B}^T\mathbf{q}_h^{k+1}$, where ω is a relaxation parameter.
4. Project pressure field $\mathbf{p}_h^{k+1} = P_\Lambda(\mathbf{p}_h^{k+1})$, where the operator $P_\Lambda(\boldsymbol{\vartheta}) := \max(\mathbf{0}, \boldsymbol{\vartheta})$.
5. If convergence not yet achieved, set $k = k + 1$ and go back to step 2.

The projection operator P_Λ is applied element-wise on the element values for the pressure, which by construction leads to $p_h \in \{p \in L_2(\Omega) : p \geq 0\}$.

3.3 Error control

An adaptive finite element method should consist of a sequence of successive loops



The *a posteriori* error control in the *Estimate* step, and for the whole loop as well, has been investigated over the last decade for the conforming finite element method. However, the mixed finite element method and the problem at hand, i.e. with cavitation treatment via projection, is to the authors knowledge not treated in the literature. We choose to follow Carstensen and Hoppe [6].

Given a sequence of refined meshes $\{\mathcal{T}_h^i\}$ with corresponding solution \mathbf{q}_h^i and error $e_i = \|\mathbf{q} - \mathbf{q}_h^i\|$ on mesh \mathcal{T}_h^i . Then

$$e_i^2 \leq \gamma^i e_0^2 + Ci\rho^{i-1}, \quad \text{for } i = 1, 2, \dots \quad (31)$$

with constants $C > 0, 0 < \gamma < 1$ and $0 < \rho < 1$ if the refinement is done

using the following strategy. Define the error estimator

$$\eta_h = \left(\sum_{E \in \mathcal{E}_T} \eta_E^2 \right)^{1/2}, \quad \text{with} \quad \eta_E^2 := h_E \|\llbracket \mathbf{q}_h^i \rrbracket_E\|_{L_2(\Omega)}^2. \quad (32)$$

where, $\llbracket \mathbf{q}_h^i \rrbracket_E$ is the discrete jump $\llbracket \mathbf{q}_h^i \rrbracket_E := \mathbf{q}_h^i|_{T_+} - \mathbf{q}_h^i|_{T_-}$ of the flux \mathbf{q}_h^i over an interior edge $E := T_+ \cap T_-$ of the length $h_E := \text{diam}(E)$ shared by the two neighboring triangles $T_\pm \in \mathcal{T}_h^i$ and \mathcal{E}_T denotes the set of all interior edges in \mathcal{T}_h^i . We have also used the notation $\mathbf{v}|_{T_\pm} := \lim_{\epsilon \downarrow 0} \mathbf{v}(\mathbf{x} \mp \epsilon \mathbf{n})$ with $\mathbf{x} \in \Gamma_E$, and \mathbf{n} a constant unit normal vector to the edge E .

A sufficient condition for (31) to hold is now to insert new nodes on midpoints of those edges having highest indicators η_E forming next refined mesh \mathcal{T}_h^{i+1} . We refine 30% of the edges with the highest indicator in each adaptive step.

4 Numerical examples

In order to investigate the performance of the methods proposed, a few numerical examples will be presented. Unfortunately, experimental results demonstrating in detail the local behavior of the pressure and velocity images is, to our knowledge, not published. Though some integrated experimental results, such as lift, has been given by Etsion [7], [8] and Wang et. al. [14].

The object for our study is a single parabolic shaped oil pocket, Figure 5. A central longitudinal cut through the gap between the metal sheet and work piece comprise our 2D computational model. The dimensions of the nominal channel and a particular pocket can be seen in Figure 6. Boundary conditions used for the pressure is $p = 0$ at a thin slice surrounding the actual domain. Upper and lower walls are impermeable, thus $q = 0$ at applicable element edges, Figure 6. The flow is driven by the relative velocity $\mathbf{U} = (1, 0)$ between the metal sheet and the workpiece. The lubricant viscosity $\mu = 1$.

From a starting pressure $p = 0$ throughout the initial domain is the pressure field inherited to the next refined mesh using linear interpolation during the adaptivity process. Despite this is the typical number of iterations 1000, though decreasing with refinement level, for the Usawa algorithm to converge according to $\|\mathbf{p}_h^{k+1} - \mathbf{p}_h^k\| < 10^{-9}$ for a particular mesh. In order to converge, especially for deep oil pockets, Usawa needed to be relaxed by $\omega = 0.1$. All integrals involved are integrated using a 4-point Gauss quadrature scheme.

The initial mesh has a typical element side length of 0.2. In Figure 7 we visualize the adaptivity refinement progress inserting new nodes giving a sequence of meshes under consideration for a particular pocket depth. In each step the edges that give the largest third of the edge contributions to

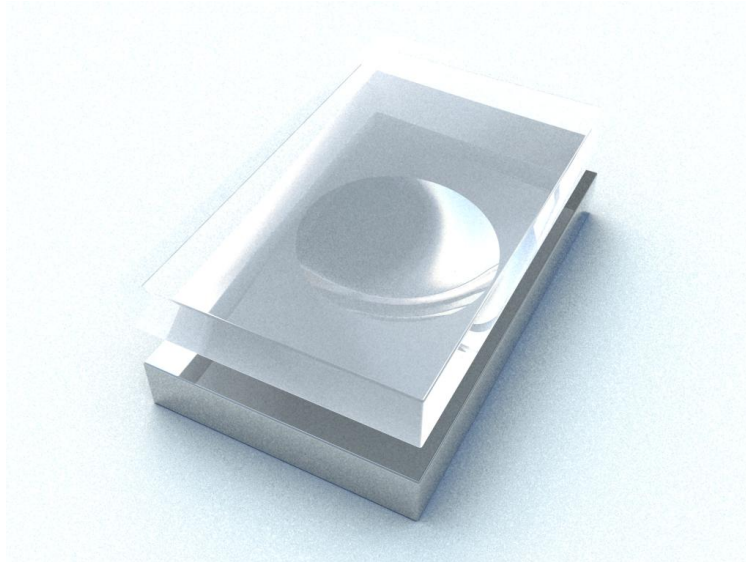


Figure 5: Oil pocket model.

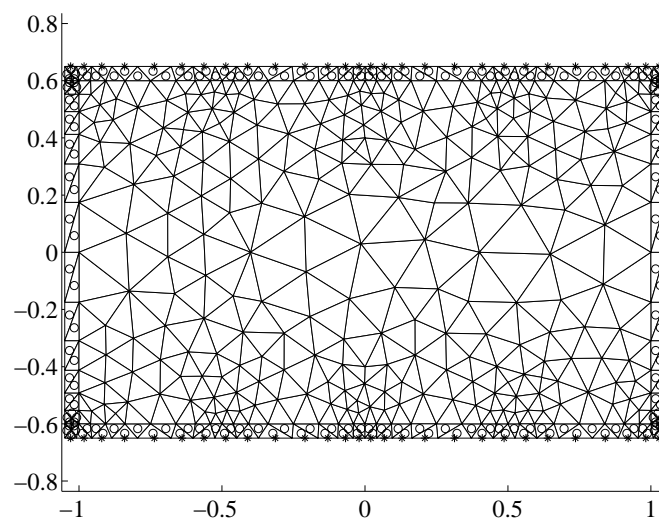


Figure 6: Initial mesh and boundary conditions. Pressure is zero at o-marked elements and flow is zero at *-marked edges.

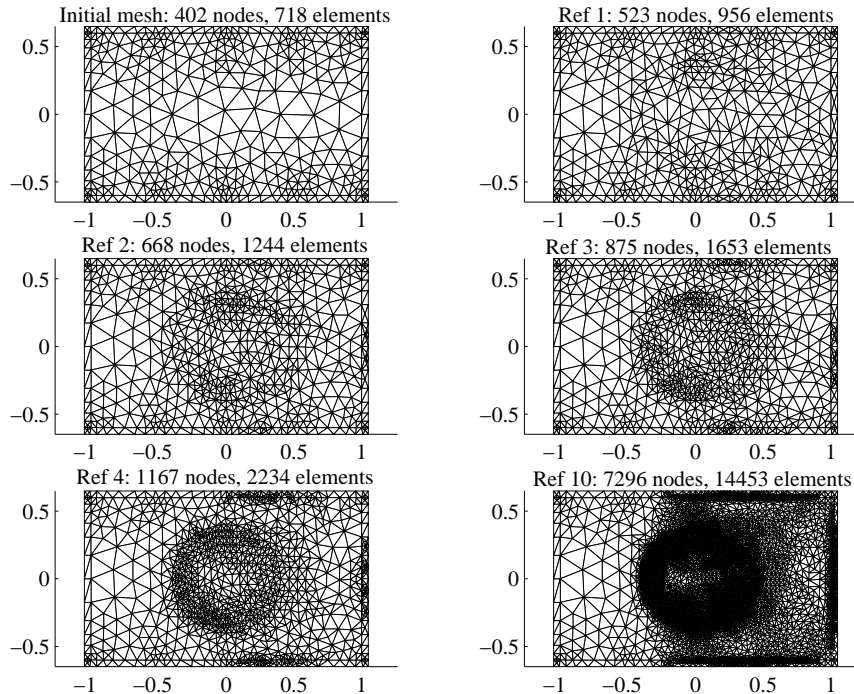


Figure 7: Sequence of refined meshes.

the total error according to relation (32) are subdivided forcing neighboring elements to be subdivided into, at least, two new ones. After refinement step 10 is the area ratio approximately 6000 for the largest element over the smallest. Likewise is the longest element side over the shortest one found to be about 115. The process indicates adaptivity to take place along the sharp edge of the oil pocket, which of course is the dramatic region of the domain.

The decrease of the total error indicator η_h , defined by (32), according to refinement, measured by the number of nodes, is presented in Figure 8. Each dot indicates a refinement step.

In Figure 9 we present the typical pressure bubble with constant pressure element and in Figure 10 we visualize the flow vector at center of elements throughout the domain. We emphasize that we do not need to *a priori* define the boundary location between the fluid and cavitation phases. This is automatically taken care of by the refinement process.

In order to compare current results with earlier ones [3], an L_2 -projection of the pressure field is applied in order to furnish a continuous piecewise linear pressure over the elements. A comparison of pressure at ceiling between

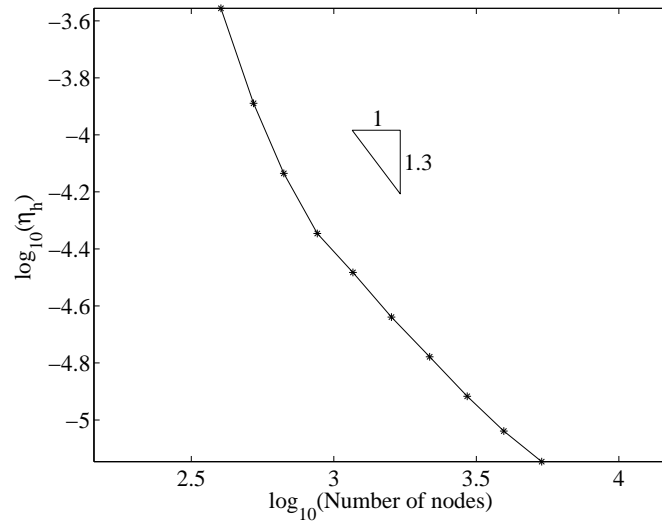


Figure 8: Error estimation according to (32). Each dot indicates a refinement step.

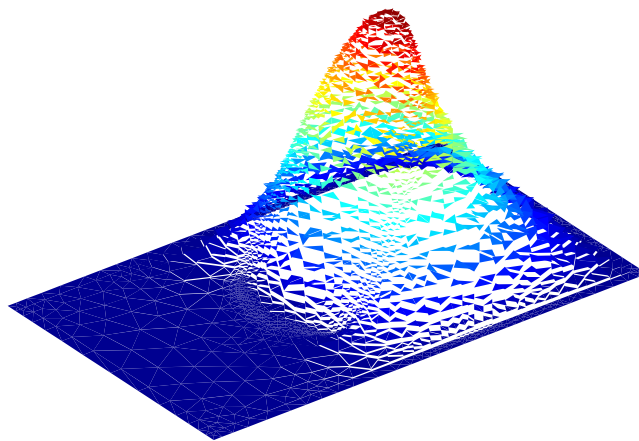


Figure 9: Pressure bubble.

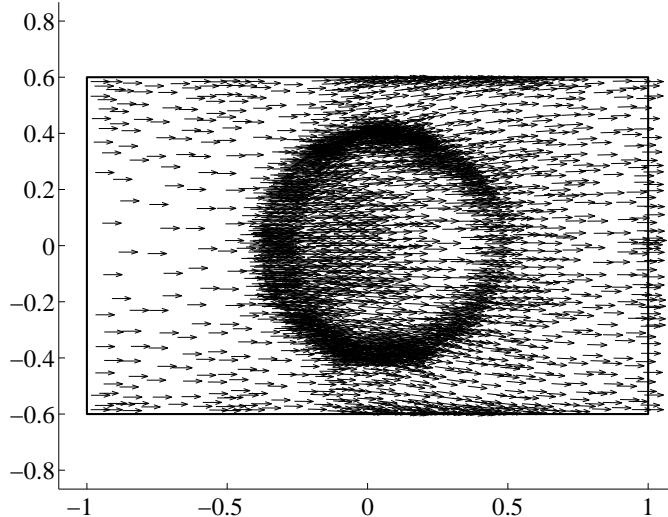


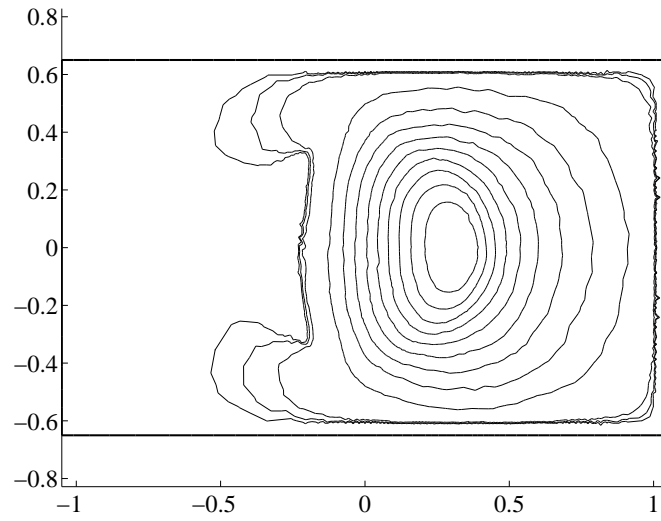
Figure 10: Flow vectors.

an adaptive Reynolds cavitation model [3] and the present model is given in Figures 11(a) and 11(b) and indicates good agreement. The classical way to approach the cavitation problem in the Reynolds community via continuity boundary conditions or first computing p^R from a pure Reynolds solution, followed by approximating $p \approx \max(0, p^R)$ (known as the half-Sommerfeld condition), is not very accurate at all compared to the cavitation model presented.

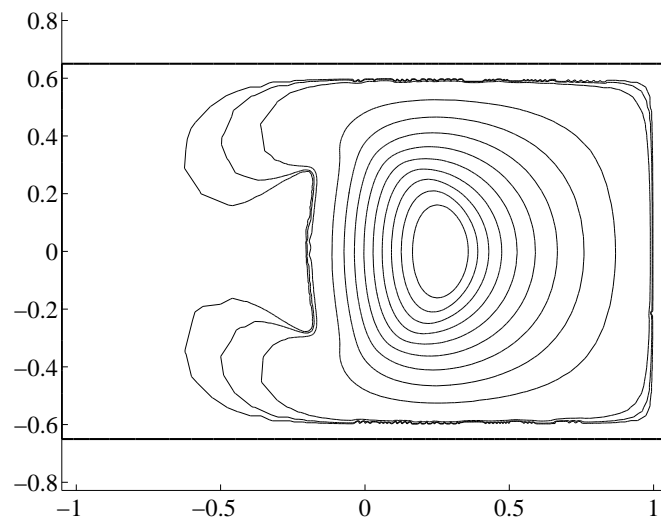
5 Concluding remarks

We have presented an apparently novel approach to cavitation in Reynolds model based on a mixed formulation, as an alternative to Reynolds pure model combined with the cruder half-Sommerfeld condition often used in lubrication analysis. We focus on the pressure drop as the source of cavitation, which has been criticized, e.g., by Joseph [11] as being dubious from a physical point of view. However, as we see it, our approach has a wider range of applicability and can in principle make use of other cavitation models, such as those of [11]; it can also be used to model stretching of cavitation bubbles due to convective phenomena.

One of our aim was also to study the behavior of the physics as the depth of the oil pocket increases while the opening width of the pocket and channel height stays the same in order to indicate an oil pocket depth that is better than all other to produce lift. But the story goes for this mixed



(a) Current model.



(b) Reynolds cavitation model [3].

Figure 11: Contour lines for comparison of pressure at ceiling for current model and the one in [3].

formulation as the one presented in [3]. Reynolds simplified flow model is unable to indicate such a depth. To achieve this information we have to go to a similar cavitation model based on Stokes flow model, as investigated in [4].

Future research will focus on cavitating flows for the full transient Navier-Stokes equations, for which a simple cavitation model such as ours can be an alternative for some aspects of cavitation, compared to more elaborate models incorporating several physical phenomena.

References

- [1] Bayada G., Chambat M., *The transition between the Stokes equation and the Reynolds equation: a mathematical proof*, Appl. Math. Optim., 1986;**14**:73–93.
- [2] Becker R., Rannacher R., *An optimal control approach to a posteriori error estimation in finite element methods*, Acta Numer., 2001;**10**:1–102.
- [3] Nilsson B., Hansbo P., *Adaptive finite element methods for hydrodynamic lubrication with cavitation*, Int. J. Numer. Methods Engrg., 2007;**72**:1584–1604.
- [4] Nilsson B., Hansbo P., *A Stokes model with cavitation for the numerical simulation of hydrodynamic lubrication*, Preprint, Department of Mathematical Sciences, Chalmers University of Technology, 2008.
- [5] Brezzi F., Hager W. W., Raviart P.-A., *Error estimates for the finite element solution of variational inequalities. Part II. Mixed methods*, Numer. Math., 1978;**31**:1–16.
- [6] Carstensen C., Hoppe R. H. W., *Error reduction and convergence for an adaptive mixed finite element method*, Math. Comp., 2006;**75**:1033–1043.
- [7] Etsion I., Burstein L., *A model for mechanical seals with regular micro-surface structure*, Tribology Transactions, 1996;**39**:677–683.
- [8] Etsion I., Kligerman Y., Halperin G., *Analytical and Experimental Investigation of Laser-Textured Mechanical Seal Faces*, Tribology Transactions, 1999;**42**:511–516.
- [9] Hansbo P., *Three lectures on error estimation and adaptivity*, in: E. Stein (Ed.), *Adaptive Finite Elements in Linear and Nonlinear Solid*

and Structural Mechanics, CISM Courses and Lectures No. **416**:149–193, Springer, 2005.

- [10] Haslinger J., *Mixed formulations of elliptic variational inequalities and its approximation*, *Apl. Mat.*, 1981;**26**:462–475.
- [11] Joseph D. D., *Cavitation and the state of stress in a flowing liquid*, *J. Fluid Mech.*, 1998;**366**:367–378.
- [12] Slimane L., Bendali A., Laborde P., *Mixed formulations for a class of variational inequalities*, *ESAIM: Math. Model. Numer. Anal.*, 2004;**38**:177–201.
- [13] Suttmeier F.-T., *On computational methods for variational inequalities*, *Comput. Mech.*, 2005;**35**:401–408.
- [14] Wang X., Kato K., Adachi A., Aizawa K., *Load carrying capacity map for the surface texture design of SiC thrust bearing sliding in water*, *Tribology International*, 2003;**36**:189–197.

Paper IV

Weak coupling of a Reynolds model and a Stokes model for hydrodynamic lubrication

Bertil Nilsson

*Center for Applied Mathematics and Physics,
Halmstad University,
SE-301 18 Halmstad, Sweden*

Peter Hansbo

*Department of Mathematical Sciences,
Chalmers University of Technology
and University of Gothenburg, SE-412 96 Göteborg, Sweden*

Abstract

The Reynolds model is a reduced Stokes model, valid for narrow lubrication regions. In order to be able to handle locally non-narrow regions such as pits or grooves, often displaying or rapid geometrical variations, there is a need to be able to transit to the more accurate Stokes model. A fundamental problem is how to couple the two models in a numerical simulation, preferably allowing for different meshes in the different domains. In this paper, we present a weak coupling method for Reynolds and Stokes models for lubrication computations. is taken into account. The paper concludes with some numerical examples.

1 Introduction

In approximating thin fluid films typically appearing in lubrication, simplifying assumptions (discussed below) introduced by Reynolds in the 19:th century [7] are typically introduced in order to remove the dimension associated with the thickness of the film. In many situations, one or more of these assumptions must be dropped in order to make accurate predictions of the actual flow. If, however, the Reynolds assumptions hold in a substantial part of the domain of interest, there is a large computational gain in making a model coupling between the Reynolds model and a more accurate model such as Stokes or Navier–Stokes equations. An example of such a coupling scheme, between Stokes and Reynolds equations, is given by

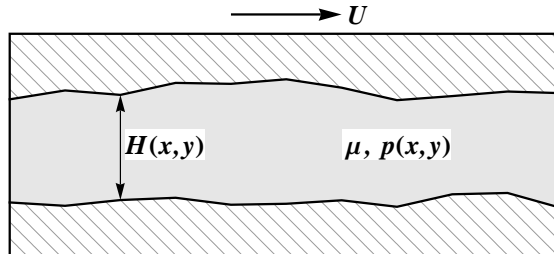


Figure 1: Reynolds channel.

Stay and Barocas [8], who formulate the Reynolds problem in terms solely of the pressure and apply stress balance and velocity continuity conditions on the interface. In this paper we take a more direct approach in that we pose both the Stokes and Reynolds equations on mixed form with unknowns for velocity and pressure. In the Reynolds case, the velocity variable then represents the flow rate, i.e., the integral of the physical velocity across the interface thickness. In posing this mixed formulation, we obtain a natural coupling method based on convex minimization with constraints: divergence zero constraints in both the Stokes and Reynolds domains, and continuity constraints between the mean velocities across the coupling interface.

2 Reynolds equation

The first mathematical approach to tribology was undertaken by Leonard Euler with a geometrical resistance theory of "dry" friction - the *Interlocking Asperity Theory*. Euler's theory provides us with the two well known terms for static and dynamic friction. The static friction coefficient is provided by the tangent of the asperity angle, while the dynamic friction coefficient is reduced by the kinetic term. But the true workhorse for many of years is of course the Reynolds equation [7]. It has been used successfully to determine the pressure distribution in the fluid film for a wide range of applications from bearings, seals to sheet metal forming processes.

In the spirit of Figure 1, where a typical channel is furnished with the x -axis oriented as the relative surface velocity \mathbf{U} and z -axis upwards, he made the following assumptions:

1. Body forces are neglected, i.e. there are no extra fields of forces acting on the fluid.
2. The pressure is constant through the thickness of the film.

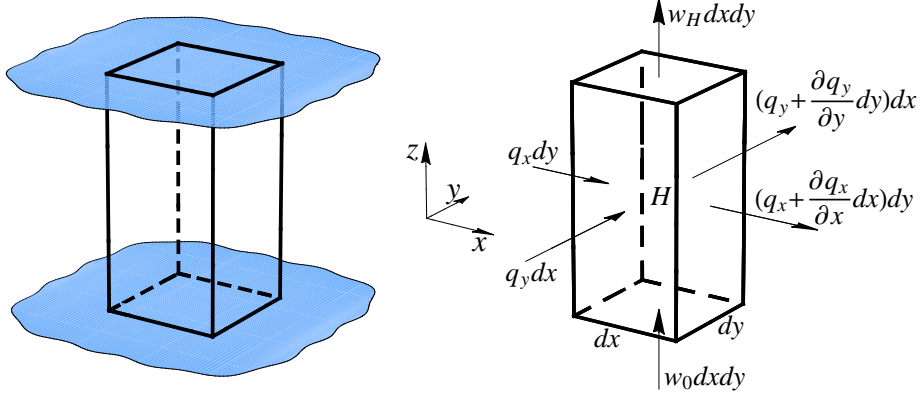


Figure 2: Continuity of flow in a column of height H .

3. The curvature of surfaces is large compared with film thickness. Surface velocities need not be considered as varying in direction.
4. There is no slip at the boundaries.
5. The lubricant is Newtonian, i.e. stress is proportional to rate of shear.
6. The flow is laminar.
7. Fluid inertia is neglected.
8. The viscosity is constant through the film thickness.

With these assumptions considered, the development of the equations can start. First, continuity of flow is examined.

2.1 Continuity of flow of a column

Consider a thin column of fluid of height $H(x, y)$ and base dx, dy , Figure 2. Fluid flows from the left at a rate q_x per unit width so the volume flow rate is $q_x dy$ into the column. The rate of flow out per unit width is

$$q_x + \frac{\partial q_x}{\partial x} dx, \quad (1)$$

where $\frac{\partial q_x}{\partial x}$ is the rate of change of flow in the x -direction. The actual flow out is

$$\left(q_x + \frac{\partial q_x}{\partial x} dx \right) dy. \quad (2)$$

In the y -direction the same argument applies. The flow rate in is $q_y dx$ and out is

$$\left(q_y + \frac{\partial q_y}{\partial y} dy \right) dx. \quad (3)$$

The vertical flow is rather different. If the floor of the column moves upwards at a velocity w_0 and if the roof moves upward as well at a speed w_H the volume of the column changes at a rate $(w_H - w_0) dx dy$. Although the base and roof are moving, at the instant considered the height is H , though a fraction of time later it will of course have altered.

An alternative possibility is that the floor and/or roof are porous, and fluid is flowing in at a velocity w_0 or out of the column at a velocity w_H . The fluid velocity can be considered constant over the very small base area $dx dy$ hence the increase of volume is at a rate $w_0 dx dy$ and fluid leaves at a rate $w_H dx dy$.

For continuity of flow, the fluid being of constant density, the rate flowing in must equal the rate flowing out. These can all be added up. Flowing into the column

$$q_x dy + q_y dx + w_0 dx dy, \quad (4)$$

and flowing out

$$\left(q_x + \frac{\partial q_x}{\partial x} dx \right) dy + \left(q_y + \frac{\partial q_y}{\partial y} dy \right) dx + w_H dx dy. \quad (5)$$

These two are equal, equating them and canceling,

$$\frac{\partial q_x}{\partial x} dx dy + \frac{\partial q_y}{\partial y} dy dx + (w_H - w_0) dx dy = 0. \quad (6)$$

Now $dx dy$ is arbitrary and non zero, hence can be canceled giving the continuity of flow of a column as

$$\frac{\partial q_x}{\partial x} + \frac{\partial q_y}{\partial y} + (w_H - w_0) = 0. \quad (7)$$

If the top and bottom surfaces are impermeable, $w_H - w_0$ is the rate of change of height of the column according to time and may be written $\frac{\partial H}{\partial t}$. Having obtained the continuity it is necessary to look at the force balance of an element of the fluid.

2.2 Equilibrium of an element

Take a small element of fluid of sides dx, dy and dz , Figure 3, and consider first the forces in the x -direction only. On the left of the element there is

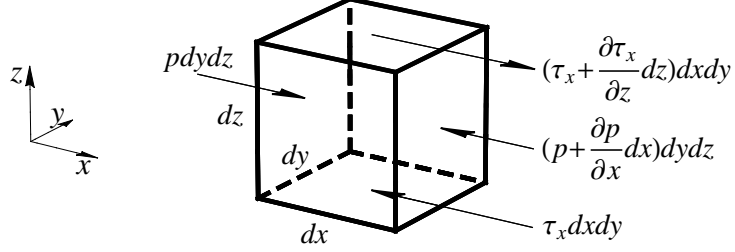


Figure 3: Equilibrium of an element.

a pressure p on the face of area $dydz$ giving a force of $pdydz$ acting to the right. On the opposite face the pressure is

$$p + \frac{\partial p}{\partial x} dx, \quad (8)$$

and the corresponding force is

$$\left(p + \frac{\partial p}{\partial x} dx \right) dydz. \quad (9)$$

There are shear stresses on the top and bottom faces producing forces. On the bottom face the shear stress τ_x gives a force $\tau_x dx dy$ acting to the left and on the top face, and acting to the right, is a force

$$\left(\tau_x + \frac{\partial \tau_x}{\partial z} dz \right) dx dy, \quad (10)$$

where the shear stress on the top face being $\tau_x + \frac{\partial \tau_x}{\partial z} dz$. These forces acting to the left and right must balance each other so

$$pdydz + \left(\tau_x + \frac{\partial \tau_x}{\partial z} dz \right) dx dy = \left(p + \frac{\partial p}{\partial x} dx \right) dydz + \tau_x dx dy, \quad (11)$$

expanding and canceling considering $dx dy dz$ an arbitrary non zero volume gives

$$\frac{\partial \tau_x}{\partial z} = \frac{\partial p}{\partial x}. \quad (12)$$

Now Newton's viscosity relation states

$$\tau_x = \mu \frac{\partial u}{\partial z}, \quad (13)$$

where u is the velocity of the fluid in the x -direction, so

$$\frac{\partial}{\partial z} \left(\mu \frac{\partial u}{\partial z} \right) = \frac{\partial p}{\partial x}. \quad (14)$$

In the y -direction where the velocity of the fluid is v the shear stresses and pressures can be equated and a similar equation follows

$$\frac{\partial \tau_y}{\partial z} = \frac{\partial p}{\partial y}, \quad \text{where} \quad \tau_y = \mu \frac{\partial v}{\partial z},$$

so

$$\frac{\partial}{\partial z} \left(\mu \frac{\partial v}{\partial z} \right) = \frac{\partial p}{\partial y}. \quad (15)$$

The pressure gradient in the z -direction is by assumption zero, so $\frac{\partial p}{\partial z} = 0$. Consider now equation (14) further. This can be integrated since p is not a function of z , thus

$$\mu \frac{\partial u}{\partial z} = \frac{\partial p}{\partial x} z + C_1. \quad (16)$$

Now both μ and u are functions of z but it is in this context too difficult to consider both at once so μ is taken as constant with respect to z as stated in assumption 8. It is important to realize that this is a big assumption and is only made for simplicity. The inclusion of $\frac{\partial \mu}{\partial z}$ can modify the equation very considerably in certain circumstances. However, using this assumption, a further integration can be performed to give

$$\mu u = \frac{\partial p}{\partial x} \frac{z^2}{2} + C_1 z + C_2. \quad (17)$$

The boundary conditions are simple, according to assumption 4, i.e. no slip at the boundaries

$$\begin{cases} u(0) = U_0 \\ u(H) = U_H \end{cases}, \quad (18)$$

so (17) and (18) gives

$$u = \frac{1}{2\mu} \frac{\partial p}{\partial x} (z^2 - zH) + (U_H - U_0) \frac{z}{H} + U_0. \quad (19)$$

Finally the flow rate $q_x = \int_0^H u dz$ in the x -direction per unit width of y

$$q_x = -\frac{H^3}{12\mu} \frac{\partial p}{\partial x} + (U_0 + U_H) \frac{H}{2}. \quad (20)$$

If the same procedure is followed for y using equation (15) it is easily found that

$$q_y = -\frac{H^3}{12\mu} \frac{\partial p}{\partial y} + (V_0 + V_H) \frac{H}{2}, \quad (21)$$

where V_0 and V_H in the y -direction correspond to U_0 and U_H in the x -direction.

It is now possible to replace (20) and (21) into the continuity equation (7)

$$\frac{\partial}{\partial x} \left(\frac{H^3}{\mu} \frac{\partial p}{\partial x} \right) + \frac{\partial}{\partial y} \left(\frac{H^3}{\mu} \frac{\partial p}{\partial y} \right) = 6 \left(\frac{\partial}{\partial x} ((U_0 + U_H) H) + \frac{\partial}{\partial y} ((V_0 + V_H) H) + 2(w_H - w_0) \right). \quad (22)$$

This is the full Reynolds equation in terms of the pressure as usually stated, and in particular as used in [8].

3 A mixed formulation of Reynolds equation

In order to formulate a coupling method between Reynolds equation and more accurate fluid models, we reintroduce the flow rates from (20)–(21) and pose the problem as that of finding (\mathbf{q}, p) such that

$$\begin{aligned} \frac{12\mu}{H^3} \mathbf{q} + \nabla p &= \frac{6\mu}{H^2} \mathbf{U}, \\ \nabla \cdot \mathbf{q} &= 0. \end{aligned}$$

where it has been assumed that the thickness of the film does not change over time and that $\mathbf{U} = (U_0, U_H) = (0, U_H)$ and $\mathbf{V} = \mathbf{0}$.

In weak form, this problem may be written as seeking $\mathbf{q} \in H(\text{div}; \Omega)$, where

$$H(\text{div}, \Omega) = \{\mathbf{v} \in [L_2(\Omega)]^2 : \|\nabla \cdot \mathbf{v}\|_{L_2(\Omega)} < \infty\},$$

and $p \in L_2(\Omega)$, $L_2(\Omega)$ being the space of square-integrable functions over Ω , such that

$$\int_{\Omega} \frac{12\mu}{H^3} \mathbf{q} \cdot \mathbf{v} \, d\Omega - \int_{\Omega} p \nabla \cdot \mathbf{v} \, d\Omega = \int_{\Omega} \frac{6\mu}{H^2} \mathbf{U} \cdot \mathbf{v} \, d\Omega, \quad \forall \mathbf{v} \in H(\text{div}; \Omega), \quad (23)$$

and

$$\int_{\Omega} \nabla \cdot \mathbf{q} w \, d\Omega = 0, \quad \forall w \in L_2(\Omega). \quad (24)$$

Boundary conditions for this problem are either handled strongly, in the case of conditions on the normal flow rate, or weakly in the case of conditions on the pressure.

4 The coupled problem

We are interested in coupling the Reynolds model with the Stokes model across a vertical interface. The interface from the Reynolds side then appears one-dimensional, while the interface on the Stokes side is two-dimensional.

Denote by Ω_R the Reynolds domain, Ω_S the Stokes domain, by Γ_{1D} the dimensionally reduced interface, and by $\Gamma_{2D} := \Gamma_{1D} \times H$ the full 2D interface. We have the following problem to solve taking cavitation into consideration:

$$\begin{aligned}
\frac{12\mu}{H^3} \mathbf{q} + \nabla p_R &= \frac{6\mu}{H^2} \mathbf{U} \text{ in } \Omega_R \subset \mathbb{R}^2, \\
\nabla \cdot \mathbf{q} &= 0 \text{ in } \Omega_R, \\
-\mu \Delta \mathbf{u} + \nabla p_S &= 0 \text{ in } \Omega_S \subset \mathbb{R}^3, \\
\nabla \cdot \mathbf{u} &= 0 \text{ in } \Omega_S, \\
\int_0^H \sigma_n(\mathbf{u}, p_S) dz + p_R &= 0 \text{ on } \Gamma_{1D}, \\
(\mathbf{q} - \int_0^H \mathbf{u} dz) \cdot \mathbf{n} &= 0 \text{ on } \Gamma_{1D}.
\end{aligned} \tag{25}$$

This problem must then be supplemented with boundary conditions on the exterior boundaries, which depend on the type of model adjacent to the exterior. These are handled in the usual way in the finite element setting.

4.1 Finite element formulation

To formulate our method, we suppose that we have regular finite element partitions \mathcal{T}_h^i , $i \in \{R, S\}$ of the two subdomains Ω_R and Ω_S into shape regular simplexes. These two meshes imply the existence of trace meshes on the interface

$$\mathcal{G}_h^i = \{E : E = T \cap \Gamma_{2D}, \forall T \in \mathcal{T}_h^i, i \in \{R, S\}\}.$$

From the finite element theory of mixed methods, it is well known that one must carefully select the combination of approximations for the flow variables and the pressure. In the case of the Reynolds model, a well known stable element combination is the lowest order Raviart-Thomas approximation for the flow rate, i.e., $\mathbf{q}^h \in V_h^R$, where

$$V_h^R := \{\mathbf{q} \in H(\text{div}, \Omega) : \mathbf{q}|_T \in (P_0(T))^2 + \mathbf{x}P_0(T), \forall T \in \mathcal{T}_h^R\}$$

combined with a pressure space of elementwise constant pressures,

$$Q_h^R := \{p \in L_2(\Omega) : p|_T \in P_0(T), \forall T \in \mathcal{T}_h^R\}.$$

In the case of Stokes flow, we choose to use the well known stable Taylor-Hood element consisting of the velocity space

$$V_h^S := \{\mathbf{u} \in [C^0(\Omega)]^3 : \mathbf{u}|_T \in (P_2(T))^3, \forall T \in \mathcal{T}_h^S\}$$

and pressure space

$$Q_h^S := \{p \in C^0(\Omega) : p|_T \in P_1(T), \forall T \in \mathcal{T}_h^S\}.$$

Cavitation occurs when the pressure reaches atmospheric pressure, which we for definiteness define as $p = 0$. The lubricant cannot support subatmospheric pressure, so an additional condition is $p \geq 0$ in $\Omega_R \cup \Omega_S$. In order to incorporate this condition into the model, it can be written as a variational inequality. For this purpose we define the space

$$K = \{p \in L_2(\Omega) : p \geq 0\}.$$

We shall use a Lagrange multiplier method using piecewise constants on the 1D trace mesh \mathcal{G}_h^R for the fulfillment of the continuity requirement on the velocities. We seek $(\mathbf{q}^h, \mathbf{u}^h, p_R^h, p_S^h, \lambda^h) \in V_h^R \times V_h^S \times Q_h^R \times Q_h^S \times \mathcal{C}_h$, where

$$\mathcal{C}_h := \{\kappa \in L_2(\Gamma_{1D}) : \kappa|_E \in P_0(E), \forall E \in \mathcal{G}_h^R\},$$

such that

$$\begin{aligned} a_h((\mathbf{q}^h, \mathbf{u}^h), (\mathbf{v}_R, \mathbf{v}_S)) + b_h((p_R^h, p_S^h), (\mathbf{v}_R, \mathbf{v}_S)) + c_h(\lambda^h, (\mathbf{v}_R, \mathbf{v}_S)) &= f_h(\mathbf{v}_R), \\ \forall (\mathbf{v}_R, \mathbf{v}_S) \in V_h^R \times V_h^S, \end{aligned} \quad (26)$$

$$b_h((p_R^h - w_R, p_S^h - w_S), (\mathbf{q}^h, \mathbf{u}^h)) \leq 0, \quad \forall (w_R, w_S) \in (Q_h^R \cap K) \times (Q_h^S \cap K), \quad (27)$$

and

$$c_h(\kappa, \mathbf{q}^h, \mathbf{u}^h) = 0, \quad \forall \kappa \in \mathcal{C}_h. \quad (28)$$

Here

$$\begin{aligned} a_h((\mathbf{q}, \mathbf{u}), (\mathbf{v}_R, \mathbf{v}_S)) &:= \int_{\Omega_R} \frac{12\mu}{H^3} \mathbf{q} \cdot \mathbf{v}_R d\Omega + \int_{\Omega_S} \mu \nabla \mathbf{u} : \nabla \mathbf{v}_S d\Omega, \\ b_h((w_R, w_S), (\mathbf{v}_R, \mathbf{v}_S)) &:= - \int_{\Omega_R} w_R \nabla \cdot \mathbf{v}_R d\Omega - \int_{\Omega_S} w_S \nabla \cdot \mathbf{v}_S d\Omega, \\ c_h(\gamma, (\mathbf{v}_R, \mathbf{v}_S)) &:= \int_{\Gamma_{2D}} \gamma \mathbf{n} \cdot (\mathbf{v}_R - \int_0^H \mathbf{v}_S dz) ds, \\ f_h(\mathbf{v}_R) &:= \int_{\Omega_R} \frac{6\mu}{H^2} \mathbf{U} \cdot \mathbf{v}_R d\Omega. \end{aligned} \quad (29)$$

It is clear from the formulation that on every one-dimensional element side on \mathcal{G}_h^R the (constant) normal component of the flow rate will be set equal to the mean of the Stokes velocities over the height (multiplied by the height). The problem could thus alternatively be posed in a discrete space where this side condition is used directly in the definition of the space. The well-posedness of this problem follows from the general theory presented by Brezzi, Hager, and Raviart [3], and for the interface condition in this setting we refer to the closely related approach of Alonso et al. [1].

4.2 Solution

For solving this nonlinear saddle point problem, we have chosen to use an Uzawa iteration method. In order to find a good initial solution, we first assemble the finite element matrices emanating from full model (25), written using the unrestricted spaces (that are actually used in the iterations)

$$\begin{pmatrix} \mathbf{K}_S & \mathbf{B}_d & \mathbf{0} & \mathbf{0} & \mathbf{C}_S \\ \mathbf{B}_d^T & \mathbf{0} & \mathbf{0} & \mathbf{0} & \mathbf{0} \\ \mathbf{0} & \mathbf{0} & \mathbf{K}_q & \mathbf{K}_p & \mathbf{C}_R \\ \mathbf{0} & \mathbf{0} & \mathbf{K}_p^T & \mathbf{0} & \mathbf{0} \\ \mathbf{C}_S^T & \mathbf{0} & \mathbf{C}_R^T & \mathbf{0} & \mathbf{S}_\lambda \end{pmatrix} \begin{pmatrix} \mathbf{u}^h \\ \mathbf{p}_S^h \\ \mathbf{q}^h \\ \mathbf{p}_R^h \\ \boldsymbol{\lambda}^h \end{pmatrix} = \begin{pmatrix} \mathbf{0} \\ \mathbf{0} \\ \mathbf{F}_q \\ \mathbf{0} \\ \mathbf{0} \end{pmatrix}, \quad (30)$$

where the submatrices are the assembled element matrices according to the integrals found in (29), i.e. with $(\mathbf{v}_R, \mathbf{v}_S, w_R, w_S, \kappa) \in V_h^R \times V_h^S \times Q_h^R \times Q_h^S \times \mathcal{C}_h$ denoting generic basis functions spanning the relevant spaces, we have

$$\begin{aligned} \mathbf{K}_S &= \bigoplus_{T \in \mathcal{T}_h^S} \int_T \mu \nabla \mathbf{v}_S : \nabla \mathbf{v}_S \, d\Omega, \quad \mathbf{B}_d = - \bigoplus_{T \in \mathcal{T}_h^S} \int_T w_S \nabla \cdot \mathbf{v}_S \, d\Omega, \\ \mathbf{K}_q &= \bigoplus_{T \in \mathcal{T}_h^R} \int_T \frac{12\mu}{H^3} \mathbf{v}_R \cdot \mathbf{v}_R \, d\Omega, \quad \mathbf{K}_p = \bigoplus_{T \in \mathcal{T}_h^R} \int_T w_R \nabla \cdot \mathbf{v}_R \, d\Omega, \\ \mathbf{F}_q &= \bigoplus_{T \in \mathcal{T}_h^R} \int_T \frac{6\mu}{H^2} \mathbf{U} \cdot \mathbf{v}_R \, d\Omega, \\ \mathbf{C}_R &= \bigoplus_{E \in \mathcal{G}_h^R} \int_E \mathbf{n} \cdot \mathbf{v}_R \, ds, \quad \mathbf{C}_S = - \bigoplus_{E \in \mathcal{G}_h^R} \int_E \int_0^H \mathbf{n} \cdot \mathbf{v}_S \, dz \, ds, \quad \mathbf{S}_\lambda = \mathbf{0}, \end{aligned}$$

where \bigoplus denotes the assembly operator for the finite element matrix construction. We emphasize that in this particular case there is no need for stabilization of the multipliers, thus $\mathbf{S}_\lambda = \mathbf{0}$. A simple stabilization method could for instance mimic the idea of letting neighboring edges along \mathcal{G}_h^R be connected by springs with spring constants k_λ , giving

$$\mathbf{S}_\lambda = \bigoplus_{E \in \mathcal{G}_h^R} k_\lambda \begin{pmatrix} 1 & -1 \\ -1 & 1 \end{pmatrix}.$$

The system (30) is fed repeatedly into a direct linear equation solver. In each round is a simple cavitation requirement $p_S^h = \max(p_S^h, 0)$ enforced and a modification of the corresponding residuals (out-of-balance residual forces) carried out. This process is repeated until $p_S^h \geq 0$ throughout the Stokes domain. The artificial pressure boundary conditions are then released and the model with current solution state is handed over to Uzawa taking

cavitation into consideration using a pressure projection on the run. The Stokes and Reynolds models are solved in parallel as described in Hansbo and Nilsson [5], and Nilsson [6]. We supply the details.

A core operation in Uzawa algorithm is to update the pressure field. However, recall that $p = -\lim_{\kappa \rightarrow \infty} \kappa \nabla \cdot \mathbf{u}$, but $\nabla \cdot V_h^S$ does not reside in Q_h^S , due to the fact that we are using Taylor-Hood elements, so in step 3 we find a continuous pressure corrector $p_d \in Q_h^S$.

1. Let $k = 0$ and choose as initial pressure solution ${}^k \mathbf{p}_S^h$ and ${}^k \mathbf{p}_R^h$ provided by the solution strategy of the linear system (30) just described.

2. Solve the condensed version of the linear system (30)

$$\begin{pmatrix} \mathbf{K}_S & \mathbf{0} & \mathbf{C}_S \\ \mathbf{0} & \mathbf{K}_q & \mathbf{C}_R \\ \mathbf{C}_S^T & \mathbf{C}_R^T & \mathbf{S}_\lambda \end{pmatrix} \begin{pmatrix} {}^k \mathbf{u}^h \\ {}^k \mathbf{q}^h \\ {}^k \boldsymbol{\lambda}^h \end{pmatrix} = \begin{pmatrix} -\mathbf{B}_d^k \mathbf{p}_S^h \\ \mathbf{F}_q - \mathbf{K}_p^k \mathbf{p}_R^h \\ \mathbf{0} \end{pmatrix},$$

for the vector fields ${}^k \mathbf{u}^h$ and ${}^k \mathbf{q}^h$ and the Lagrange multipliers ${}^k \boldsymbol{\lambda}^h$.

3. Find a continuous pressure corrector $p_d \in Q_h^S$ from the system $\int_{\Omega_S} p_d q \, d\Omega = -\int_{\Omega_S} \nabla \cdot \mathbf{u}^h q \, d\Omega, \forall q \in Q_h^S \Leftrightarrow \mathbf{M}_d \mathbf{p}_d = \mathbf{B}_d^k \mathbf{u}^h$, where \mathbf{M}_d is the lumped mass matrix, which makes the update fast.

4. Update pressure fields

$$\begin{cases} {}^{k+1} \mathbf{p}_S^h = P_\Lambda({}^k \mathbf{p}_S^h + \omega_S \mathbf{p}_d) \\ {}^{k+1} \mathbf{p}_R^h = P_\Lambda(\mathbf{F}_q + \omega_R \mathbf{K}_p^T {}^k \mathbf{q}^h) \end{cases}$$

where ω_S and ω_R are relaxation parameters and the operator $P_\Lambda(\boldsymbol{\vartheta}) := \max(\mathbf{0}, \boldsymbol{\vartheta})$.

5. If convergence not yet achieved, set $k = k + 1$ and go back to step 2.

The projection operator P_Λ is applied point-wise on the nodal values for the pressure, which by construction leads to $\{p_R^h, p_S^h\} \in K$.

The typical number of iterations is then 200 for the Uzawa algorithm, using well tuned relaxation for the two models, to converge according to $\|{}^{k+1} \mathbf{p}_S^h - {}^k \mathbf{p}_S^h\| + \|{}^{k+1} \mathbf{p}_R^h - {}^k \mathbf{p}_R^h\| < 10^{-9}$ for a particular mesh. For the numerical evaluation of the integrals involved in the coupling matrices, \mathbf{C}_R and \mathbf{C}_S , a 2-point Gauss quadrature scheme is used on the edges of the one-dimensional trace mesh \mathcal{G}_h^R and a 3-point Gauss quadrature scheme for companion surface integrals on the Stokes mesh.

5 Numerical examples

In order to investigate the performance of the method proposed, a numerical example will be presented. Of course, experimental results demonstrating in detail the local behavior of the pressure and velocity images for the two physical models glued together is hard to achieve.

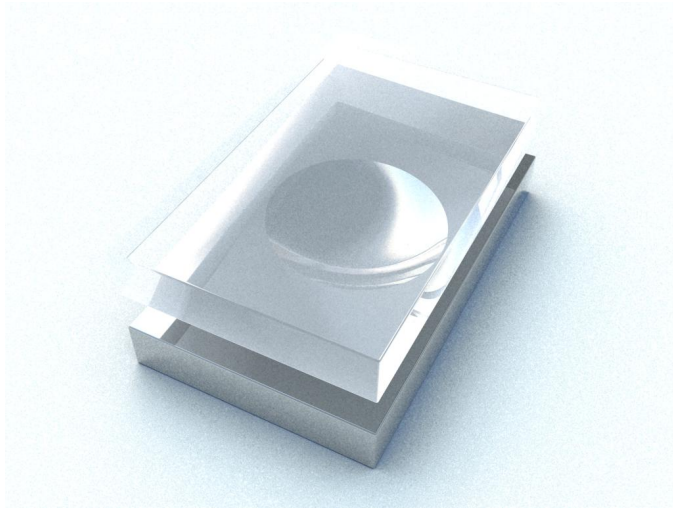
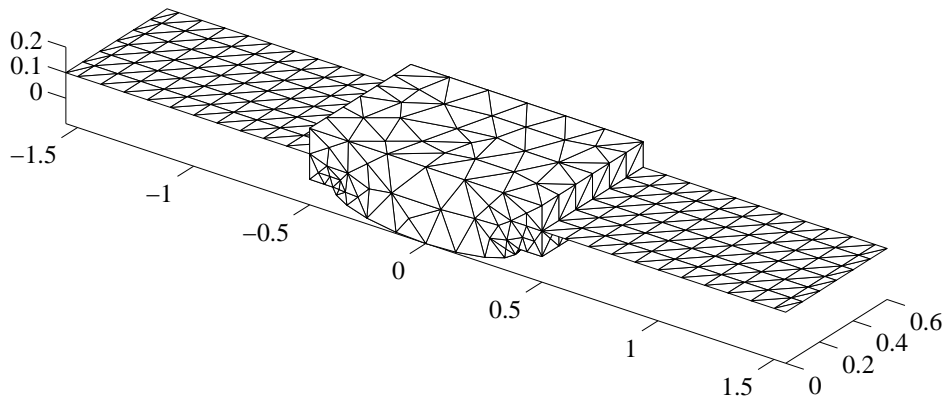


Figure 4: Oil pocket model.

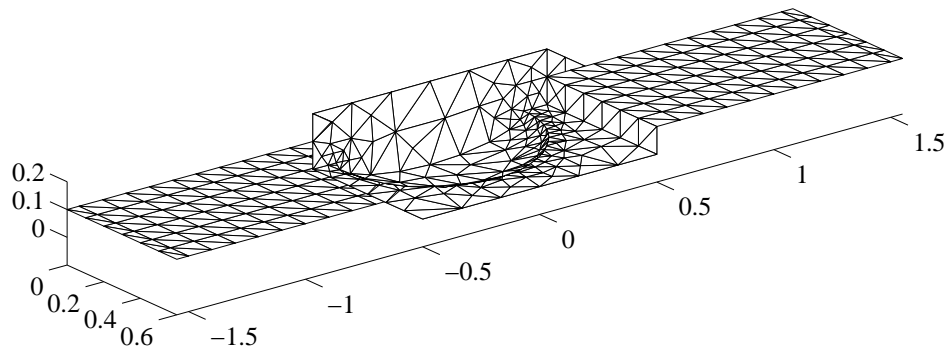
The object for our study is a single parabolic shaped oil pocket, Figure 4. A central longitudinal cut through the gap between the sheet metal and work piece comprise our full symmetrical 3D computational Stokes model. The nominal channel has the dimensions $x \times y \times z = [-0.5, 0.5] \times [0, 0.6] \times [0, 0.2]$ and the particular parabolic oil pocket is shaped as $(x/0.4)^2 + (y/0.4)^2 + (z/0.1)^2 = 1$. The narrow lubrication regions modeled by Reynolds equation is used as transit parts between the Stokes models. We investigate one Stokes part combined with two Reynolds parts of rectangular shape, the inlet part $x \times y = [-1.6, -0.5] \times [0, 0.6]$ and the outlet part $x \times y = [0.5, 1.6] \times [0, 0.6]$. The finite element model can be inspected in Figure 5.

Boundary conditions used for the pressure is $p = 0$ at inlet $x = -1.6$ and outlet $x = 1.6$ parts of the narrow Reynolds regions. Velocity is set to $u_x = u_y = u_z = 0$ over the floor of the Stokes channel, oil pocket included. Symmetry along the two cuts $y = 0$ and $y = 0.6$ is accomplished via $u_y = 0$ for the Stokes part and $q = 0$ for the Reynolds parts. Finally is the flow driven by $u_x = 1, u_y = u_z = 0$ at the ceiling of the Stokes model and over the Reynolds parts. The lubricant viscosity $\mu = 1$.

For visualization purposes we apply a L_2 -projection to the Reynolds constant element pressure field forming a continuous one. In Figure 6 we present pressure contour lines on the model surface, and in Figures 7 and 8 contour lines for slices in two different directions. We can clearly identify by inspection the cavitation zone upstream in the pocket and a high pressure peak at downstream pocket side. The important note is of course



(a) FE-model from above.



(b) FE-model from below.

Figure 5: Finite element computational model. Outlet and inlet 2D Reynolds parts and 3D Stokes part in between.

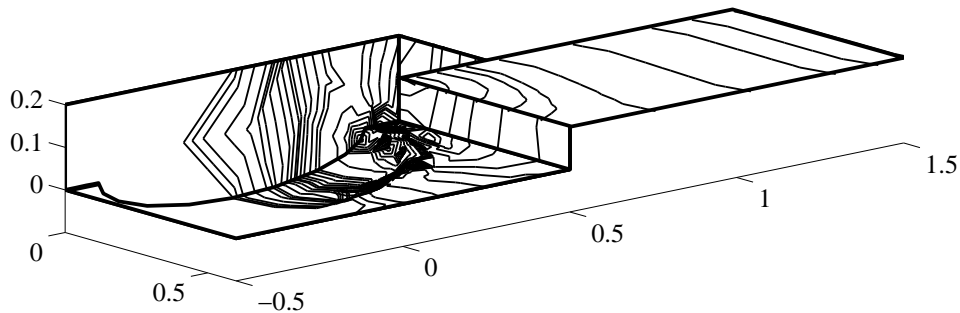


Figure 6: Pressure contour lines on the surface.

that we do not need to *a priori* define the boundary location between the fluid and cavitation phases. The classical way to approach the cavitation problem in the Reynolds community via continuity boundary conditions or first computing p_R from a pure Reynolds solution, followed by approximating $p \approx \max(0, p_R)$ (known as the half-Sommerfeld condition), is not very accurate at all compared to the cavitation model presented here.

From Figure 9 it is obvious that the weak coupling of velocity field between the models produce a Couette flow profile as expected.

If we define pocket impact to be the ratio of maximal channel height over minimal channel height Figure 10 indicates that the model at hand is potent to indicate an oil pocket impact of ≈ 1.9 that is better than all other in order to produce best lift. This is in agreement with our earlier observation described in Hansbo and Nilsson [4], and [5]. indicating depth when recirculation is induced. These two models are included in the figure purely for qualitative comparison.

As the oil pocket depth increases the Reynolds model breaks down. This is of course due to severe recirculation in the pocket, which interferes badly with one of the basic assumptions for the flow to be laminar in Reynolds model. However the Stokes model remains calm.

References

- [1] Alonso, A., Dello Russo, A., Padra, C., Rodríguez, R. (2001) An adaptive finite element scheme to solve fluid–structure vibration problems on non-matching grids, *Comput. Visual. Sci.* **4**, 67–78
- [2] Bayada, G., Chambat, M. (1986) The transition between the Stokes equation and the Reynolds equation: a mathematical proof, *Appl. Math. Optim.* **14**, 73–93.

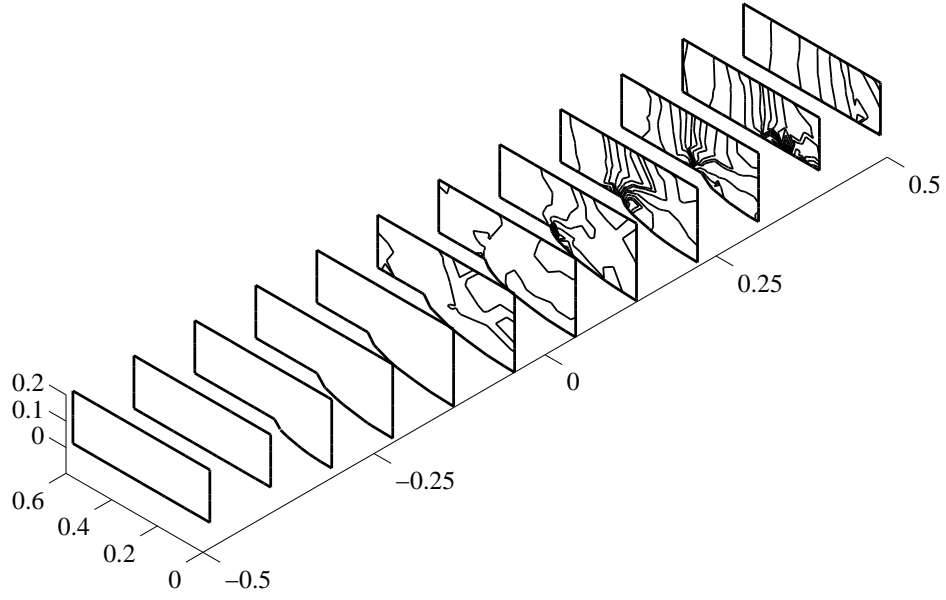


Figure 7: Pressure contour lines on x -slices.

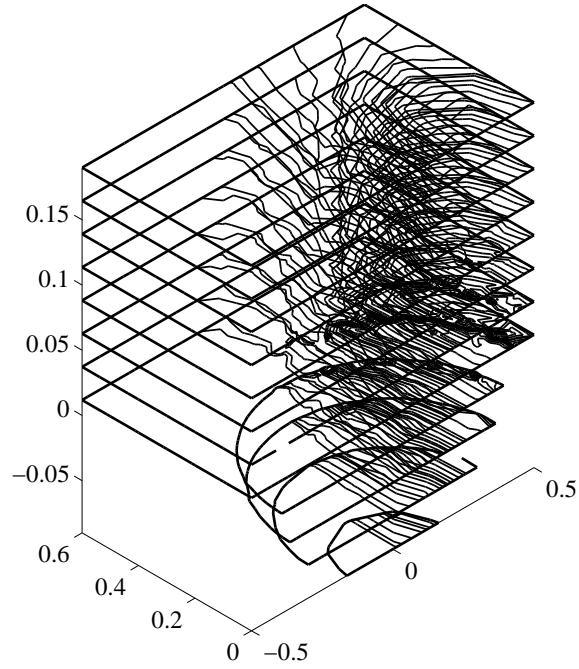


Figure 8: Pressure contour lines on z -slices.

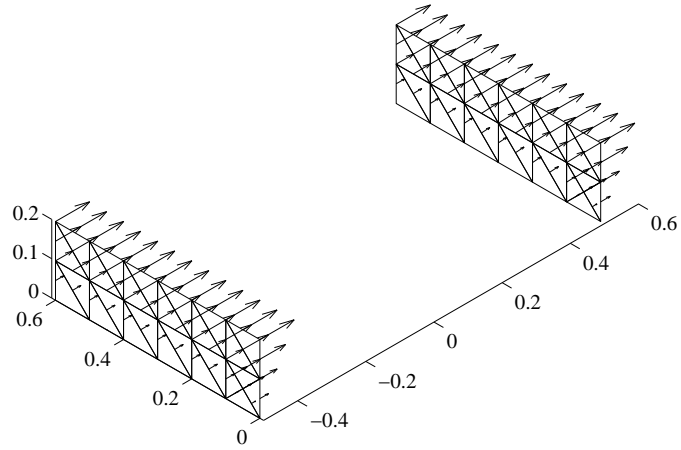


Figure 9: Couette flow profile at coupling zones.

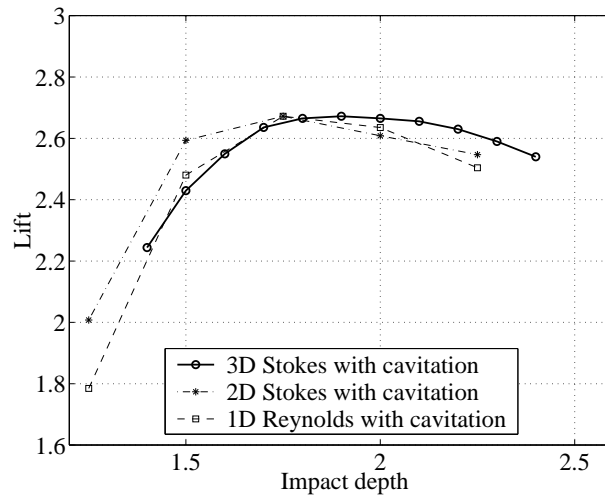


Figure 10: Lift for present coupling model. Normalized lift is included for the 2D Stokes and 1D Reynolds models just for qualitative comparison.

- [3] Brezzi, F., Hager, W.W., Raviart, P.A. (1978) Error estimates for the finite element solution of variational inequalities. Part II. Mixed methods, *Numer. Math.* **31**, 1–16.
- [4] Nilsson B., Hansbo P. Adaptive finite element methods for hydrodynamic lubrication with cavitation, *Int. J. Numer. Methods Engrg.* 72 (2007) 1584–1604.
- [5] Nilsson B., Hansbo P. A Stokes model with cavitation for the numerical simulation of hydrodynamic lubrication, Preprint, Department of Mathematical Sciences, Chalmers University of Technology, 2008.
- [6] Nilsson B. A mixed finite element formulation of Reynolds equations with cavitation, Preprint, Department of Mathematical Sciences, Chalmers University of Technology, 2009.
- [7] Reynolds, O. (1886) On the theory of lubrication and its application to Beauchamp Tower’s experiments, including an experimental determination of the viscosity of olive oil. *Philos. Trans. R. Soc. London Ser. A* 177: 157-233.
- [8] Stay, M.S., Barocas, V.H. (2003) Coupled lubrication and Stokes flow finite elements, *Int. J. Numer. Methods Fluids* **43**, 129–146.
- [9] Suttmeier, F.T. (2005) On computational methods for variational inequalities, *Comput. Mech* **35**, 401–408.